Cell

Innate immune memory after brain injury drives inflammatory cardiac dysfunction

Graphical abstract

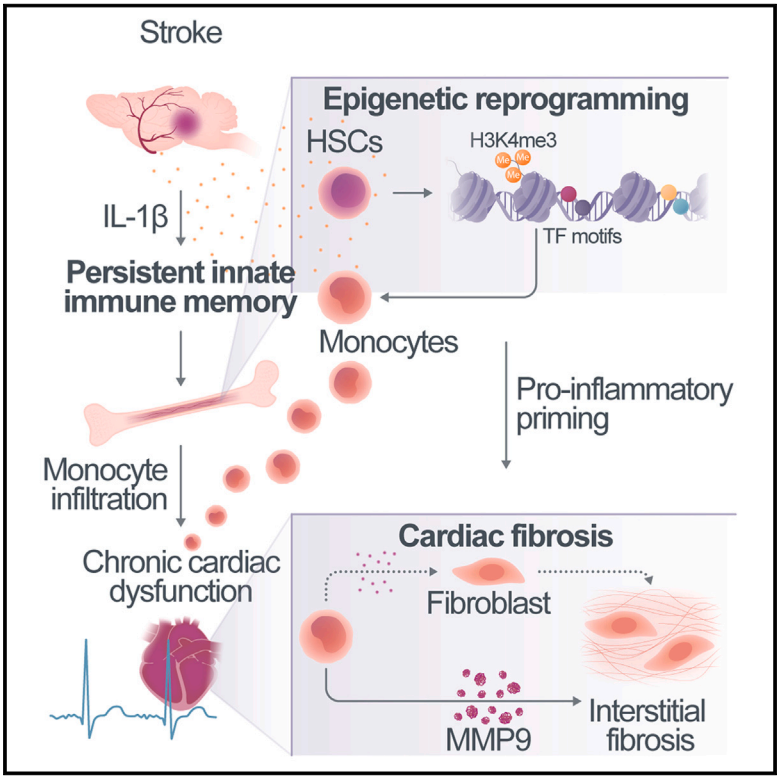

Highlights

- Acute brain ischemia leads to persistent innate immune memory
- Innate immune memory causes chronic post-stroke cardiac dysfunction
- IL-1β induces post-stroke-trained immunity through epigenetic modifications
- Blocking IL-1β or monocyte recruitment prevents cardiac dysfunction

Authors

Alba Simats, Sijia Zhang, Denise Messerer, ..., Boyan Bonev, Christian Schulz, Arthur Liesz

Correspondence

arthur.liesz@med.uni-muenchen.de

In brief

Targeting IL-1β and monocyte trafficking after ischemic stroke in the brain limits subsequent cardiac pathology, suggesting a way to prevent comorbidities due to secondary organ damage.

Simats et al., 2024, Cell *187*, 4637–4655
August 22, 2024
https://doi.org/10.1016/j.cell.2024.06.028

CellPress

Cell

CellPress
OPEN ACCESS

Article

Innate immune memory after brain injury drives inflammatory cardiac dysfunction

Alba Simats,[1,2,22] Sijia Zhang,[1,22] Denise Messerer,[3] Faye Chong,[4] Sude Beşkardeş,[4] Aparna Sharma Chivukula,[3] Jiayu Cao,[1] Simon Besson-Girard,[1] Felipe A. Montellano,[7,13] Caroline Morbach,[8] Olga Carofiglio,[1] Alessio Ricci,[1] Stefan Roth,[1] Gemma Llovera,[1] Rashween Singh,[1] Yiming Chen,[1] Severin Filser,[1] Nikolaus Plesnila,[1,9] Christian Braun,[10] Hannah Spitzer,[1] Ozgun Gokce,[1,11,12] Martin Dichgans,[1,9,11] Peter U. Heuschmann,[13,14,15] Kinta Hatakeyama,[16] Eduardo Beltrán,[9,17,18] Sebastian Clauss,[3,5,6,19] Boyan Bonev,[4,20] Christian Schulz,[3,5,6,21] and Arthur Liesz[1,9,23,*]

[1]Institute for Stroke and Dementia Research (ISD), University Hospital, LMU Munich, Munich, Germany
[2]Cerebrovascular Research Laboratory, Institute of Biomedical Research of Barcelona (IIBB), Spanish National Research Council (CSIC), Barcelona, Spain
[3]Medizinische Klinik und Poliklinik I, University Hospital, LMU Munich, Munich, Germany
[4]Helmholtz Pioneer Campus, Helmholtz Zentrum München, Neuherberg, Germany
[5]Institute of Surgical Research at the Walter-Brendel-Centre of Experimental Medicine, University Hospital, LMU Munich, Munich, Germany
[6]German Center for Cardiovascular Research (DZHK), Partner Site Munich Heart Alliance, Munich, Germany
[7]Department of Neurology, University Hospital Würzburg, Würzburg, Germany
[8]Department Clinical Research & Epidemiology, Comprehensive Heart Failure Center, and Department Medicine I, University Hospital Würzburg, Würzburg, Germany
[9]Munich Cluster for Systems Neurology (SyNergy), Munich, Germany
[10]Institute of Legal Medicine, Faculty of Medicine, LMU Munich, Munich, Germany
[11]German Center for Neurodegenerative Diseases (DZNE), Partner Sites Munich and Bonn, Germany
[12]Department of Old Age Psychiatry and cognitive Disorders, University Hospital Bonn, University of Bonn, Bonn, Germany
[13]Institute of Clinical Epidemiology and Biometry, Julius-Maximilian-University Würzburg, Würzburg, Germany
[14]Institute for Medical Data Sciences, University Hospital Würzburg, Würzburg, Germany
[15]Clinical Trial Centre Würzburg, University Hospital Würzburg, Würzburg, Germany
[16]Department of Pathology, National Cerebral and Cardiovascular Center, Suita, Japan
[17]Institute of Clinical Neuroimmunology, University Hospital, LMU Munich, Munich, Germany
[18]Biomedical Center (BMC), Faculty of Medicine, LMU Munich, Martinsried, Germany
[19]Interfaculty Center for Endocrine and Cardiovascular Disease Network Modelling and Clinical Transfer (ICONLMU), LMU Munich, Munich, Germany
[20]Physiological Genomics, Biomedical Center, Ludwig-Maximilians-Universität München, Munich, Germany
[21]Department of Immunopharmacology, Mannheim Institute for Innate Immunoscience (MI3), Medical Faculty Mannheim, Heidelberg University, Mannheim, Germany
[22]These authors contributed equally
[23]Lead contact
*Correspondence: arthur.liesz@med.uni-muenchen.de
https://doi.org/10.1016/j.cell.2024.06.028

SUMMARY

The medical burden of stroke extends beyond the brain injury itself and is largely determined by chronic comorbidities that develop secondarily. We hypothesized that these comorbidities might share a common immunological cause, yet chronic effects post-stroke on systemic immunity are underexplored. Here, we identify myeloid innate immune memory as a cause of remote organ dysfunction after stroke. Single-cell sequencing revealed persistent pro-inflammatory changes in monocytes/macrophages in multiple organs up to 3 months after brain injury, notably in the heart, leading to cardiac fibrosis and dysfunction in both mice and stroke patients. IL-1β was identified as a key driver of epigenetic changes in innate immune memory. These changes could be transplanted to naive mice, inducing cardiac dysfunction. By neutralizing post-stroke IL-1β or blocking pro-inflammatory monocyte trafficking with a CCR2/5 inhibitor, we prevented post-stroke cardiac dysfunction. Such immune-targeted therapies could potentially prevent various IL-1β-mediated comorbidities, offering a framework for secondary prevention immunotherapy.

INTRODUCTION

We and others have previously shown that acute brain injuries induce a sterile, systemic inflammatory response.[1] The inflammatory response to sterile injury is rapidly initiated by the release of immunogenic alarmins, such as nuclear proteins or DNA from necrotic cells to the blood circulation.[2] It is further characterized by an increase in blood cytokine levels, the mobilization of immune cells, and profound changes in immune cell composition and function.[3] In contrast to the acute inflammatory response within hours to few days, the chronic effects of brain injury on systemic immunity are largely unknown. Few studies mainly investigating blood biomarkers have suggested chronic changes in the concentrations of circulating cytokines and other inflammatory markers, such as interleukin (IL)-6, IL-1, C-reactive protein (CRP), interferon (IFN)-γ, and high-mobility group box 1 (HMGB1).[4–7] However, a detailed analysis of the chronically compromised systemic immune compartment after brain injury is still missing, and the underlying mechanisms are largely unknown.

Acute brain injuries due to ischemic stroke are a leading cause of mortality and long-term disabilities in adults. Besides the early mortality and morbidity due to the ischemic brain injury itself, long-term morbidity after stroke is also due to the high prevalence of secondary comorbidities and complications, such as cognitive impairment and dementia, post-stroke depression, cardiac events, persistent vascular inflammation, and stroke-induced metabolic disturbances.[8–12] Yet, the exact cause of this increased risk of long-term secondary comorbidities after stroke remains elusive.

Recent studies have demonstrated long-term changes in the function of innate immune cells after bacterial infections or vaccination. This phenomenon has been termed innate immune memory or "trained immunity" in contrast to antigen-specific adaptions in long-lived lymphocytes (T and B cells).[13] Innate immune memory has been demonstrated in proof-of-concept infection studies to alter the responsiveness to pathogens after re-infection. This represents a beneficial evolutionary mechanism for the clearance of infectious pathogens, but can also result in potentially pathological functions during aging and autoimmunity due to aberrant inflammation.[14] Yet, barely any information is available on mechanisms and consequences of trained immunity after sterile tissue injuries. Epigenetic changes in myeloid cells have been reported in models of organ transplantation,[15] experimental arthritis, and in patients with systemic lupus erythematosus.[16,17] Similarly, alterations in hematopoiesis and pro-inflammatory monocyte priming have been associated with cardiovascular disease, particularly atherosclerosis and associated comorbidities.[18] We hypothesized that sterile tissue injuries such as stroke might result in similar long-term innate immune memory and that these long-term immunological consequences after stroke might drive secondary comorbidities.

RESULTS

Stroke induces long-term inflammatory changes in systemic monocytes/macrophages

To test a potential effect of stroke on long-term systemic inflammation, we performed a comprehensive single-cell mRNA sequencing analysis of CD45+CD11b+ myeloid cells from blood and multiple peripheral organs 1 month after experimental ischemic stroke, which have previously been associated with inflammatory consequences of brain injury in the acute phase (Figure 1A).[2,19–21] For this, we used a well-established experimental stroke model of transient occlusion of the middle cerebral artery,[22] which results in relatively large lesion volumes, but mice largely recover from the neurological symptoms already within 1–2 weeks (Figure S1A). After performing unsupervised clustering, we projected a total of 29,124 myeloid cells and identified 20 independent clusters based on the most variable genes (Figures 1B and S1B). We found a large number of genes to still be differentially regulated at this late chronic time point after stroke, particularly within the population of monocytes/macrophages, while other cell populations, including neutrophils or dendritic cells, were less affected (Figure 1C). Also, transcriptomic changes in monocytes/macrophages were not associated with changes in the frequencies of any subcluster (Figures S1C and S1D) that would explain the difference. The post-stroke monocytic transcriptomic signature was associated with a pro-inflammatory phenotype, characterized by significant upregulation of various biologically relevant inflammatory signaling pathways of circulating monocytes and tissue macrophages, including increased expression of genes involved in chemotaxis and cell adhesion (e.g., Cx3cr1, Lyz2, Icam1, and Itga4), cytokine- and IFN-mediated signaling pathways (e.g., Csf1r, Cebpa, Itgb2, Il10ra, Aim2, Irf8, and Irf5), and pattern recognition receptors (PRRs) (e.g., Irak2 and Tab2) (Figures 1D, S1E, and S1F).[23,24] Furthermore, through a biological network analysis, we confirmed the involvement of other pro-inflammatory mediators, such as IL-12, IL-1, and IFN-α and IFN-β, and the downstream NF-κb and Akt signaling pathways in the activated phenotype of resident monocytes/macrophages in peripheral organs 1 month after stroke (Figure S1G).

Across organs, changes in the monocyte/macrophage population were particularly pronounced in the heart and liver. Principal-component analysis (PCA) based on a total of 18,835 genes showed that changes in blood, spleen, and lung were more subtle (Figures 1E and S1H). Specifically, we detected the selective expansion of a Ly6C^{high}-expressing monocyte population in hearts 1 month after stroke (Figures 1F, 1G, and S1I), which changed the differentiation trajectories of monocytes to cardiac macrophages. Correspondingly, we term this population "post-stroke monocytes/macrophages" (Figures 1H, S1K, and S1L). In addition, cardiac Ly6C^{high} monocytes after stroke showed increased expression of genes related to tissue residency when compared with circulating monocytes (Figure S1J). Moreover, we found that the genes driving the post-stroke differentiation of monocytes into cardiac macrophages positively correlate with immune response and leukocyte activation pathways (Figures S1M and S1N). Taken together, these results suggest that stroke chronically promotes the recruitment of circulating Ly6C^{high} monocytes to the heart, which might further differentiate into tissue-resident macrophages.

Stroke results in chronic cardiac diastolic dysfunction

To assess the functional consequences of changes in the cardiac monocyte/macrophage population during the chronic

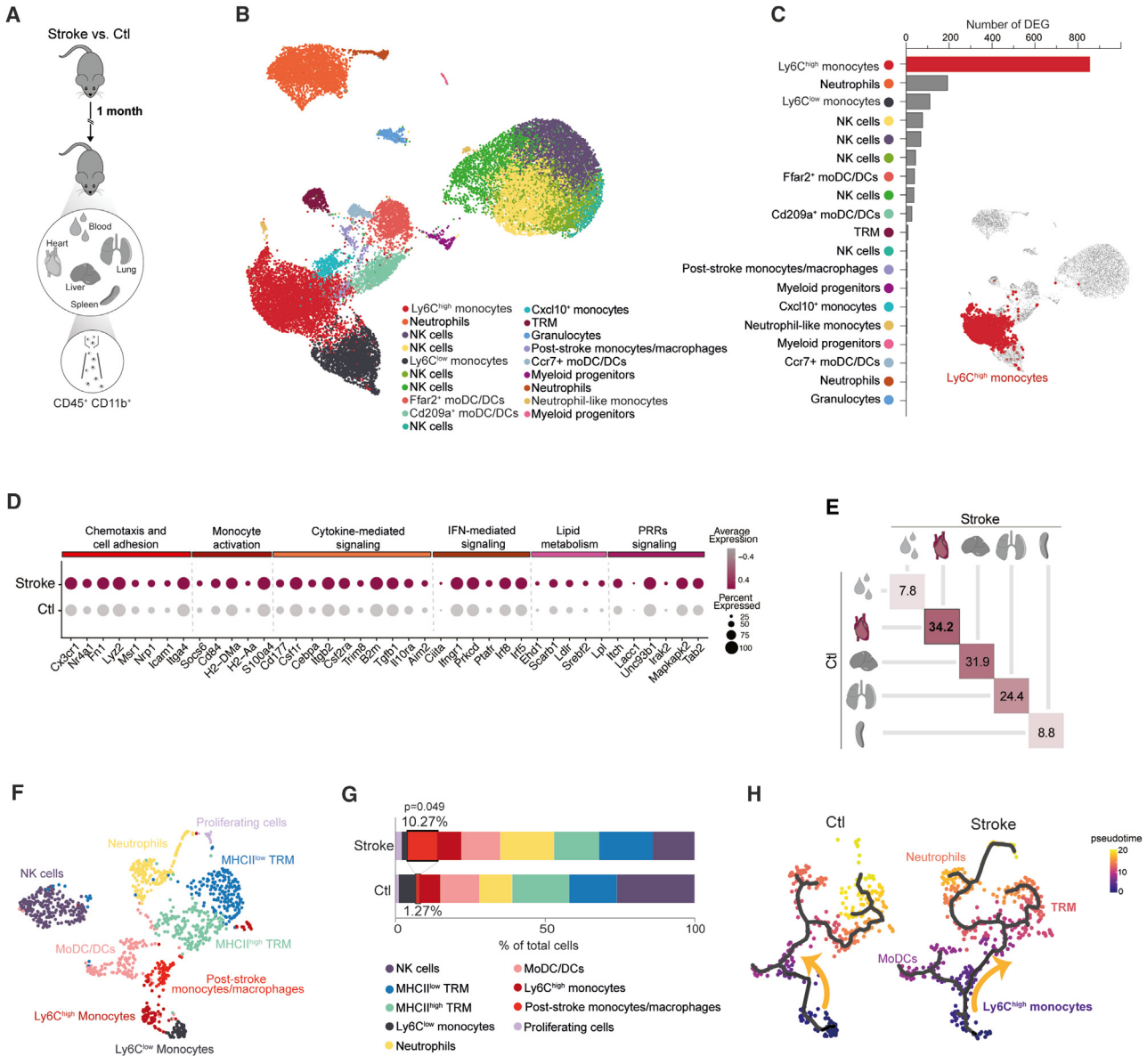

Figure 1. Stroke induces long-term inflammatory changes in systemic monocytes/macrophages

(A) Myeloid cells were sorted from blood and peripheral organs 1 month after experimental ischemic stroke (n = 4/group) for single-cell mRNA sequencing.

(B) UMAP plot of 29,124 CD45$^+$ CD11b$^+$ cells, colored by identified clusters.

(C) Number of differentially expressed genes (DEGs) between conditions per identified population (adj. $p < 0.05$). Ly6C^{high} monocytes show the highest number of DEGs (857 genes).

(D) Expression levels of selected genes in the Ly6C^{high} monocytes highlighted in (C) and selected from the enriched Gene Ontology (GO) terms in the set of DEGs between conditions (adj. $p < 0.1$). The dot size corresponds to the fraction of cells within each condition, and the color indicates average expression.

(E) Euclidian distances in the PCA space between the stroke and control per organ. The PCA was calculated from a total of 18,834 genes identified in all CD45$^+$CD11b$^+$ cells.

(F and G) (F) UMAP plot of 1,117 CD45$^+$ CD11b$^+$ cells from the heart, colored by identified populations, and (G) stacked bar graph for percentage of identified population per condition (chi-square test).

(H) Monocle3 pseudo-temporal ordering of CD45$^+$ CD11b$^+$ cells from the heart superimposed on the UMAP plot and split by condition. Cells are colored based on their progression along pseudo-temporal space.

See also Figure S1.

phase following stroke, we investigated cardiac function using Doppler echocardiography. We observed a persistent reduction in end-diastolic left ventricle (LV) volume, while the systolic function, measured by the ejection fraction and fractional shortening, was only transiently affected by stroke in the acute phase (Figures 2A and S2A; Table S1). These findings suggest the

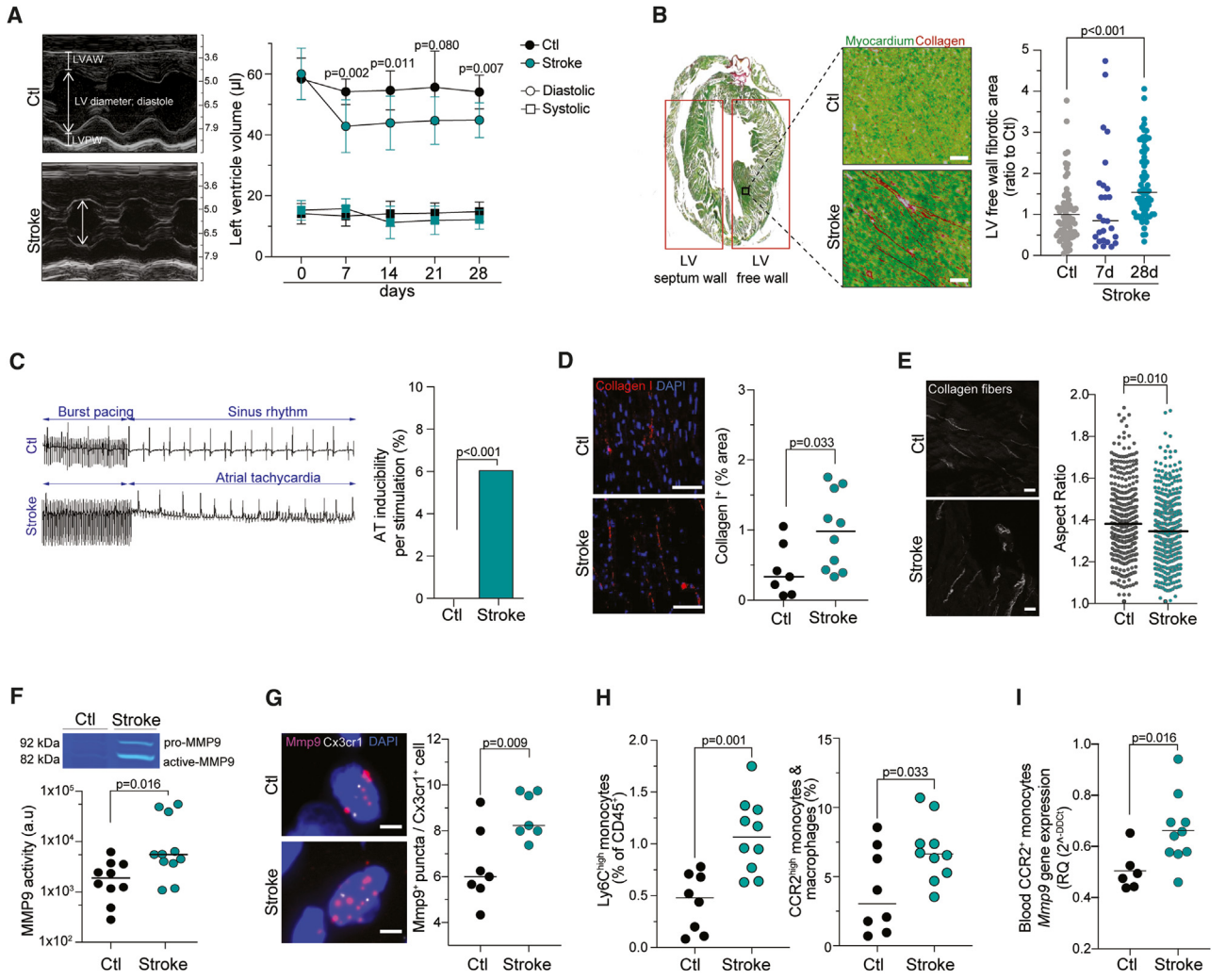

Figure 2. Stroke results in chronic cardiac diastolic dysfunction and inflammatory cardiac remodeling

(A) Representative ultrasound images (M-mode) performed at indicated time points (n = 12[stroke]/6[control]) and quantification of the left ventricle (LV) volume in systole (squares) and diastole (circles). LVAW, left ventricle anterior wall; LVPW, left ventricle posterior wall.

(B) Representative images (Sirius red/fast green staining) and quantification of cardiac fibrosis in the LV free wall (t test, n = 7/10 per group, 4 independent sections per mouse).

(C) Representative image of cardiac electrophysiology at 1 month after stroke or control (n = 7/group) and quantification of inducibility of atrial tachycardia (AT).

(D) Representative image and quantification of collagen I content, expressed in percentage of total area of the LV free wall (scale bars, 50 µm; t test, n = 8/10 per group).

(E) Representative second harmonic generation (SHG) images for the detection of the organization of fibrillar collagen and quantification of the aspect ratio (scale bars, 20 µm; nested t test, n = 9/10 mice per group, 35–50 images per mouse heart).

(F) Enzymatic MMP9 activity using *gel* zymography of heart samples 1 month after stroke or control (U test, n = 10/11 per group).

(G) Representative images of single-molecule fluorescence *in situ* hybridization (smFISH) and quantification of the number of *Mmp9* mRNA puncta per *Cx3cr1*$^+$ cell (scale bars, 5 µm; t test, n = 7 per group).

(H) Quantification of flow cytometry for Ly6C^{high} monocytes (CD45$^+$ Ly6G$^-$ CD11b$^+$ F4/80$^-$ Ly6C^{high}) and CCR2^{high} monocytes/macrophages (CD45$^+$ Ly6G$^-$ CD11b$^+$ F4/80$^+$ CCR2^{high}) in the heart 1 month after stroke or control (t test; n = 8/10 per group).

(I) *Mmp9* mRNA expression (RT-qPCR) in sorted blood CCR2$^+$ monocytes relative to *Ppia* expression and normalized to control (U test, n = 6/10 per group).

See also Figure S2.

selective development of chronic diastolic dysfunction, which was further confirmed using pulse wave Doppler of the apical four-chamber-window demonstrating compromised left ventricular compliance by decreased mitral valve E wave deceleration time (Figure S2B). Heart failure in patients with preserved ejection fraction but diastolic dysfunction is commonly associated with cardiac fibrosis, which impairs the rapid LV filling due to increased myocardial stiffness.[25,26] Hence, we evaluated the amount of fibrosis in hearts after stroke or in control mice and observed significantly increased LV fibrosis 1 month after stroke,

which remained increased still at 3 months post-stroke (Figures 2B, S2C, and S2D). Importantly, this observed post-stroke cardiac fibrosis was not associated with renal dysfunction, gross anatomical cardiac alterations, or persistent perturbations in autonomous cardiac innervation beyond the acute post-stroke phase (Figures S2E–S2J). To test the potential impact of post-stroke cardiac fibrosis, we next conducted an invasive electrophysiological (EP) study 1 month after stroke. In line with a previous study identifying the role of cardiac inflammation as a risk factor for atrial fibrillation,[27] we observed a higher inducibility of atrial arrhythmias following burst stimulation in stroke mice, which was absent for control mice (Figure 2C; Table S2).

We further characterized the composition of the extracellular matrix (ECM) in hearts after stroke and observed that increased cardiac fibrosis was mainly due to increased deposition of type I collagen (Figures 2D and S2K). Further analysis of collagen orientation in the LV myocardium by second harmonic generation microscopy revealed increased fiber disorganization after stroke, suggesting ECM remodeling in addition to increased deposition (Figure 2E). Therefore, we analyzed cardiac matrix metalloproteinase (MMP) activity—key effector enzymes in ECM remodeling—and observed significantly increased MMP9 activity by gel zymography (Figure 2F) as well as total pro-MMP9 protein content after stroke (Figure S2L). More specifically, we detected by single-molecule fluorescence *in situ* hybridization (smFISH) significantly increased *Mmp9* transcripts in cardiac macrophages, as the most likely source of increased cardiac MMP9 expression, which was confirmed by RT-qPCR of sorted cardiac monocytes/macrophages (Figures 2G and S2M). Corresponding to results of the single-cell sequencing analysis (see Figures 1F and 1G), we also observed by flow cytometry an increased number of Ly6C^{high} monocytes and CCR2^{+} cardiac monocytes/macrophages in post-stroke hearts (Figures 2H and S2N). These results suggest a higher infiltration of circulating monocytes and an enhanced monocyte-to-macrophage differentiation chronically after stroke.[28,29] In addition, we observed that circulating monocytes after stroke also have a significantly increased expression of *Mmp9* (Figure 2I).

We next aimed to validate the translational relevance of these observations. First, we were able to confirm the development of post-stroke chronic cardiac dysfunction in three representative stroke patients recruited by the Stroke-Induced Cardiac Failure (SICFAIL) study consortium that have been followed up by cardiac echocardiography at 3 and 6 months after the incident stroke event (Figure 3A). In addition, we obtained myocardial autopsy samples from patients that had died 1–3 months after stroke or from age-matched control subjects that had died without cardiac or brain disorder (confirmed by autopsy, Figure 3B; Table S3). We observed significantly increased ECM deposition in the left ventricular wall of stroke patients (Figures 3C and 3D). We also detected a significant increase in CCR2^{+} monocyte counts in post-stroke hearts, which correlated with cardiac collagen content, while total monocyte and macrophage counts did not differ between groups (Figures 3E–3G). Consistent with our experimental results, human cardiac macrophages also expressed significantly more *MMP9* transcripts after stroke (Figure 3H). Finally, we performed bulk mRNA sequencing on adjacent tissue sections used for the histological analyses above and found significant transcriptional differences between control subjects and after stroke (Figures 3I and 3J). Interestingly, several of the upregulated genes in stroke patients were associated with ECM remodeling, including paraoxonase 1 (*PON1*) and keratinocyte-associated protein 2 (*KRTCAP2*). Taken together, we observed marked cardiac fibrosis and ECM remodeling in both experimental mice and stroke patients, which was further associated with diastolic dysfunction after experimental stroke. A hallmark of this secondary cardiac pathology after stroke is the increased recruitment and pro-inflammatory profile of cardiac monocytes/macrophages.

Stroke promotes chronic monocyte recruitment into the heart

Using an inducible myeloid progenitor reporter mouse strain (Ms4a3^{creERT2}xAi14; Figures S3A–S3C), we observed that cellular recruitment of cardiac monocytes/macrophages occurs not only as an acute response to stroke but persists over time as a chronic, long-term consequence (Figure 4A). In addition, based on *in* vivo 5-ethynyl-2'-deoxyuridine (EdU)-labeling experiments, we observed that more than 95% of cardiac myeloid cells will have been replaced within 1 month after stroke (Figure 4B), underscoring the significance of infiltrated monocytes in influencing post-stroke cardiac function. Therefore, we further studied the contribution of peripheral monocytes to heart fibrosis using an inducible reporter mouse strain under control of the *Ccr2* promoter to label infiltrating monocytes (Ccr2^{creERT2}xAi14, Figure 4C). Cardiac interstitial cells from mice 1 month after stroke and control mice were analyzed by single-cell sequencing, excluding intravascular cells by intravenous (i.v.) antibody labeling. We identified 20 cell clusters corresponding to the heterogeneous cell populations of cardiac cell subsets (Figure S3D). A more detailed analysis identified 7 distinct populations of cardiac monocytes and macrophages (Figures 4D and S3E). Ccr2-tdTomato (tdT) expression was specifically enriched in 4 of the monocyte/macrophage subsets (Figures 4E and 4F). Unsupervised trajectory analysis further confirmed our finding that circulating Ly6C^{high} monocytes infiltrate the heart and acquire a tissue-resident monocyte/macrophage phenotype (Figures 4G and 4H). In addition, we observed that invading tdT^{+} cells after stroke are characterized by an upregulation of various biologically relevant signaling pathways (Figure 4I). Furthermore, we performed cell-cell interaction analysis using CellChat between the tdT^{+} cell subsets as source and cardiac fibroblasts as target cells, revealing a large number of upregulated interactions (while none were downregulated) associated with processes involved in tissue fibrosis and inflammation (Figure 4J). Using *in situ* smFISH for collagen I mRNA in conjunction with vimentin staining, we detected a significant increase in vimentin-positive fibroblasts as well as higher expression of *Collagen I* transcripts in fibroblasts chronically after stroke (Figure 4K).

BM cellularity and function are chronically altered after stroke

To explore the potential mechanisms of post-stroke immune-mediated cardiac dysfunction, we performed an in-depth analysis of the bone marrow (BM) myeloid compartment in the

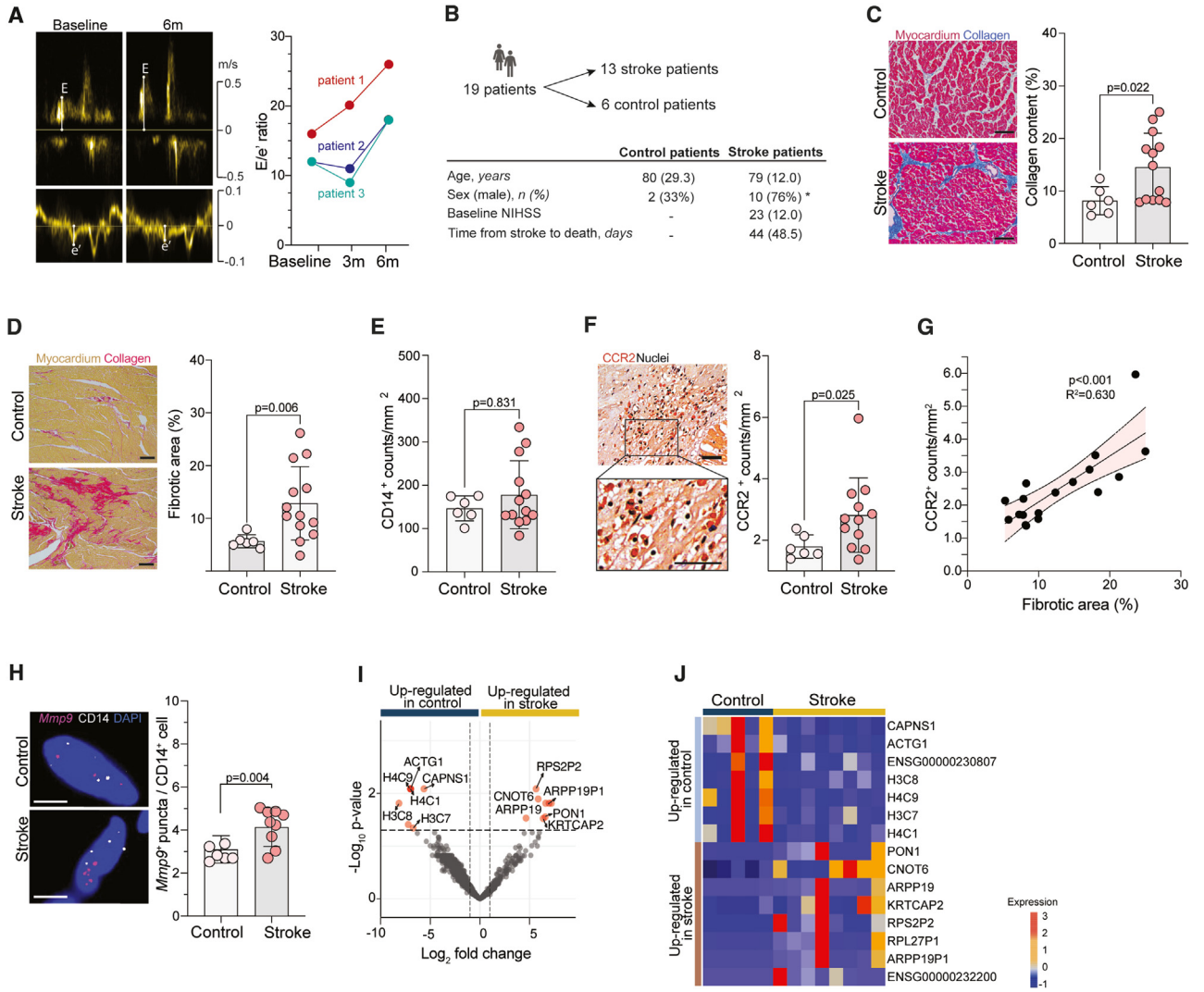

Figure 3. Stroke increases cardiac fibrosis and monocyte accumulation in patients

(A) Representative images of the patient with chronic diastolic dysfunction recruited by the Stroke-Induced Cardiac Failure (SICFAIL) study consortium. Corresponding quantification of the E/e′ of 3 patients identified with chronic diastolic dysfunction.

(B) Myocardial autopsy samples were collected from a total of 19 patients: 12 ischemic stroke (IS) patients and 7 controls, who died without cardiac or brain disorder (confirmed by autopsy). Basic demographical and clinical characteristics are depicted. Data are expressed as median (interquartile range [IQR]), unless stated otherwise. *$p < 0.05$ (chi-square test).

(C) Representative images (Masson trichrome staining, scale bars, 0.1 mm) and quantification of collagen content (t test).

(D) Representative images (Sirius red/fast green staining, scale bars, 0.2 mm) and quantification of the collagen content expressed as percentage of total cardiac area (t test).

(E) Quantification of $CD14^+$ cells (t test).

(F) Representative image (scale bars, 0.05 mm) and quantification (t test) of $CCR2^+$ cells.

(G) Correlation of $CCR2^+$ cell counts with cardiac fibrosis (Masson trichrome staining, Pearson correlation test).

(H) Representative images and quantification of single-molecule fluorescence *in situ* hybridization (smFISH) for the detection of *Mmp9* mRNA puncta expression in $CD14^+$ cardiac cells from stroke and control patients (scale bars, 5 μm; t test, $n = 7/9$ per group).

(I) Volcano plot showing regulated genes in the myocardium between IS and control patients. Colored genes are $p < 0.05$.

(J) Heatmap showing the top differentially expressed genes in the heart between IS and control patients.

chronic phase after stroke. We analyzed long-term effects of stroke on the BM by single-cell sequencing. We identified 21 cell clusters and the respective differentiation trajectories from hematopoietic stem and progenitor cells (HSPCs) to all other mature myeloid populations (Figures 5A, 5B, and S4A) and uncovered a distinct transcriptomic signature in $Ly6C^{high}$ monocytes chronically after stroke (Figure 5C). Additionally, we observed a substantial number of differentially expressed genes (DEGs) in HSPCs, suggesting that also progenitor populations exhibited persistent transcriptional alterations during the chronic

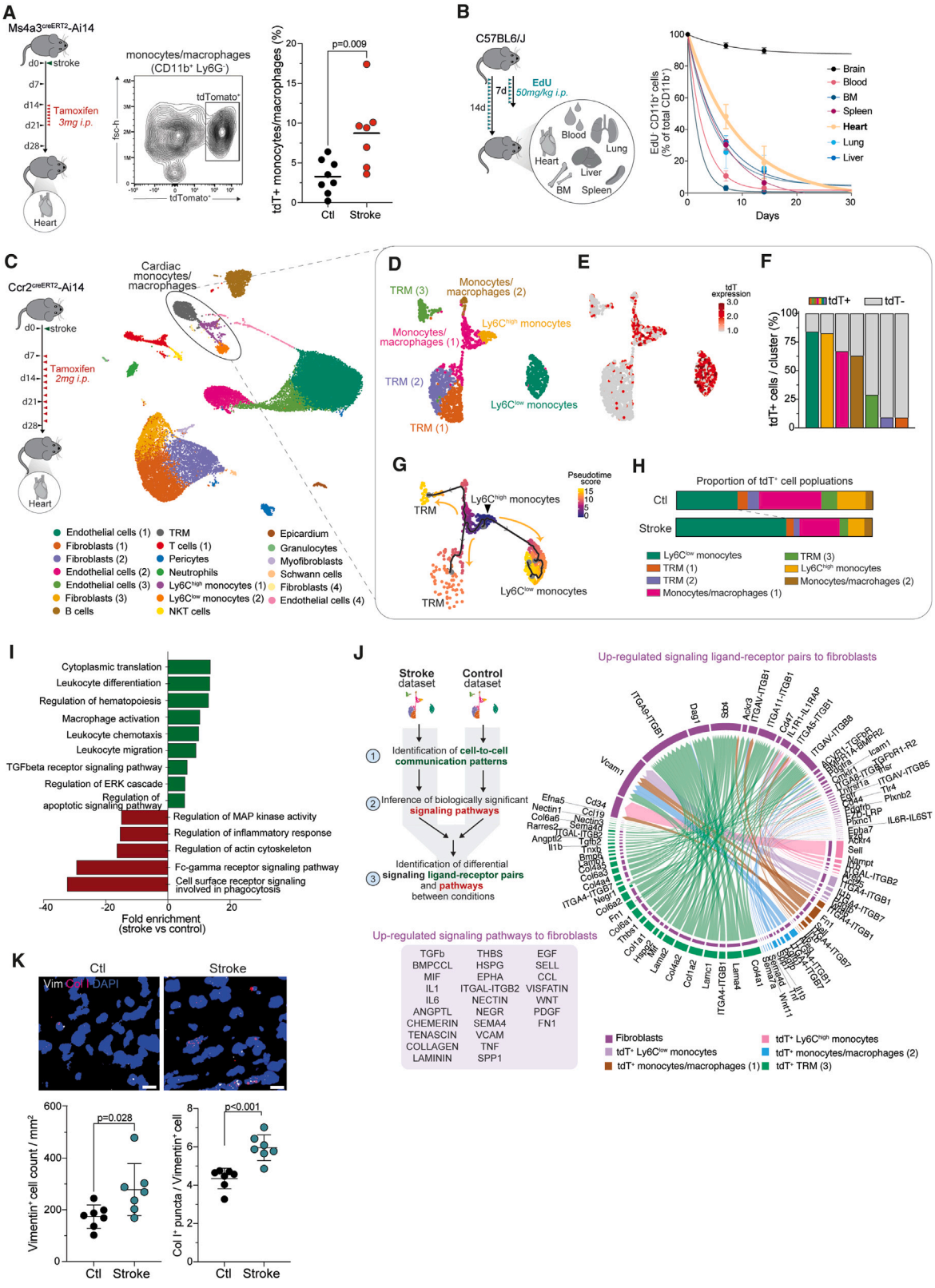

(legend on next page)

stage after stroke, which were associated with inflammatory pathways (Figures S4B and S4C). Moreover, the post-stroke transcriptomic signature in mature monocytes from the BM was also highly conserved in circulating monocytes and differentiated monocytes recruited to peripheral organs (Figure S4D). Apolipoprotein E (ApoE) and lipoprotein lipase (Lpl) were consistently transcriptionally upregulated after stroke, which was additionally confirmed on protein level (Figure S4E). Stroke-induced transcriptional changes in HSPCs and mature monocytes persisted up to 3 months after stroke, suggesting a sustained and potentially progressive effect of stroke on the BM transcriptomic landscape (Figure S4F).

To validate these findings, flow cytometry analyses were conducted, confirming altered BM cellularity (Figures 4D, 4E, S4G, and S4H). Labeling of proliferating cells with a single intraperitoneal EdU injection 1 month after stroke indicated significantly increased proliferation rates of myeloid progenitor cell populations (Figure S4I). Of note, the increased myelopoiesis after stroke was dependent on the lesion severity, since no effect on BM cellularity was observed after a transient ischemic attack or minor stroke (Figure S4J).

Stroke induces persistent innate immune memory

To test the persistence and potentially causal role of the observed myeloid changes chronically after stroke, we transplanted GFP-positive, enriched HSPCs from BM 1 month after stroke or control surgery into naive recipients, using a genetic BM depletion model (poly(I:C) administration to $Mx1^{Cre}$:c-$myb^{fl/fl}$ mice) in order to avoid confounding effects by irradiation or chemotherapy (Figure 5F). 1 month after transplantation, we isolated GFP^+ transplanted myeloid cells for single-cell mRNA sequencing and confirmed successful BM repopulation for all analyzed animals, without differences in the BM repopulation potential between groups (Figures 5G and S5A–S5E). Differential gene expression between stroke and control transplanted BM cells showed substantial transcriptomic differences 1 month after transplantation in the naive recipient mice (Figures S5F and S5G). Interestingly, comparing the most significantly regulated transcriptomic pathways between the transplanted mice to the original differences between animals 1 month after stroke and control surgery revealed a highly conserved phenotype in the transplanted cells after stroke (Figure 5H). Both BM cells from stroke mice and BM cells from recipient mice transplanted with stroke BM cells retained a pro-inflammatory activated phenotype. Projecting all individual samples into a PCA bidimensional space, we found that cells from mice transplanted with stroke BM showed spatial proximity to cells from stroke mice (Figures S4H and S4I), confirming that myeloid cells acquire a distinct pro-inflammatory phenotype after stroke that is transmissible by BM transplantation.

1 month after BM transplantation, we also isolated GFP^+ transplanted myeloid cells (CD45+CD11b+) from the heart and blood of recipient mice. Using unsupervised clustering, we identified distinct myeloid GFP^+ populations in both the heart and blood (Figure S5J). Using pseudotime analysis on the combined dataset from blood and heart, we observed a shift in the differentiation trajectory from blood monocytes to heart monocytes/macrophages following stroke (Figure 5I). The altered pseudotime trajectory post-stroke was driven by a differentially higher contribution of blood-derived $Ly6C^{high}$ monocytes to tissue-resident monocytes and macrophages after stroke (Figures 5I and 5J). In addition, we found that a considerable proportion of the DEGs identified in circulating monocytes also remained differentially expressed in cardiac monocyte/macrophages after stroke (Figure S5K). These common genes were found to participate in pathways related to stress response, immune cell activation, migration, and differentiation. We next analyzed the hearts of BM recipient mice for hallmarks of ECM remodeling observed after stroke. We found significantly increased *Mmp9* expression in cardiac macrophages of mice receiving BM from stroke donors and, more specifically, an increase of *Mmp9* expression particularly in transplanted GFP^+ cardiac monocytes/macrophages (Figures 5K and 5L). Moreover, we observed significantly increased cardiac fibrosis in animals receiving the stroke BM transplant in comparison to control BM recipients (Figure 5M). Together, these findings demonstrate that myeloid function is

Figure 4. Stroke promotes chronic monocyte recruitment into the heart

(A) $Ms4a3^{creERT2}$-Ai14 stroke and control mice were daily administered with tamoxifen for 7 consecutive days from day 14 after stroke. Cardiac myeloid cells were analyzed by flow cytometry 1 month after stroke or control (n = 7/8 per group). Representative gating strategy for the tdTomato (tdT^+) cardiac monocytes/macrophages ($CD45^+$ $Ly6G^-$ $CD11b^+$, middle) and quantification of tdT^+ cardiac monocytes/macrophages (right).

(B) Mice were daily administered with EdU for 7 or 14 days after stroke. Lineage-negative myeloid cells from the blood and peripheral organs were analyzed by flow cytometry for percentage of EdU^+ $CD11b^+$ cells per time point (n = 6/7 per organ).

(C) $CCR2^{creERT2}$-Ai14 reporter mice received tamoxifen every second day from day 7 after stroke or control surgery until 1 month, and cardiac interstitial cells were analyzed using single-cell mRNA sequencing (n = 2 mice/group).

(D) UMAP plot of a total of 34,927 cardiac interstitial cells, colored by identified clusters, and (D) UMAP plot of the cardiac monocytes/macrophages subsets.

(E) UMAP plot showing the expression of tdT within the cardiac monocytes/macrophages.

(F) Percentage of tdT^+ cells per cell subset.

(G) Monocle3 pseudo-temporal ordering of tdT^+ cardiac monocytes/macrophages superimposed on the UMAP plot. Cells are colored based on their progression along pseudo-temporal space.

(H) Stacked bar graph for percentage of cells per population.

(I) Pathway analysis for tDEGs between conditions in tdT^+ cardiac monocytes/macrophages. Biological processes were grouped and sorted by p value.

(J) Schematic design of cell-cell interaction analysis (left upper) and chord plot showing upregulated ligand-receptor pairs from tdT^+ cardiac monocytes/macrophages populations to fibroblasts after stroke. List of upregulated signaling pathways from tdT^+ cardiac monocytes/macrophages populations to fibroblasts after stroke.

(K) Representative images and quantification of single-molecule fluorescence *in situ* hybridization (smFISH) for the detection of the count of *Vimentin*$^+$ cardiac fibroblasts and the *Collagen I* mRNA expression in *Vimentin*$^+$ fibroblasts 1 month after stroke or control (scale bars, 5 μm; t test, n = 7/group).

See also Figure S4.

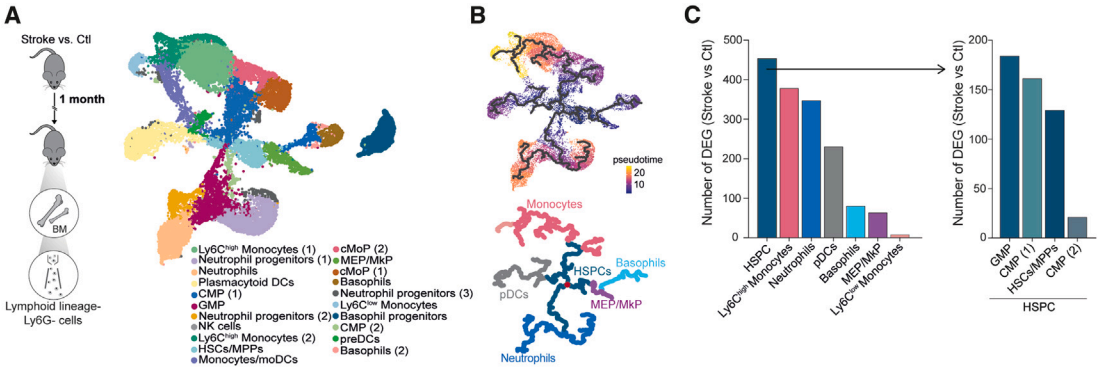

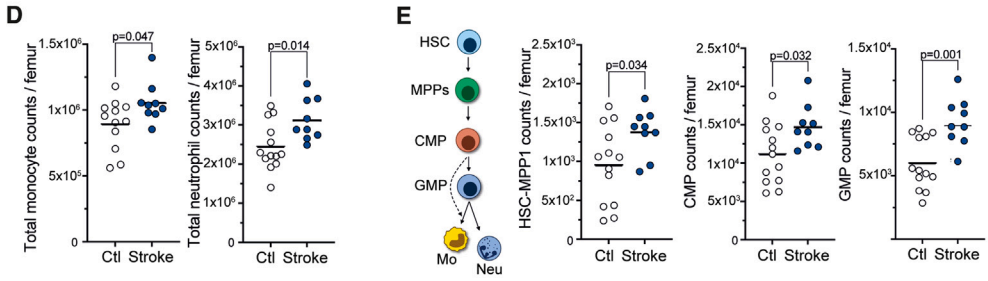

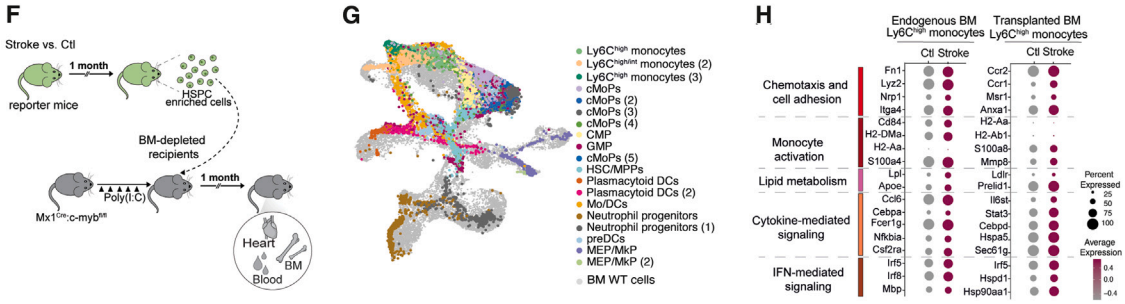

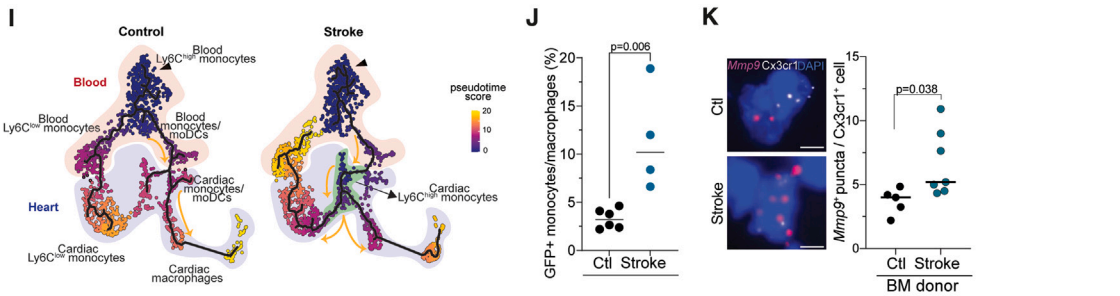

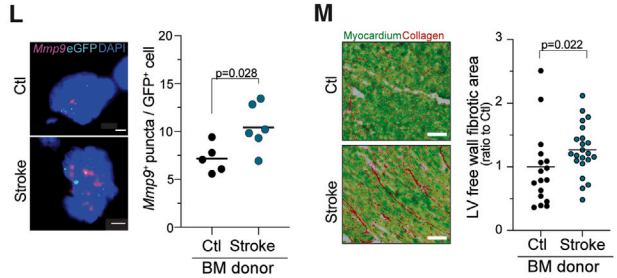

(legend on next page)

not only stably altered after stroke but that these changes in the myeloid compartment are sufficient to drive secondary cardiac fibrosis.

Innate immune memory is mediated by early post-stroke IL-1β secretion

The observed effects all indicate a phenomenon described after vaccination and in infection models as trained immunity,[14] which generally describes a heightened response of innate immune cells to subsequent stimuli. Indeed, we observed that primary monocytes as well as BM-derived macrophages isolated from stroke mice had an increased phagocytic activity compared with cells from control mice (Figure 6A). Furthermore, cells from mice with a stroke also showed an increased response to cytokine stimulation (Figure S6A), overall confirming the development of trained immunity due to stroke.

A characteristic hallmark of trained immunity is epigenetic reprogramming of myeloid cells. Therefore, we first assessed histone modifications at 1 month after stroke or in control mice for key histone marks and identified changes in both enhancer-associated marks (H3K4me1 and H3K27ac), as well as in H3K4me3, which is a histone modification associated with active promoters[14] (Figure S6B). Next, we wanted to examine if similar transcription factors (TFs) are involved in rewiring of the epigenetic landscape at promoters in HSPC and monocytes. Correspondingly, we identified differential enrichment of several TF motifs including CTCF, STAT1/2, GABPA, CEBPD, GFI, and KLF14 in HSPC (Figure 6B). These TF have been previously described to regulate survival and proliferation of HSPC, their differentiation toward the myeloid lineage, and their inflammatory phenotype.[30–34] We also evaluated the chromatin profiling of mature monocytes isolated from mice 1 month after stroke or control conditions. Consistent with the findings in HSPCs, we found that H3K4me3 levels in monocytes were tightly linked to diverse TF motifs after stroke, including CTCF and several regions associated with the NF-κb and IL-1 signaling pathways and a pro-inflammatory response, such as E2F2, ATF7, STAT1, and KLF14 (Figure 6C).[32,34–36]

We previously identified systemic inflammasome activation and subsequent IL-1β secretion in response to tissue injury including stroke, with serum IL-1β concentrations peaking within the first hours after injury to similar peak levels as observed after stimulation with lipopolysaccharide (Figures S6C and S6D).[2] Studies in experimental infection models have suggested IL-1β-mediated effects to be involved in epigenetic reprogramming.[17] Therefore, we performed single-cell assay for transposase-accessible chromatin with sequencing (ATAC-seq) for analysis of open chromatin accessibility in control mice and in animals 1 month after stroke that either received IL-1β neutralizing antibodies or vehicle control. We obtained a total of 13,520 nuclei from $Lin^{-}CD45^{+}CD11b^{+}$ BM cells and identified a total of 11 clusters, which were superimposed on the BM mRNA sequencing uniform manifold approximation and projection (UMAP) plot (see Figure 5A), confirming coverage of the complete BM cell heterogeneity (Figure 6D). We identified in the HSPC as well as in the mature $Ly6C^{high}$ monocyte clusters distinct differences in chromatin accessibility 1 month after stroke compared with control mice (Figures S6E and S6F; Table S4). Next, we particularly focused on potentially important cell-type-specific differentially active regulatory sequences,[37] and identified significant changes in TF motifs between stroke and control conditions (Figure 6E). These analyses confirm our findings that stroke induces a pronounced alteration in the activity of several TF in hematopoietic stem cells (HSCs), including CTCF, ETV4, and RUNX2, which have been previously described to regulate HSPC function.[38–40] Similarly, we also confirmed that

Figure 5. Stroke induces persistent innate immune memory

(A) Schematic experimental design: lymphoid lineage- (CD3, CD4, CD8a, CD19, and Ter119) and neutrophil- (Ly6G) negative myeloid cells were sorted from the BM of control and stroke mice 1 month after stroke ($n = 8$) for single-cell mRNA sequencing. UMAP plot of the 22,169 myeloid cells sorted from the BM of control and stroke mice.

(B) Monocle3 pseudo-temporal ordering of myeloid BM cells, superimposed on the UMAP plot. Cells are colored based on their progression along pseudo-temporal space (left) or by cell types (right).

(C) Number of differentially expressed genes (DEGs) between conditions per cell type (adj. $p < 0.05$).

(D) Quantification of monocyte and neutrophil cell counts between conditions (U test; $n = 9/13$ per group).

(E) Schematic of the differentiation path of hematopoietic stem cells (HSCs) toward monocytes (Mo) and neutrophils (Neu) (left) and quantifications of HSC-multipotent progenitors 1 (MPP1), common myeloid progenitors (CMPs), and granulocyte-monocyte progenitors (GMPs) (U test; $n = 9/13$ per group).

(F) Schematic experimental design: bone marrow (BM) cells enriched for HSPCs were isolated from stroke and control actin-GFP mice and transplanted into BM-depleted $Mx1^{Cre}$:c-$myb^{fl/fl}$ mice. 1 month after transplantation, mice were sacrificed, and GFP-positive myeloid cells from BM, blood, and heart were isolated and analyzed using single-cell mRNA sequencing and flow cytometry.

(G) UMAP plot of 25,358 myeloid GFP+ cells from the BM of transplanted mice, colored by identified populations and superimposed on the UMAP plot of the myeloid cells from the endogenous BM (cells in gray, Figure 5A for reference).

(H) Dot plot showing the expression of selected genes in the $Ly6C^{high}$ monocytic populations from the endogenous BM of stroke and control mice (left column) and the BM of recipient mice transplanted with stroke and control GFP^{+} HSPC-enriched BM cells (right column). Genes were selected from the enriched GO terms in the set of DEGs between conditions in $Ly6C^{high}$ monocytes (adjusted $p < 0.1$). The dot size corresponds to the fraction of cells within each condition, and the color indicates average expression.

(I) Monocle3 pseudo-temporal ordering of GFP^{+} cells from recipient mice, superimposed on the UMAP plot and split by condition. Cells are colored based on their progression along pseudo-temporal space.

(J) Quantification of the flow cytometry analysis of GFP^{+} cardiac monocytes/macrophages from recipient mice transplanted with stroke or control BM cells.

(K and L) Representative images for single-molecule fluorescence *in situ* hybridization (smFISH) (left, scale bars, 5 μm) and quantification of the number of *Mmp9* puncta per *Cx3cr1*$^{+}$ cardiac cells (K; U test, $n = 5/7$ per group) and GFP^{+} cardiac cells (L; U test, $n = 5/6$ per group).

(M) Representative images (Sirius red/fast green staining) and quantification of cardiac fibrosis in the left ventricle (LV) free wall of recipient mice (t test, $n = 5/7$ per group, 3/4 heart sections per mouse).

See also Figures S4 and S5.

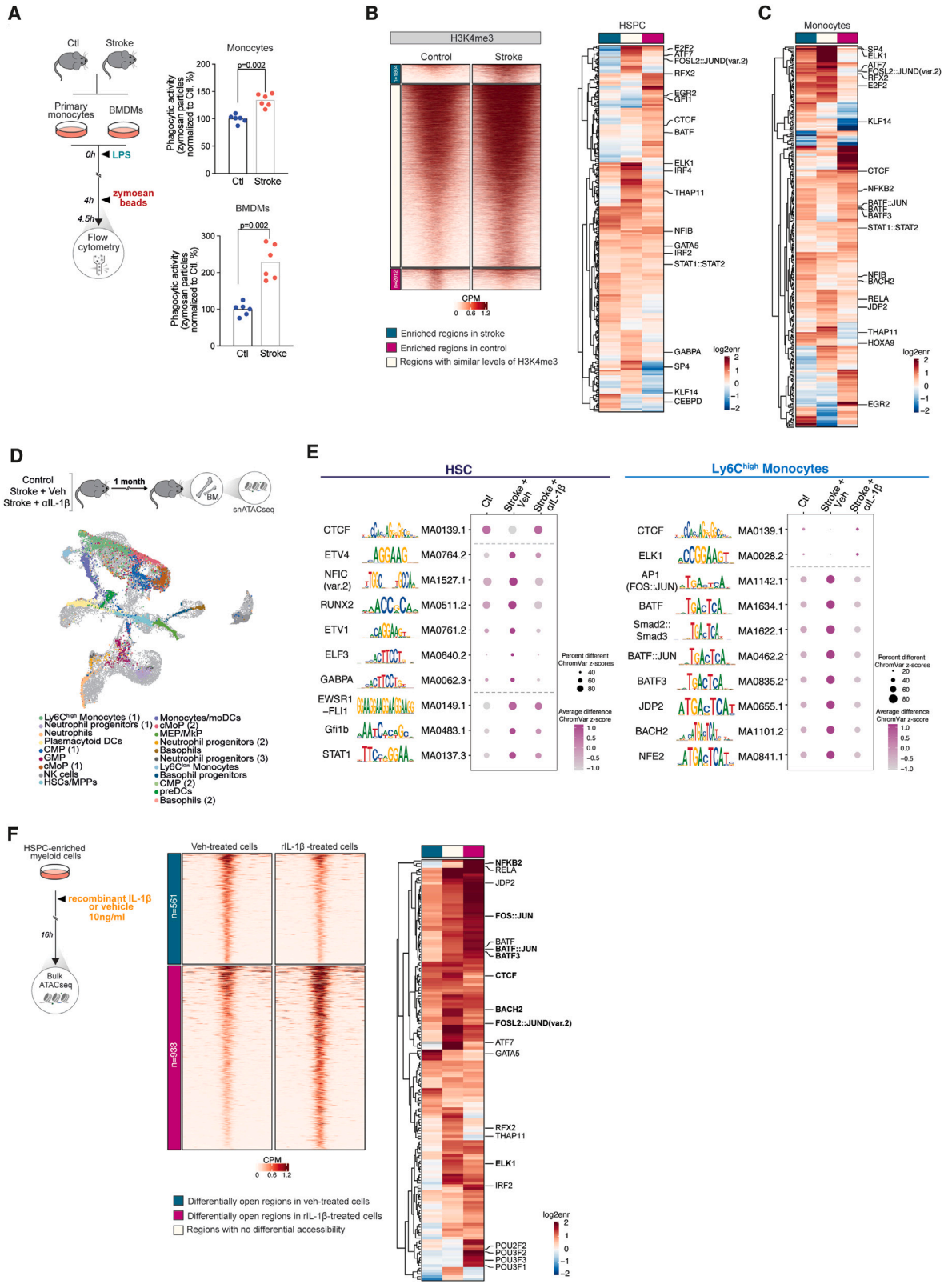

(legend on next page)

stroke changed the epigenetic landscape of mature Ly6C^{high} monocytes by changing the motif accessibility associated with TF involved in stress and immune responses, such as CTCF, NRF1 (also known as NFE2), and FOS:JUND(AP1).[41–46] Importantly, IL-1β neutralization prevented most of the stroke-induced changes in chromatin accessibility in both HSPC and mature Ly6C^{high} monocytes (Figure 6E). To explore stroke-regulated TFs, we identified genes with differential expression between control and stroke conditions linked to these TFs. These genes were involved in inflammation and cytokine signaling, including IL-1β signaling (Figures S6G and S6H).

Finally, to confirm that IL-1β drives the epigenetic reprogramming observed after stroke, we used bulk ATAC-seq of the HSPC-enriched myeloid fraction of BM (i.e., HSPCs) cells treated with recombinant IL-1β. We observed significant alterations in chromatin accessibility across a range of genomic regions in HSPCs treated with IL-1β, although most of the changes were quantitative (Figure 6F). This analysis revealed an enrichment of TF motifs in IL-1β-treated HSPCs that are consistent with those identified in both the analysis of histone modification sites and the single-cell ATAC-seq analyses after experimental stroke. Altogether, these results demonstrate the critical role of IL-1β in inducing epigenetic changes leading to post-stroke-trained immunity.

IL-1β-driven innate immune memory mediates remote organ dysfunction after stroke

Beyond its role in post-stroke-trained immunity, we aimed to further test the role of IL-1β in the post-stroke increased myelopoiesis and monocyte recruitment to the heart. Therefore, we evaluated the heart and BM myeloid composition 1 week after injection of recombinant IIL-1β live mice without a stroke (Figure 7A). By flow cytometry, we observed a substantial increase in the Ly6C^{high} cardiac monocytes and CCR2^{high} monocytes/macrophages in the hearts rIL-1β-treated mice (Figure 7B) and found correspondingly increased myelopoiesis, characterized by elevated counts of HSPCs and mature monocytes after rIL-1β injection (Figure 7C). Notably, we observed efficient normalization of BM cellularity to levels of control mice in stroke animals receiving acute IL-1β neutralization by rIL-1β-specific antibodies (Figures 7D, 7E, S7A, and S7B). In turn, anti-IL-1β treatment during the acute phase reduced circulating Ly6C^{high} monocyte counts 1 month post-stroke (Figure 7F), and the post-stroke increase in CCR2^{high} cardiac monocytes/macrophages was also restored to control levels after IL-1β neutralization (Figure 7G). Correspondingly, preventing release by blocking caspase-1 activation by administration of the caspase-1 inhibitor VX-765,[2] similarly prevented the post-stroke increase in myelopoiesis (Figure S7C). Of note, delayed neutralization of IL-1β levels at 2 weeks after stroke failed to rescue the post-stroke increase in myelopoiesis (Figure S7D), confirming that the post-stroke inflammasome-dependent acute IL-1β release but not a chronic stimulation by potentially residual circulatory IL-1β primes the post-stroke increase in myelopoiesis and cardiac pathology.

Finally, we observed that acute (but not delayed) neutralization of the early IL-1β release was sufficient to prevent the long-term cardiac phenotype by significantly reducing *Mmp9* expression of cardiac monocytes/macrophages and cardiac fibrosis to levels of control mice without a stroke (Figures 7H, 7I, and S7E). These findings suggest that the IL-1β-driven epigenetic changes leading to trained immunity can be causally involved in mediating the chronic cardiac fibrosis after stroke.

Blocking BM-to-heart trafficking of monocytes prevents post-stroke cardiac dysfunction

Despite its striking efficacy on innate immune memory and cardiac secondary comorbidities, the translational use of neutralizing IL-1β in stroke patients is limited by an increased risk of infections.[47] Therefore, we sought for alternative options by blocking the migration of pro-inflammatory myeloid cells to secondary organs using the dual C-C chemokine receptors type 2 and 5 antagonist cenicriviroc (CVC), which has been developed and proven safe for HIV infections and for steatohepatitis.[48–50] We found that daily treatment with CVC after experimental stroke substantially reduced monocyte recruitment to the heart (Figures 7J, 7K, S7F, and S7G). This effect is likely attributable to blocking the chemokine-dependent invasion of monocytes to secondary organs because CVC increased circulating Ly-6-C^{high} monocyte counts and had no direct cytotoxic effect on monocytes (Figures S7H and S7I). Consequently, CVC treatment significantly reduced *Mmp9* expression by cardiac monocytes/macrophages and reduced cardiac fibrosis (Figures 7L, 7M, and S7J). Importantly, this therapeutic reduction in inflammatory

Figure 6. Innate immune memory is mediated by early post-stroke IL-1β secretion

(A) Schematic experimental design: bone marrow-derived macrophages (BMDMs) and primary monocytes were isolated from mice 1 month after stroke or control. Uptake of zymosan beads was quantified by flow cytometry (t test, $n = 6$ per group).

(B) Density heatmaps for enriched H3K4me3 peaks in lymphoid lineage- (CD3, CD4, CD8a, CD19, and Ter119) and neutrophil- (Ly6G) negative myeloid cells from mice 1-month post-stroke (up, green) or control mice (down, pink), split by condition.

(C) Heatmap of motif enrichment for H3K4me3 peaks for HSPCs between mice 1-month post-stroke and control mice and (C) corresponding heatmap for Ly6C^{high} monocytes.

(D) Schematic experimental design: mice received IL-1β neutralizing antibodies or vehicle 1 h before and 1 h after stroke induction. 1 month later, nuclei were isolated from lineage-negative myeloid cells ($n = 3$/group) for single-nuclei ATAC sequencing. UMAP plot of 13,520 myeloid nuclei, colored by identified populations and superimposed on the UMAP plot of the myeloid cells from the endogenous BM of control and stroke mice (cells in gray, Figure 5A).

(E) Dot plot showing per-cell differential motif activity scores between experimental conditions in HSCs (left) and Ly6C^{high} monocytes (right). Identified motifs with the highest and lowest activity scores between control and vehicle-treated strokes are represented (adj. $p < 0.05$).

(F) Schematic experimental design: HSPC-enriched myeloid cells were cultured with either recombinant (r)IL-1β or vehicle for 16 h and analyzed by ATAC sequencing (left). Density heatmaps for differentially open chromatin regions split by condition (middle). Heatmap of motif enrichment for differentially accessible peaks between groups (right).

See also Figure S6.

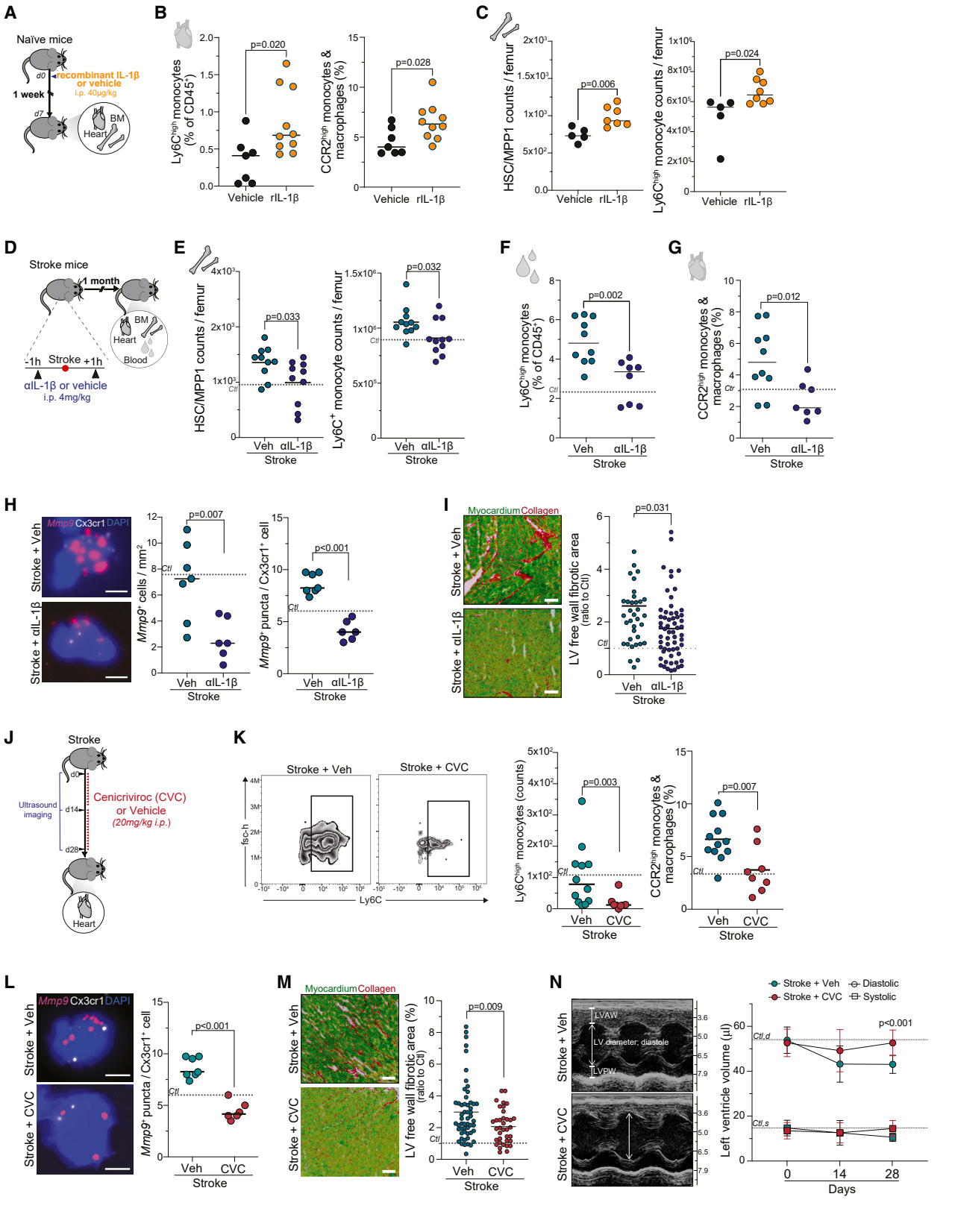

(legend on next page)

cardiac ECM remodeling by CVC also significantly improved diastolic cardiac function in the chronic phase after stroke to comparable levels of control mice without a stroke (Figure 7N). In summary, these results demonstrate the therapeutic potential of blocking the BM-to-heart migration of pro-inflammatory programmed monocytes as a strategy to prevent secondary cardiac comorbidity following stroke.

DISCUSSION

Systemic inflammation following a stroke has been identified as a critical factor affecting the short- and long-term prognosis of stroke patients.[51,52] Interestingly, many of the pre-existing or acquired health conditions that arise after a stroke share common inflammatory mechanisms. These mechanisms can potentially exacerbate the development of other medical complications, leading to a worsened long-term outcome. Consequently, addressing systemic inflammation has emerged as a focus for translational research, with initial clinical trials already conducted to minimize functional disabilities in patients and prevent secondary complications.[3]

Our study reveals that stroke triggers persistent inflammation in multiple organs by inducing innate immune memory. Specifically, we discovered that IL-1β-mediated epigenetic changes in the myeloid compartment play a role in cardiac fibrosis, leading to diastolic dysfunction following ischemic brain injury.

Cardiovascular diseases, such as atrial fibrillation, valvular heart disease, and congestive heart failure, are well-known risk factors for ischemic stroke.[53,54] However, this relationship is bidirectional, as the incidence of cardiovascular disorders also increases after an initial stroke.[55,56] After a stroke, more than 60% of patients experience electrocardiographic (ECG) abnormalities,[9] 25% are diagnosed with serious arrhythmias,[57] and approximately 19% develop at least one significant cardiac adverse event.[10] Interestingly, a previous report demonstrated a causal role of monocytes to the development of atrial arrythmias.[27] Previous studies in mice have demonstrated that stroke results in chronic systolic dysfunction lasting up to 8 weeks after the brain injury, leading to a delayed reduction in left ventricular ejection fraction and an increase in left ventricular volume.[58,59] The SICFAIL study, a prospective clinical study involving 696 stroke patients, demonstrated a surprisingly high incidence of cardiac dysfunction after stroke. Diastolic dysfunction was found to be the most prevalent type of cardiac dysfunction, affecting 23% of patients without signs of systolic dysfunction.[60] This study clearly highlights the burden of secondary cardiac dysfunction following ischemic stroke. Although diastolic dysfunction is highly prevalent, it is not routinely assessed in stroke patients,[61,62] and its clinical relevance in patients with acute ischemic stroke is not well understood. In our study—investigating a small subgroup of the SICFAIL cohort—we observed that in principle progressive diastolic dysfunction can also occur in stroke patients, similar to our experimental stroke model. Similarly, we demonstrated in a cohort of autopsy samples the development of cardiac fibrosis after stroke.

Patients with chronic systemic inflammatory diseases, such as rheumatoid arthritis, psoriasis, or psoriatic arthritis, are known to have an increased risk of cardiovascular disease. For example, a recent population-based cohort study described an increased incidence of cardiovascular disease in patients with inflammatory bowel disease even in the absence of common risk factors like obesity, lipid disturbances, or hypertension, suggesting that inflammation may be a key factor underlying the development of these cardiovascular complications.[18,63] Therefore, it is reasonable to consider that the systemic inflammatory response triggered by the ischemic brain lesion itself may further predispose stroke patients to secondary (inflammatory) vascular events.

Figure 7. IL-1β-driven innate immune memory mediates cardiac dysfunction after stroke

(A) Schematic experimental design: naive WT mice received rIL-1β or vehicle intraperitoneally (i.p.) and organs collected 7 days later for flow cytometry.

(B) Quantification of Ly6C^{high} monocytes (CD45$^+$ Ly6G$^-$ CD11b$^+$ F4/80$^-$ Ly6C^{high}) and CCR2^{high} monocytes/macrophages (CD45$^+$ Ly6G$^-$ CD11b$^+$ F4/80$^+$ CCR2^{high}) between groups (t test, n = 7/10 per group).

(C) Quantification of HSC-multipotent progenitors 1 (HSC-MPP1) and Ly6C^{high} monocytes in BM (t test, n = 5/8 per group).

(D) Schematic experimental design: mice received IL-1β-specific neutralizing antibodies or vehicle 1 h before and 1 h after stroke induction, and organs were collected for analysis 1 month later.

(E–G) (E) HSC-multipotent progenitors 1 (HSC-MPP1) and total monocytes in BM from stroke mice (U test; n = 10/11 per group) and (F) Ly6C^{high} monocytes (CD45$^+$ Ly6G$^-$ CD11b$^+$ Ly6C^{high}) in blood (t test; n = 10/8 per group) and (G) CCR2^{high} monocytes/macrophages (CD45$^+$ Ly6G$^-$ CD11b$^+$ F4/80$^+$ CCR2^{high}) in hearts (t test; n = 10/7 per group).

(H) Representative images and quantification of Mmp9 mRNA expression in Cx3cr1+ cardiac myeloid cells between treatment groups by single-molecule fluorescence *in situ* hybridization (smFISH, scale bars, 5 μm, U test, n = 6/7 per group).

(I) Representative images (Sirius red/fast green staining) and quantification of cardiac fibrosis in the left ventricle (LV) free wall (t test, n = 8/14 per group, 4 heart sections per mouse).

(J) Schematic experimental design: stroke mice were administered daily with the dual C-C chemokine receptors type 2 and 5 antagonist cenicriviroc (stroke + CVC) or vehicle (stroke + Veh) for 28 days. Cardiac ultrasound imaging was performed at days 0, 14, and 28. Hearts were collected at 28 days for flow cytometry and histological analysis.

(K) Gating strategy for Ly6C^{high} monocytes in CVC- and vehicle-treated stroke mice and corresponding quantification (U test; n = 8–12 per group).

(L) Representative smFISH images and quantification of the number of *Mmp9* puncta per *Cx3cr1*$^+$ cardiac myeloid cell (U test, n = 6/7 per group).

(M) Representative images (Sirius red/fast green staining) and quantification of cardiac fibrosis in the LV free wall in CVC- and vehicle-treated stroke mice. Dashed line indicates mean percentage of fibrotic area in control mice (t test, n = 9/14 per group, 4 heart sections per mouse).

(N) Representative ultrasound images (M-mode) performed at days 0, 14, and 28 after stroke on CVC- and vehicle-treated stroke mice (left). Quantification of the left ventricle (LV) volume in systole (squares) and diastole (circles). Dashed line indicates mean LV volume in control mice at day 28. Multiple t tests, n = 6/12 per group. LVAW, left ventricle anterior wall; LVPW, left ventricle posterior wall.

See also Figure S7.

Here, we demonstrate that persistent pro-inflammatory changes in myeloid cells after stroke are a causal factor for the development of cardiac fibrosis independent of other predisposing factor for cardiovascular disorders. Innate immune memory—defined as long-term changes in the innate immune cell compartment that alter its responsiveness to a second stimulation—has so far been described in infection models and in vaccination,[13] but was so far not recognized as a pathogenic mechanism after sterile tissue injuries including stroke. Importantly, innate (trained) immunity to a pathogen not only heightens innate immune responsiveness to the same pathogen but was demonstrated to also affect unrelated inflammatory processes, as, for example, the disease-modifying effect of periodontitis for atherosclerosis progression.[17] In this study, we make the observation of innate immune memory in response to a sterile tissue injury, which links this acute event to the development of a chronic, secondary pathology at a remote organ site.

Our study highlights IL-1β-mediated epigenetic changes and the recruitment of reprogrammed cells to the healthy heart as critical events in the development of chronic secondary organ dysfunction after a stroke. Notably, epigenetic changes induced by the acute surge of IL-1β post-stroke are comparable to the observed epigenetic modifications in previous studies using infection models.[64,65] Based on our findings, targeting IL-1β systemically can potentially prevent post-stroke epigenetic changes and the resulting pro-inflammatory effects on remote organ homeostasis. This aligns well with previous research demonstrating the cardiovascular benefits observed in the CANTOS trial using anti-IL-1β therapy.[47] However, the trial also revealed significant risks of increased infection rates associated with this non-specific approach that targets a key pro-inflammatory cytokine involved in pathogen clearance. This limitation poses a challenge for the further development of this approach in translational research.

Therefore, in our study, we explored an alternative strategy to limit the recruitment of monocytes from BM and circulation to remote organs by using a dual chemokine inhibitor targeting CCR2/5 (CVC).[48] Notably, genetic studies have provided evidence of the involvement of CCL2-CCR2 signaling in various cardiovascular disorders, suggesting that targeting this signaling pathway could have beneficial effects on monocyte recruitment.[66] Moreover, CVC has demonstrated safety and efficacy in other conditions, including HIV and hepatosteatosis.[48–50]

In conclusion, our study provides mechanistic insights into immune-mediated secondary comorbidities following stroke, such as cardiac dysfunction and potentially others. We have identified innate immune memory as a causal mechanism underlying chronic changes in resident innate immune cells across multiple organs, which contribute to the development or progression of secondary organ dysfunction. These discoveries offer a therapeutic rationale for the secondary prevention of post-stroke comorbidities.

Limitations of the study

There are several limitations to our study. While our results propose IL-1β as a principal mediator of trained immunity and its significance for cardiac pathology after stroke, we did not test in this study the generalizability of this IL-1β-mediated pathway to other conditions of acute tissue injury or infection models. Also, the exact molecular mechanisms by which IL-1β induces epigenetic changes and altered hematopoiesis remain unclear, including the intracellular mechanisms as well as potential effects on structural BM organization and interaction of HSCs with stromal cells. Similarly, the effects of stroke on long-term myelopoiesis and trained immunity in humans are so far unknown. In relation to the cardiac phenotype of diastolic dysfunction and delayed cardiac fibrosis after stroke, this phenotype remains to be validated in human stroke patients in a prospective clinical study; also, a potential mechanistic relationship between early systolic and later diastolic cardiac dysfunction remains so far unexplored. Our study found no indications for a direct effect of changes in the autonomic nervous system on post-stroke-trained immunity or chronic diastolic dysfunction, although we cannot exclude a contribution of the autonomic nervous system on myelopoiesis, structural remodeling of BM stromal cells, or other peripheral immune compartments (e.g., the spleen and intestine) that might indirectly contribute to the phenotype observed in the chronic phase post-stroke.

STAR★METHODS

Detailed methods are provided in the online version of this paper and include the following:

- KEY RESOURCES TABLE
- RESOURCE AVAILABILITY
  - Lead contact
  - Materials availability
  - Data and code availability
- EXPERIMENTAL MODEL AND STUDY PARTICIPANTS DETAILS
  - Clinical patient population
  - Animal experiments
- METHOD DETAILS
  - Transient proximal cerebral artery occlusion model
  - Permanent distal cerebral artery occlusion model
  - Drug administrations
  - Tamoxifen
  - Echocardiography
  - ECG telemetry
  - Cardiac electrophysiology studies
  - Non-invasive blood pressure measurements
  - BM transplantation
  - Organ and tissue collection
  - Cell isolation
  - Cell sorting
  - Flow cytometry
  - Single-cell RNA sequencing
  - Single-cell RNA-seq data analysis
  - Single-nuclei ATAC-seq
  - Single-nuclei ATAC-seq data analysis
  - Bulk ATAC sequencing
  - CUT&tag sequencing
  - Second harmonic generation microscopy imaging
  - Mouse heart histological sections
  - Human heart histological sections
  - Picrosirius red staining
  - Hematoxylin and eosin staining
  - Immunofluorescence staining
  - Immunohistochemical staining
  - RNA-fluorescence *in situ* hybridization
  - MMP9 gelatin zymography
  - Blood urea measurement

SUPPLEMENTAL INFORMATION

Supplemental information can be found online at https://doi.org/10.1016/j.cell.2024.06.028.

ACKNOWLEDGMENTS

The authors thank Christina Fürle and Kerstin Thuß-Silczak for excellent technical support and Burkhardt Becher (University of Zurich) for providing $Ccr2^{creERT2}$xAi14 mice. The study was supported by the Vascular Dementia Research Foundation, the European Research Council (ERC-StG 802305), the German Research Foundation (DFG) under Germany's Excellence Strategy (EXC 2145 SyNergy ID 390857198 and EXC2151 ImmunoSensation ID 390873048), FOR 2879 (ID 405358801), CRC 1123 (ID 238187445), TRR 274 (ID 408885537), TRR 355 (ID 490846870), TRR 332 (INST 211/1066-1), a Walter-Benjamin Fellowship (SI 2832/1), the Corona Foundation (S199/10079/2019), the Munich School for Data Science (MUDS), the China Scholarship Council, and the UNION-CVD Clinician Scientist Programme (ID 413657723). The SICFAIL study was funded by the German Ministry of Research and Education (Comprehensive Heart Failure Centre Würzburg, BMBF #01EO1004 and #01EO1504).

AUTHOR CONTRIBUTIONS

Conceptualization, A.S. and A.L.; investigation, A.S., S.Z., J.C., D.M., F.C., O.C., S.B., A.S.C., F.A.M., P.U.H., A.R., S.R., G.L., R.S., Y.C., and C.M.; formal analysis, A.S., S.Z., F.C., A.S.C., S.B.-G., H.S., E.B., S.R., G.L., F.A.M., and P.U.H.; resources, C.B., K.H., S.F., N.P., O.G., E.B., C.S., B.B., and S.C.; writing – original draft, A.S., S.Z., and A.L.; writing – review and editing, A.S., M.D., P.U.H., S.C., F.A.M., P.U.H., B.B., C.S., and A.L.; visualization, A.S., S.Z., F.C., B.B., and A.L.; supervision, S.C., B.B., C.S., and A.L.; funding acquisition, S.C., B.B., C.S., and A.L.

DECLARATION OF INTERESTS

The authors declare no competing interests.

Received: June 29, 2023
Revised: April 22, 2024
Accepted: June 21, 2024
Published: July 22, 2024

REFERENCES

1. Simats, A., and Liesz, A. (2022). Systemic inflammation after stroke: implications for post-stroke comorbidities. EMBO Mol. Med. *14*, e16269. https://doi.org/10.15252/emmm.202216269.
2. Roth, S., Cao, J., Singh, V., Tiedt, S., Hundeshagen, G., Li, T., Boehme, J.D., Chauhan, D., Zhu, J., Ricci, A., et al. (2021). Post-injury immunosuppression and secondary infections are caused by an AIM2 inflammasome-driven signaling cascade. Immunity *54*, 648–659.e8. https://doi.org/10.1016/j.immuni.2021.02.004.
3. Iadecola, C., Buckwalter, M.S., and Anrather, J. (2020). Immune responses to stroke: mechanisms, modulation, and therapeutic potential. J. Clin. Invest. *130*, 2777–2788. https://doi.org/10.1172/JCI135530.
4. Liesz, A., Rüger, H., Purrucker, J., Zorn, M., Dalpke, A., Möhlenbruch, M., Englert, S., Nawroth, P.P., and Veltkamp, R. (2013). Stress mediators and immune dysfunction in patients with acute cerebrovascular diseases. PLoS One *8*, e74839. https://doi.org/10.1371/journal.pone.0074839.
5. Stanne, T.M., Angerfors, A., Andersson, B., Brännmark, C., Holmegaard, L., and Jern, C. (2022). Longitudinal study reveals long-term proinflammatory proteomic signature after ischemic stroke across subtypes. Stroke *53*, 2847–2858. https://doi.org/10.1161/STROKEAHA.121.038349.
6. Roth, S., Singh, V., Tiedt, S., Schindler, L., Huber, G., Geerlof, A., Antoine, D.J., Anfray, A., Orset, C., Gauberti, M., et al. (2018). Brain-released alarmins and stress response synergize in accelerating atherosclerosis progression after stroke. Sci. Transl. Med. *10*, 1–12. https://doi.org/10.1126/scitranslmed.aao1313.
7. Holmegaard, L., Stanne, T.M., Andreasson, U., Zetterberg, H., Blennow, K., Blomstrand, C., Jood, K., and Jern, C. (2021). Proinflammatory protein signatures in cryptogenic and large artery atherosclerosis stroke. Acta Neurol. Scand. *143*, 303–312. https://doi.org/10.1111/ane.13366.
8. Tatemichi, T.K., Paik, M., Bagiella, E., Desmond, D.W., Pirro, M., and Hanzawa, L.K. (1994). Dementia after stroke is a predictor of long-term survival. Stroke *25*, 1915–1919. https://doi.org/10.1161/01.STR.25.10.1915.
9. Braga, G.P., Gonçalves, R.S., Minicucci, M.F., Bazan, R., and Zornoff, L.A.M. (2020). Strain pattern and T-wave alterations are predictors of mortality and poor neurologic outcome following stroke. Clin. Cardiol. *43*, 568–573. https://doi.org/10.1002/clc.23348.
10. Prosser, J., MacGregor, L., Lees, K.R., Diener, H.C., Hacke, W., and Davis, S. (2007). Predictors of early cardiac morbidity and mortality after ischemic stroke. Stroke *38*, 2295–2302. https://doi.org/10.1161/STROKEAHA.106.471813.
11. Suissa, L., Panicucci, E., Perot, C., Romero, G., Gazzola, S., Laksiri, N., Rey, C., Doche, E., Mahagne, M.-H., Pelletier, J., et al. (2020). Effect of hyperglycemia on stroke outcome is not homogeneous to all patients treated with mechanical thrombectomy. Clin. Neurol. Neurosurg. *194*, 105750. https://doi.org/10.1016/j.clineuro.2020.105750.
12. Hackett, M.L., and Pickles, K. (2014). Part I: frequency of depression after stroke: an updated systematic review and meta-analysis of observational studies. Int. J. Stroke *9*, 1017–1025. https://doi.org/10.1111/ijs.12357.
13. Netea, M.G., Joosten, L.A.B., Latz, E., Mills, K.H.G., Natoli, G., Stunnenberg, H.G., O'Neill, L.A.J., and Xavier, R.J. (2016). Trained immunity: A program of innate immune memory in health and disease. Science *352*, aaf1098. https://doi.org/10.1126/science.aaf1098.
14. Netea, M.G., Domínguez-Andrés, J., Barreiro, L.B., Chavakis, T., Divangahi, M., Fuchs, E., Joosten, L.A.B., van der Meer, J.W.M., Mhlanga, M.M., Mulder, W.J.M., et al. (2020). Defining trained immunity and its role in health and disease. Nat. Rev. Immunol. *20*, 375–388. https://doi.org/10.1038/s41577-020-0285-6.
15. Ochando, J., Fayad, Z.A., Madsen, J.C., Netea, M.G., and Mulder, W.J.M. (2020). Trained immunity in organ transplantation. Am. J. Transplant. *20*, 10–18. https://doi.org/10.1111/ajt.15620.
16. Leung, Y.T., Shi, L., Maurer, K., Song, L., Zhang, Z., Petri, M., and Sullivan, K.E. (2015). Interferon regulatory factor 1 and histone H4 acetylation in systemic lupus erythematosus. Epigenetics *10*, 191–199. https://doi.org/10.1080/15592294.2015.1009764.
17. Li, X., Wang, H., Yu, X., Saha, G., Kalafati, L., Ioannidis, C., Mitroulis, I., Netea, M.G., Chavakis, T., and Hajishengallis, G. (2022). Maladaptive innate immune training of myelopoiesis links inflammatory comorbidities. Cell *185*, 1709–1727.e18. https://doi.org/10.1016/j.cell.2022.03.043.
18. Murphy, A.J., and Tall, A.R. (2016). Disordered haematopoiesis and athero-thrombosis. Eur. Heart J. *37*, 1113–1121. https://doi.org/10.1093/eurheartj/ehv718.
19. Winklewski, P.J., Radkowski, M., and Demkow, U. (2014). Cross-talk between the inflammatory response, sympathetic activation and pulmonary infection in the ischemic stroke. J. Neuroinflammation *11*, 213. https://doi.org/10.1186/s12974-014-0213-4.

20. Seifert, H.A., and Offner, H. (2018). The splenic response to stroke: from rodents to stroke subjects. J. Neuroinflammation *15*, 195. https://doi.org/10.1186/s12974-018-1239-9.

21. Austin, V., Ku, J.M., Miller, A.A., and Vlahos, R. (2019). Ischaemic stroke in mice induces lung inflammation but not acute lung injury. Sci. Rep. *9*, 3622. https://doi.org/10.1038/s41598-019-40392-1.

22. Llovera, G., Hofmann, K., Roth, S., Salas-Pérdomo, A., Ferrer-Ferrer, M., Perego, C., Zanier, E.R., Mamrak, U., Rex, A., Party, H., et al. (2015). Results of a preclinical randomized controlled multicenter trial (pRCT): anti-CD49d treatment for acute brain ischemia. Sci. Transl. Med. *7*, 299ra121. https://doi.org/10.1126/scitranslmed.aaa9853.

23. Ginhoux, F., Schultze, J.L., Murray, P.J., Ochando, J., and Biswas, S.K. (2016). New insights into the multidimensional concept of macrophage ontogeny, activation and function. Nat. Immunol. *17*, 34–40. https://doi.org/10.1038/ni.3324.

24. Hoyer, F.F., Naxerova, K., Schloss, M.J., Hulsmans, M., Nair, A.V., Dutta, P., Calcagno, D.M., Herisson, F., Anzai, A., Sun, Y., et al. (2019). Tissue-specific macrophage responses to remote injury impact the outcome of subsequent local immune challenge. Immunity *51*, 899–914.e7. https://doi.org/10.1016/j.immuni.2019.10.010.

25. Paulus, W.J., and Tschöpe, C. (2013). A novel paradigm for heart failure with preserved ejection fraction: comorbidities drive myocardial dysfunction and remodeling through coronary microvascular endothelial inflammation. J. Am. Coll. Cardiol. *62*, 263–271. https://doi.org/10.1016/j.jacc.2013.02.092.

26. Sharma, K., and Kass, D.A. (2014). Heart failure with preserved ejection fraction: mechanisms, clinical features, and therapies. Circ. Res. *115*, 79–96. https://doi.org/10.1161/CIRCRESAHA.115.302922.

27. Hulsmans, M., Schloss, M.J., Lee, I.-H., Bapat, A., Iwamoto, Y., Vinegoni, C., Paccalet, A., Yamazoe, M., Grune, J., Pabel, S., et al. (2023). Recruited macrophages elicit atrial fibrillation. Science *381*, 231–239. https://doi.org/10.1126/science.abq3061.

28. Epelman, S., Lavine, K.J., Beaudin, A.E., Sojka, D.K., Carrero, J.A., Calderon, B., Brija, T., Gautier, E.L., Ivanov, S., Satpathy, A.T., et al. (2014). Embryonic and adult-derived resident cardiac macrophages are maintained through distinct mechanisms at steady state and during inflammation. Immunity *40*, 91–104. https://doi.org/10.1016/j.immuni.2013.11.019.

29. Park, M.D., Silvin, A., Ginhoux, F., and Merad, M. (2022). Macrophages in health and disease. Cell *185*, 4259–4279. https://doi.org/10.1016/j.cell.2022.10.007.

30. Stik, G., Vidal, E., Barrero, M., Cuartero, S., Vila-Casadesús, M., Mendieta-Esteban, J., Tian, T.V., Choi, J., Berenguer, C., Abad, A., et al. (2020). CTCF is dispensable for immune cell transdifferentiation but facilitates an acute inflammatory response. Nat. Genet. *52*, 655–661. https://doi.org/10.1038/s41588-020-0643-0.

31. Jaitin, D.A., Weiner, A., Yofe, I., Lara-Astiaso, D., Keren-Shaul, H., David, E., Salame, T.M., Tanay, A., Van Oudenaarden, A., and Amit, I. (2016). Dissecting immune circuits by linking CRISPR-pooled screens with single-cell RNA-seq. Cell *167*, 1883–1896.e15. https://doi.org/10.1016/j.cell.2016.11.039.

32. Yuan, Y., Fan, G., Liu, Y., Liu, L., Zhang, T., Liu, P., Tu, Q., Zhang, X., Luo, S., Yao, L., et al. (2022). The transcription factor KLF14 regulates macrophage glycolysis and immune function by inhibiting HK2 in sepsis. Cell. Mol. Immunol. *19*, 504–515. https://doi.org/10.1038/s41423-021-00806-5.

33. Yang, Z.-F., Drumea, K., Cormier, J., Wang, J., Zhu, X., and Rosmarin, A.G. (2011). GABP transcription factor is required for myeloid differentiation, in part, through its control of Gfi-1 expression. Blood *118*, 2243–2253. https://doi.org/10.1182/blood-2010-07-298802.

34. Chen, S., Yang, J., Wei, Y., and Wei, X. (2020). Epigenetic regulation of macrophages: from homeostasis maintenance to host defense. Cell. Mol. Immunol. *17*, 36–49. https://doi.org/10.1038/s41423-019-0315-0.

35. Yoshida, K., and Ishii, S. (2016). Innate immune memory via ATF7-dependent epigenetic changes. Cell Cycle *15*, 3–4. https://doi.org/10.1080/15384101.2015.1112687.

36. Li, W., Moorlag, S.J.C.F.M., Koeken, V.A.C.M., Röring, R.J., De Bree, L.C.J., Mourits, V.P., Gupta, M.K., Zhang, B., Fu, J., Zhang, Z., et al. (2023). A single-cell view on host immune transcriptional response to in vivo BCG-induced trained immunity. Cell Rep. *42*, 112487. https://doi.org/10.1016/j.celrep.2023.112487.

37. Schep, A.N., Wu, B., Buenrostro, J.D., and Greenleaf, W.J. (2017). chromVAR: inferring transcription-factor-associated accessibility from single-cell epigenomic data. Nat. Methods *14*, 975–978. https://doi.org/10.1038/nmeth.4401.

38. Omatsu, Y., Aiba, S., Maeta, T., Higaki, K., Aoki, K., Watanabe, H., Kondoh, G., Nishimura, R., Takeda, S., Chung, U.I., et al. (2022). Runx1 and Runx2 inhibit fibrotic conversion of cellular niches for hematopoietic stem cells. Nat. Commun. *13*, 2654. https://doi.org/10.1038/s41467-022-30266-y.

39. Ciau-Uitz, A., Wang, L., Patient, R., and Liu, F. (2013). ETS transcription factors in hematopoietic stem cell development. Blood Cells Mol. Dis. *51*, 248–255. https://doi.org/10.1016/j.bcmd.2013.07.010.

40. Ohlsson, R., Renkawitz, R., and Lobanenkov, V. (2001). CTCF is a uniquely versatile transcription regulator linked to epigenetics and disease. Trends Genet. *17*, 520–527. https://doi.org/10.1016/s0168-9525(01)02366-6.

41. Baillie, J.K., Arner, E., Daub, C., De Hoon, M., Itoh, M., Kawaji, H., Lassmann, T., Carninci, P., Forrest, A.R.R., Hayashizaki, Y., et al. (2017). Analysis of the human monocyte-derived macrophage transcriptome and response to lipopolysaccharide provides new insights into genetic aetiology of inflammatory bowel disease. PLoS Genet. *13*, e1006641. https://doi.org/10.1371/journal.pgen.1006641.

42. An, Y., Ni, Y., Xu, Z., Shi, S., He, J., Liu, Y., Deng, K.-Y., Fu, M., Jiang, M., and Xin, H.-B. (2020). TRIM59 expression is regulated by Sp1 and Nrf1 in LPS-activated macrophages through JNK signaling pathway. Cell. Signal. *67*, 109522. https://doi.org/10.1016/j.cellsig.2019.109522.

43. Nikolic, T., Movita, D., Lambers, M.E.H., Ribeiro de Almeida, C.R., Biesta, P., Kreefft, K., De Bruijn, M.J.W., Bergen, I., Galjart, N., Boonstra, A., et al. (2014). The DNA-binding factor Ctcf critically controls gene expression in macrophages. Cell. Mol. Immunol. *11*, 58–70. https://doi.org/10.1038/cmi.2013.41.

44. Dekkers, K.F., Neele, A.E., Jukema, J.W., Heijmans, B.T., and De Winther, M.P.J. (2019). Human monocyte-to-macrophage differentiation involves highly localized gain and loss of DNA methylation at transcription factor binding sites. Epigenetics Chromatin *12*, 34. https://doi.org/10.1186/s13072-019-0279-4.

45. Liao, J., Humphrey, S.E., Poston, S., and Taparowsky, E.J. (2011). Batf promotes growth arrest and terminal differentiation of mouse myeloid leukemia cells. Mol. Cancer Res. *9*, 350–363. https://doi.org/10.1158/1541-7786.MCR-10-0375.

46. Behmoaras, J., Bhangal, G., Smith, J., McDonald, K., Mutch, B., Lai, P.C., Domin, J., Game, L., Salama, A., Foxwell, B.M., et al. (2008). Jund is a determinant of macrophage activation and is associated with glomerulonephritis susceptibility. Nat. Genet. *40*, 553–559. https://doi.org/10.1038/ng.137.

47. Ridker, P.M., MacFadyen, J.G., Thuren, T., Everett, B.M., Libby, P., Glynn, R.J., Lorenzatti, A., Krum, H., and Varigos, J. (2017). Effect of interleukin-1β inhibition with canakinumab on incident lung cancer in patients with atherosclerosis: exploratory results from a randomised, double-blind, placebo-controlled trial. Lancet *390*, 1833–1842. https://doi.org/10.1016/S0140-6736(17)32247-X.

48. Thompson, M., Saag, M., DeJesus, E., Gathe, J., Lalezari, J., Landay, A.L., Cade, J., Enejosa, J., Lefebvre, E., and Feinberg, J. (2016). A 48-week randomized phase 2b study evaluating cenicriviroc versus efavirenz in treatment-naive HIV-infected adults with C-C chemokine receptor type 5-tropic virus. AIDS *30*, 869–878. https://doi.org/10.1097/QAD.0000000000000988.

49. Sherman, K.E., Abdel-Hameed, E., Rouster, S.D., Shata, M.T.M., Blackard, J.T., Safaie, P., Kroner, B., Preiss, L., Horn, P.S., and Kottilil, S. (2019). Improvement in hepatic fibrosis biomarkers associated with chemokine receptor inactivation through mutation or therapeutic blockade. Clin. Infect. Dis. *68*, 1911–1918. https://doi.org/10.1093/cid/ciy807.

50. Friedman, S.L., Ratziu, V., Harrison, S.A., Abdelmalek, M.F., Aithal, G.P., Caballeria, J., Francque, S., Farrell, G., Kowdley, K.V., Craxi, A., et al. (2018). A randomized, placebo-controlled trial of cenicriviroc for treatment of nonalcoholic steatohepatitis with fibrosis. Hepatology *67*, 1754–1767. https://doi.org/10.1002/hep.29477.

51. Dziedzic, T. (2015). Systemic inflammation as a therapeutic target in acute ischemic stroke. Expert Rev. Neurotherapeutics *15*, 523–531. https://doi.org/10.1586/14737175.2015.1035712.

52. Anrather, J., and Iadecola, C. (2016). Inflammation and stroke: an overview. Neurotherapeutics *13*, 661–670. https://doi.org/10.1007/s13311-016-0483-x.

53. Chugh, S.S., Roth, G.A., Gillum, R.F., and Mensah, G.A. (2014). Global burden of atrial fibrillation in developed and developing nations. Glob. Heart *9*, 113–119. https://doi.org/10.1016/j.gheart.2014.01.004.

54. Kim, W., and Kim, E.J. (2018). Heart failure as a risk factor for stroke. J. Stroke *20*, 33–45. https://doi.org/10.5853/jos.2017.02810.

55. Kallmünzer, B., Breuer, L., Kahl, N., Bobinger, T., Raaz-Schrauder, D., Huttner, H.B., Schwab, S., and Köhrmann, M. (2012). Serious cardiac arrhythmias after stroke: incidence, time course, and predictors-a systematic, prospective analysis. Stroke *43*, 2892–2897. https://doi.org/10.1161/STROKEAHA.112.664318.

56. Buckley, B.J.R., Harrison, S.L., Hill, A., Underhill, P., Lane, D.A., and Lip, G.Y.H. (2022). Stroke-heart syndrome: incidence and clinical outcomes of cardiac complications following stroke. Stroke *53*, 1759–1763. https://doi.org/10.1161/STROKEAHA.121.037316.

57. Ruthirago, D., Julayanont, P., Tantrachoti, P., Kim, J., and Nugent, K. (2016). Cardiac arrhythmias and abnormal electrocardiograms after acute stroke. Am. J. Med. Sci. *351*, 112–118. https://doi.org/10.1016/j.amjms.2015.10.020.

58. Bieber, M., Werner, R.A., Tanai, E., Hofmann, U., Higuchi, T., Schuh, K., Heuschmann, P.U., Frantz, S., Ritter, O., Kraft, P., et al. (2017). Stroke-induced chronic systolic dysfunction driven by sympathetic overactivity. Ann. Neurol. *82*, 729–743. https://doi.org/10.1002/ana.25073.

59. Veltkamp, R., Uhlmann, S., Marinescu, M., Sticht, C., Finke, D., Gretz, N., Gröne, H.J., Katus, H.A., Backs, J., and Lehmann, L.H. (2019). Experimental ischaemic stroke induces transient cardiac atrophy and dysfunction. J. Cachexia Sarcopenia Muscle *10*, 54–62. https://doi.org/10.1002/jcsm.12335.

60. Heuschmann, P.U., Montellano, F.A., Ungethüm, K., Rücker, V., Wiedmann, S., Mackenrodt, D., Quilitzsch, A., Ludwig, T., Kraft, P., Albert, J., et al. (2021). Prevalence and determinants of systolic and diastolic cardiac dysfunction and heart failure in acute ischemic stroke patients: the SICFAIL study. ESC Heart Fail. *8*, 1117–1129. https://doi.org/10.1002/ehf2.13145.

61. Jeong, E.-M., and Dudley, S.C., Jr. (2015). Diastolic dysfunction. Circ. J. *79*, 470–477. https://doi.org/10.1253/circj.CJ-15-0064.

62. Thomas, L., Marwick, T.H., Popescu, B.A., Donal, E., and Badano, L.P. (2019). Left atrial structure and function, and left ventricular diastolic dysfunction: JACC state-of-the-art review. J. Am. Coll. Cardiol. *73*, 1961–1977. https://doi.org/10.1016/j.jacc.2019.01.059.

63. Kirchgesner, J., Beaugerie, L., Carrat, F., Andersen, N.N., Jess, T., Schwarzinger, M., Bouvier, A.M., Buisson, A., Carbonnel, F., and Cosnes, J. (2018). Increased risk of acute arterial events in young patients and severely active IBD: a nationwide French cohort study ibd. Gut *67*, 1261–1268. https://doi.org/10.1136/gutjnl-2017-314015.

64. Moorlag, S.J.C.F.M., Khan, N., Novakovic, B., Kaufmann, E., Jansen, T., Van Crevel, R., Divangahi, M., and Netea, M.G. (2020). β-glucan induces protective trained immunity against *Mycobacterium tuberculosis* infection: a key role for IL-1. Cell Rep. *31*, 107634. https://doi.org/10.1016/j.celrep.2020.107634.

65. Mitroulis, I., Ruppova, K., Wang, B., Chen, L.S., Grzybek, M., Grinenko, T., Eugster, A., Troullinaki, M., Palladini, A., Kourtzelis, I., et al. (2018). Modulation of myelopoiesis progenitors is an integral component of trained immunity. Cell *172*, 147–161.e12. https://doi.org/10.1016/j.cell.2017.11.034.

66. Georgakis, M.K., Bernhagen, J., Heitman, L.H., Weber, C., and Dichgans, M. (2022). Targeting the CCL2–CCR2 axis for atheroprotection. Eur. Heart J. *43*, 1799–1808. https://doi.org/10.1093/eurheartj/ehac094.

67. Stuart, T., Butler, A., Hoffman, P., Hafemeister, C., Papalexi, E., Mauck, W.M., Hao, Y., Stoeckius, M., Smibert, P., and Satija, R. (2019). Comprehensive integration of single-cell data. Cell *177*, 1888–1902.e21. https://doi.org/10.1016/j.cell.2019.05.031.

68. Stuart, T., Srivastava, A., Madad, S., Lareau, C.A., and Satija, R. (2021). Single-cell chromatin state analysis with Signac. Nat. Methods *18*, 1333–1341. https://doi.org/10.1038/s41592-021-01282-5.

69. Cao, J., Spielmann, M., Qiu, X., Huang, X., Ibrahim, D.M., Hill, A.J., Zhang, F., Mundlos, S., Christiansen, L., Steemers, F.J., et al. (2019). The single-cell transcriptional landscape of mammalian organogenesis. Nature *566*, 496–502. https://doi.org/10.1038/s41586-019-0969-x.

70. Granja, J.M., Corces, M.R., Pierce, S.E., Bagdatli, S.T., Choudhry, H., Chang, H.Y., and Greenleaf, W.J. (2021). ArchR is a scalable software package for integrative single-cell chromatin accessibility analysis. Nat. Genet. *53*, 403–411. https://doi.org/10.1038/s41588-021-00790-6.

71. Lange, M., Bergen, V., Klein, M., Setty, M., Reuter, B., Bakhti, M., Lickert, H., Ansari, M., Schniering, J., Schiller, H.B., et al. (2022). CellRank for directed single-cell fate mapping. Nat. Methods *19*, 159–170. https://doi.org/10.1038/s41592-021-01346-6.

72. Jin, S., Guerrero-Juarez, C.F., Zhang, L., Chang, I., Ramos, R., Kuan, C.-H., Myung, P., Plikus, M.V., and Nie, Q. (2021). Inference and analysis of cell-cell communication using CellChat. Nat. Commun. *12*, 1088. https://doi.org/10.1038/s41467-021-21246-9.

73. Machlab, D., Burger, L., Soneson, C., Rijli, F.M., Schübeler, D., and Stadler, M.B. (2022). monaLisa: an R/Bioconductor package for identifying regulatory motifs. Bioinformatics *38*, 2624–2625. https://doi.org/10.1093/bioinformatics/btac102.

74. Lun, A.T.L., and Smyth, G.K. (2016). csaw: a Bioconductor package for differential binding analysis of ChIP-seq data using sliding windows. Nucleic Acids Res. *44*, e45. https://doi.org/10.1093/nar/gkv1191.

75. Andrews, S. (2010). FastQC: a Quality Control Tool for High Throughput Sequence Data (Babraham Bioinformatics).

76. Dobin, A., Davis, C.A., Schlesinger, F., Drenkow, J., Zaleski, C., Jha, S., Batut, P., Chaisson, M., and Gingeras, T.R. (2013). STAR: ultrafast universal RNA-seq aligner. Bioinformatics *29*, 15–21. https://doi.org/10.1093/bioinformatics/bts635.

77. Martin, M. (2011). Cutadapt removes adapter sequences from high-throughput sequencing reads. EMBnet. j. *17*. https://doi.org/10.14806/ej.17.1.200.

78. Liao, Y., Smyth, G.K., and Shi, W. (2014). featureCounts: an efficient general purpose program for assigning sequence reads to genomic features. Bioinformatics *30*, 923–930. https://doi.org/10.1093/bioinformatics/btt656.

79. Love, M.I., Huber, W., and Anders, S. (2014). Moderated estimation of fold change and dispersion for RNA-seq data with DESeq2. Genome Biol. *15*, 550. https://doi.org/10.1186/s13059-014-0550-8.

80. Ge, S.X., Jung, D., and Yao, R. (2020). ShinyGO: a graphical gene-set enrichment tool for animals and plants. Bioinformatics *36*, 2628–2629. https://doi.org/10.1093/bioinformatics/btz931.

81. Raudvere, U., Kolberg, L., Kuzmin, I., Arak, T., Adler, P., Peterson, H., and Vilo, J. (2019). g:profiler: a web server for functional enrichment analysis and conversions of gene lists (2019 update). Nucleic Acids Res. *47*, W191–W198. https://doi.org/10.1093/nar/gkz369.

82. Nagueh, S.F., Smiseth, O.A., Appleton, C.P., Byrd, B.F., Dokainish, H., Edvardsen, T., Flachskampf, F.A., Gillebert, T.C., Klein, A.L., Lancellotti, P., et al. (2016). Recommendations for the evaluation of left ventricular diastolic function by echocardiography: an update from the American Society of Echocardiography and the European Association of Cardiovascular Imaging. Eur. Heart J. Cardiovasc. Imaging *17*, 1321–1360. https://doi.org/10.1093/ehjci/jew082.

83. Llovera, G., Roth, S., Plesnila, N., Veltkamp, R., and Liesz, A. (2014). Modeling stroke in mice: permanent coagulation of the distal middle cerebral artery. J. Vis. Exp., e51729. https://doi.org/10.3791/51729.

84. Tomsits, P., Volz, L., Xia, R., Chivukula, A., Schüttler, D., and Clauß, S. (2023). Medetomidine/midazolam/fentanyl narcosis alters cardiac autonomic tone leading to conduction disorders and arrhythmias in mice. Lab Anim. (NY) *52*, 85–92. https://doi.org/10.1038/s41684-023-01141-0.

85. Tomsits, P., Sharma Chivukula, A., Raj Chataut, K., Simahendra, A., Weckbach, L.T., Brunner, S., and Clauss, S. (2022). Real-time electrocardiogram monitoring during treadmill training in mice. J. Vis. Exp. https://doi.org/10.3791/63873.

86. Tomsits, P., Chataut, K.R., Chivukula, A.S., Mo, L., Xia, R., Schüttler, D., and Clauss, S. (2021). Analyzing long-term electrocardiography recordings to detect arrhythmias in mice. J. Vis. Exp. https://doi.org/10.3791/62386.

87. Ramírez, F., Ryan, D.P., Grüning, B., Bhardwaj, V., Kilpert, F., Richter, A.S., Heyne, S., Dündar, F., and Manke, T. (2016). deepTools2: a next generation web server for deep-sequencing data analysis. Nucleic Acids Res. *44*, W160–W165. https://doi.org/10.1093/nar/gkw257.

88. Skene, P.J., Henikoff, J.G., and Henikoff, S. (2018). Targeted in situ genome-wide profiling with high efficiency for low cell numbers. Nat. Protoc. *13*, 1006–1019. https://doi.org/10.1038/nprot.2018.015.

89. Kaya-Okur, H.S., Janssens, D.H., Henikoff, J.G., Ahmad, K., and Henikoff, S. (2020). Efficient low-cost chromatin profiling with CUT&Tag. Nat. Protoc. *15*, 3264–3283. https://doi.org/10.1038/s41596-020-0373-x.

90. Yu, F., Sankaran, V.G., and Yuan, G.-C. (2021). CUT&RUNTools 2.0: a pipeline for single-cell and bulk-level CUT&RUN and CUT&Tag data analysis. Bioinformatics *38*, 252–254. https://doi.org/10.1093/bioinformatics/btab507.

91. Stempor, P., and Ahringer, J. (2016). SeqPlots - Interactive software for exploratory data analyses, pattern discovery and visualization in genomics. Wellcome Open Res. *1*, 14. https://doi.org/10.12688/wellcomeopenres.10004.1.

STAR★METHODS

KEY RESOURCES TABLE

REAGENT or RESOURCE	SOURCE	IDENTIFIER
Antibodies		
Anti-mouse CD45 (30-F11), Fluor™ 450	eBioscience	Cat# 48-0451-82; RRID: AB_1518806
Anti-mouse CD16/CD32 (2.4G2), BV480	BD Biosciences	Cat# 746324; RRID: AB_2743648
Anti-mouse CD11b (M1/70), FITC	BioLegend	Cat# 557396; RRID: AB_396679
Anti-mouse Ly6C (HK1.4), Brilliant Violet 570™	BioLegend	Cat# 128029; RRID: AB_10896061
Anti-mouse Ly6G (1A8-Ly6g), PE-eFluor™ 610	ThermoFisher Scientific	Cat# 61-9668-82; RRID: AB_2574679
Anti-mouse Sca1 (D7), Brilliant Violet 421™	BioLegend	Cat# 108127; RRID: AB_10898327
Anti-mouse CD115 (AFS98), BV711	BD Biosciences	Cat# 750890; RRID: AB_2874986
Anti-mouse CD150 (TC15-12F12.2), PE	BioLegend	Cat# 115903; RRID: AB_313682
Anti-mouse *ckit* (CD117) (2B8), PE-Cy™7	BD Biosciences	Cat# 558163; RRID: AB_647250
Anti-mouse CD135 (A2F10), APC	BioLegend	Cat# 135309; RRID: AB_1953264
Anti-mouse CD11c (N418), Brilliant Violet 650™	BioLegend	Cat# 117339; RRID: AB_2562414
Anti-mouse CD127 (A7R34), Brilliant Violet 785™	BioLegend	Cat# 135037; RRID: AB_2565269
Anti-mouse CD48 (HM48-1), PerCP	Elabscience	Cat# E-AB-F1017UF; RRID: AB_3106916
Anti-mouse CD34 (RAM34), Alexa Fluor® 700	BD Biosciences	Cat# 560518; RRID: AB_1727471
Anti-mouse CD3 (17A2), APC-eFluor™ 780	eBioscience	Cat# 47-0032-80; RRID: AB_1272217
Anti-mouse CD4 (RM4-5), APC-eFluor™ 780	Invitrogen	Cat# 47-0042-82; RRID: AB_1272183
Anti-mouse CD8a (53-6.7), APC/Cyanine7	BioLegend	Cat# 100714; RRID: AB_312753
Anti-mouse CD19 (eBio1D3 (1D3)), APC-eFluor™ 780	Invitrogen	Cat# 47-0193-82; RRID: AB_10853189
Anti-mouse TER-119/Erythroid Cells (TER-119), APC-Cy™7	BD Biosciences	Cat# 560509; RRID: AB_1645230
Anti-mouse CD16/CD32(93)	Invitrogen	Cat# 14-0161-86; RRID: AB_467135
Anti-mouse CD11b (93), APC-Cyanine7	eBioscience	Cat# A15390; RRID: AB_2534404
Anti-mouse Ly6C (HK1.4), PerCP/Cyanine5.5	BioLegend	Cat# 128011; RRID: AB_1659242
Anti-mouse F4/80 (BM8), PE-Cyanine7	eBioscience	Cat # 25-4801-82; RRID: AB_469653
Anti-mouse CCR2 (SA203G11) (Brilliant Violet 785™)	BioLegend	Cat # 150621; RRID: AB_2721565
Anti-mouse MHC Class II (NIMR-4), PE	eBioscience	Cat # 12-5322-81; RRID: AB_465930
Anti-mouse CCR2 (SA203G11), APC	BioLegend	Cat # 150628; RRID: AB_2810415
Anti-mouse CD45 (30-F11), APC-Cy7	BioLegend	Cat # 103116; RRID: AB_312981
Anti-mouse CD11b (M1/70), BV510	BD Biosciences	Cat #562950; RRID: AB_2737913
Anti-mouse Collagen I	Invitrogen	Cat # PA5-95137; RRID: AB_2806942
Anti-mouse Collagen III	Abcam	Cat # ab184993; RRID: AB_2895112
Anti-mouse Elastin	ThermoFisher Scientific	Cat # BS-1756R; RRID: AB_10856940
Anti-Tyrosine Hydroxylase Antibody	Sigma-Aldrich	Cat # AB152; RRID: AB_390204
Anti-GFP Nanobody conjugated to Alexa Fluor® 488 (GFP-booster)	ChromoTek	Cat# gb2AF488; RRID: AB_2827573
Anti-mouse Hashtag 1 Antibody TotalSeq-B0301 (M1/42)	BioLegend	Cat# 155831; RRID: AB_2814067
Anti-mouse Hashtag 2 Antibody TotalSeq-B0302 (M1/42)	BioLegend	Cat# 155833; RRID: AB_2814068
Anti-mouse Hashtag 3 Antibody TotalSeq-B0303 (M1/42)	BioLegend	Cat# 155835; RRID: AB_2814069
Anti-mouse Hashtag 4 Antibody TotalSeq-B0304 (M1/42)	BioLegend	Cat# 155837; RRID: AB_2814070
Anti-mouse Hashtag 5 Antibody TotalSeq-A0305 (M1/42)	BioLegend	Cat# 155809; RRID: AB_2750036
Histone H3K27ac antibody (pAb)	Active Motif	Cat#39134; RRID: AB_2722569
Histone H3K4me1 antibody (pAb)	Active Motif	Cat#39297; RRID: AB_2615075
Histone H3K4me3 antibody (pAb)	ThermoFisher	Cat#PA5-27029; RRID: AB_2544505
Guinea Pig anti-Rabbit IgG (H+L) Antibody	NovusBio	Cat#NBP1-72763; RRID: AB_11024108
Anti-human CD14	NovusBio	Cat# NBP2-67630; RRID: AB_3106915
Anti-human CCR2	R&D systems	Cat# MAB150, RRID: AB_2247178

(*Continued on next page*)

Continued

REAGENT or RESOURCE	SOURCE	IDENTIFIER
Goat Anti-Rabbit (H+L) Crossed-adsorbed Secondary antibody	Abcam	Cat# 214880; RRID: AB_3106917
Alexa Flour 647 goat anti-rabbit secondary antibody	Invitrogen	Cat # A-21247; RRID: AB_141778
Anti-mouse/rat IL-1β (InVivoMAb)	BioXcell	Cat # BE0246; RRID: AB_2687727
Human/Mouse Lipoprotein Lipase/LPL Antibody	Bio-Techne	Cat # AF7197; RRID: AB_10972480
APOE Polyclonal Antibody	Invitrogen	Cat # PA5-78803; RRID: AB_2745919
Phospho-c-Jun (Ser73)	Cell signaling	Cat # 3270; RRID: AB_2129575
Monoclonal Anti-β-Tubulin antibody	Sigma-Aldrich	Cat # T4026; RRID: AB_477577
β-Actin (D6A8) Rabbit mAb	Cell signaling	Cat # 8457; RRID: AB_10950489
Critical commercial assays		
Picro-Sirius Red Stain Kit (Cardiac Muscle)	Abcam	Cat# ab245887
Pierce™ BCA Protein Assay Kit	ThermoFisher	Cat# 23227
Colloidal Blue Staining Kit	Invitrogen	Cat# LC6025
High-Capacity cDNA Reverse Transcription Kit	Applied Biosystems	Cat# 4368814
QuantiTect SYBR® Green PCR Kits	Qiagen	Cat# 204143
RNAscope® Multiplex Fluorescent Detection Kit v2	ACDbio	Cat# 323110
RNAscope® TSA Buffer Pack	ACDbio	Cat# 322810
TSA Plus Cyanine 3 (Cy3) detection Kit	PerkinElmer	Cat# NEL744001KT
TSA Plus Cyanine 5 (Cy5) detection kit	PerkinElmer	Cat# NEL745001KT
pro-MMP-9 Mouse ELISA Kit	ThermoFisher Scientific	Cat# EMMMP9
Mouse IL-1 beta ELISA Kit	Abcam	Cat# ab197742
Mouse IL-6 ELISA Kit	Abcam	Cat# ab100712
HMGB1 express ELISA	Tecan	Cat# 30164033
Urea Assay Kit	Abcam	Cat# ab83362
EasySep™ Mouse Monocyte Isolation Kit	StemCell	Cat #19761
Lineage Cell Depletion Kit, mouse	Miltenyi Biotec	Cat# 130-090-858
Dead Cell Removal kit	Miltenyi Biotec	Cat# 130-090-101
Chromium Next GEM Chip G Single Cell Kit	10x Genomics	Cat# 1000127
Chromium Next GEM Chip H Single Cell Kit	10x Genomics	Cat# 1000162
Chromium Next GEM Single Cell ATAC Kit v2	10x Genomics	Cat# 1000406
3' Feature Barcode Kit	10x Genomics	Cat# 1000262
Library Construction Kit	10x Genomics	Cat# 1000190
Single Index Kit T Set A	10x Genomics	Cat# 1000213
Single Index Kit N Set A	10x Genomics	Cat# 1000212
ATAC-Seq kit	Active Motif	Cat#53150
Click-iT™ EdU Alexa Fluor™ 647 Flow Cytometry Assay Kit	Invitrogen	Cat# C10419
Agilent High Sensitivity DNA kit	Agilent	Cat# 5067-4626
Stainless steel beads 5mm	Qiagen	Cat# 69989
Biological samples		
Human heart paraffin sections	NCBN (Japan)	(Please see details in STAR Methods section)
Human heart paraffin blocks	LMU (Munich)	(Please see details in STAR Methods section)
Chemicals, peptides, and recombinant proteins		
Recombinant Mouse IL-1 beta/IL-1F2 Protein	Bio-Techne	Cat# 401-ML-010/CF
Cenicriviroc	Biorbyt	Cat# orb402001
Kolliphor	Sigma Aldrich	Cat# 5135
Murine recombinant IL-1beta	R&D systems	Cat# 401-ML
5-ethynyl-2'-deoxyuridine (EdU)	Invitrogen	Cat# E10187
Tamoxifen	Sigma Aldrich	Cat# 85256
Poly(I:C) HMW	InvivoGen	Cat# tlrl-pic

(*Continued on next page*)

Continued

REAGENT or RESOURCE	SOURCE	IDENTIFIER
Miglyol 812	Caelo	Cat# 3274
Lipopolysaccharides from Escherichia coli O111:B4	Sigma Aldrich	Cat# L2630-10MG
Collagenase type XI	Sigma Aldrich	Cat# C7657
Collagenase type I	Sigma Aldrich	Cat# SCR103
Deoxyribonuclease I	Sigma Aldrich	Cat# 9003-98-9
Hyaluronidase	Sigma Aldrich	Cat# 37326-33-3
Histopaque®-1077	Sigma Aldrich	Cat# 10771
Zombie NIR	BioLegend	Cat# 423105
Propidium Iodide	eBiosciences	Cat# 00-6990-42
7-AAD (7-Aminoactinomycin D)	ThermoFisher Scientific	Cat# A1310
BD Horizon™ Brilliant Stain Buffer	BD Biosciences	Cat# 563794
Cell Staining Buffer	BioLegend	Cat# 420201
Fast Green FCF (0.1 %)	Morphisto	Cat# 16596
Eosin Y solution (1%)	Carl Roth	Cat# 17372-87-1
Mayer's hematoxylin solution	Sigma Aldrich	Cat# MHS32
Acetic acid	Carl Roth	Cat# 64-19-7
Ethanol	SAV Liquid	Cat# 64-17-5
Paraformaldehyde	Morphisto	Cat# 11762.00100
Agarose	VWR Chemicals	Cat# 9012-36-6
Goat serum	ThermoFisher Scientific	Cat# 16210064
Bovine Serum Albumin	Sigma Aldrich	Cat# 9048-46-8
DMEM, high glucose, GlutaMAX™ Supplement, pyruvate	Gibco	Cat# 31966021
Gentamicin	Gibco	Cat# 15750-045
Fetal Bovine Serum	Gibco	Cat# A5256701
pHrodo™ Red Zymosan BioParticles™ Conjugate for Phagocytosis	Invitrogen™	Cat# P35364
StemSpan™ SFEM	StemCell Technologies	Cat#09600
DAPI (4'-6-Diamidino-2-Phenylindole-dihydrochloride)	ThermoFisher Scientific	Cat# D3571
Recombinant Murine TPO	ThermoFisher	Cat#315-14
Recombinant Murine SCF	ThermoFisher	Cat#250-03
Priomicin	Invitrogen	Cat#ant-pm-05
Gelatin from cold water fish skin	Sigma Aldrich	Cat# 9000-70-8
Eukitt® Quick-hardening mounting medium	Sigma Aldrich	Cat# 25608-33-7
Protease and Phosphatase Inhibitors	ThermoFisher Scientific	Cat# A32959
RIPA lysis/extraction buffer	ThermoFisher Scientific	Cat# 89900
Zymogram Plus (Gelatin) gels 10%	Invitrogen	Cat# ZY00102BOX
Zymogram Renaturing Buffer (10X)	Invitrogen	Cat# LC2670
Zymogram Developing Buffer (10X)	Invitrogen	Cat# LC2671
Novex™ Tris-Glycin SD-Probenpuffer (2X)	Invitrogen	Cat# LC2676
RNAscope® Probe- Mm-Mmp9-C2	ACDbio	Cat# 315941-C2
RNAscope® Probe- Mm-Cx3cr1	ACDbio	Cat# 314221
RNAscope® Probe- Hs-MMP9	ACDbio	Cat# 311331
RNAscope® Probe- Hs-CD14	ACDbio	Cat# 418808-C2
RNAscope® Probe- Mm-Vimentin	ACDbio	Cat# 457961
RNAscope® Probe- Mm-Collagen I-C2	ACDbio	Cat# 537041-C2
RNAscope® Wash Buffer Reagents	ACDbio	Cat# 310091
RNAscope® Target Retrieval Reagents	ACDbio	Cat# 322000
Tween-20	BioRad	Cat# 1662404
Digitonin 5%	ThermoFisher Scientific	Cat# BN2006
Nuclei EZ Lysis Buffer	Sigma Aldrich	Cat# NUC-01
Dulbecco's Phosphate Buffered Saline	Sigma Aldrich	Cat# D8537-500ML

(*Continued on next page*)

Continued

REAGENT or RESOURCE	SOURCE	IDENTIFIER
Fetal calf serum (FBS)	GIBCO	Cat# 105000-064
BioMag® Plus Concanavalin A,	ThermoFisher Scentific	Cat#86057-3
CUTANA pAG-Tn5 for CUT&tag	EpiCypher	Cat#15-1017
NEBNext® High-Fidelity 2X PCR Master Mix	New England Biolabs	Cat#M0541S
AMPureXP Beads (Beckman Coulter, A63881)	Beckman Coulter	Cat#A63881
Buffer PKD	Qiagen	Cat# 1034963
Proteinase K	Qiagen	Cat# 19131
Dynabeads™ Oligo(dT)25	ThermoFisher Scientific	Cat# 61005
Recombinant RNase Inhibitor	Takara	Cat# 2313A
UltraPure™ SSPE, 20X	ThermoFisher Scientific	Cat#15591043
Experimental models: Organisms/strains		
Mouse: C57BL6/J	Charles River	Strain #: 000664
Mouse: eGFP (C57BL/6-Tg(CAG-EGFP)131Osb/LeySopJ)	JAX	Strain #: 006567
Mouse: Mx1Cre (B6.Cg-Tg(Mx1-cre)1Cgn/J)	JAX	Strain #: 003556
Mouse: $Myb^{fl/fl}$ (B6.129P2-Mybtm1Cgn/TbndJ)	JAX	Strain #: 028881
Mouse: Ccr2tm1(cre/ERT2,mKate2)Arte	Becher lab, University of Zurich, Switzerland	MGI: 6314378
Mouse: KikGR (Tg(CAG-KikGR)33Hadj)	JAX	Strain #: 013753
Mouse: Ai14 (B6.Cg-Gt(ROSA)26Sortm14(CAG-tdTomato)Hze/J)	JAX	Strain #: 007914
Mouse: Ms4a3(creERT2)	This paper	N/A
Oligonucleotides		
Mmp9: Forward 5' GCT CCT GGC TCT CCT GGC TT 3' Reverse 5' GTC CCA CCT GAG GCC TTT GA 3'	Metabion	N/A
Ppia: Forward 5' ACA CGC CAT AAT GGC ACT GG 3' Reverse 5' ATT TGC CAT GGA CAA GAT GC 3'	Metabion	N/A
Software and algorithms		
FlowJo v.10.6	Treestar Inc.	N/A
GraphPad Prism 9	Graphpad Inc.	N/A
Image J 1.53c	NIH	N/A
ZEN	ZEISS	N/A
LAS X Office	Leica	N/A
Vevo LAB 5.5.0	FUJIFILM Visual Sonics	N/A
Ponemah software v.6.42	Harvard Bioscience Inc.	N/A
LabChart Pro software v.8	AD Instruments	N/A
Cell Ranger v.7.1.0	10x Genomics	N/A
Cell Ranger ATAC v.2.1.0	10x Genomics	N/A
R package Seurat 4.2.0	Stuart et al.[67]	N/A
R package Signac 1.9.0	Stuart et al.[68]	N/A
Monocle3 v.1.3.1	Cao et al.[69]	N/A
R package ArchR v.1.0.1	Granja et al.[70]	N/A
CellRank	Lange et al.[71]	N/A
R package CellChat	Jin et al.[72]	N/A
R package MonaLisa	Machlab et al.[73]	N/A
R package csaw	Lun and Smyth[74]	N/A
FastQC	Andrews[75]	N/A
STAR	Dobin et al.[76]	N/A
Cutadapt	Martin[77]	N/A
featureCounts	Liao et al.[78]	N/A
DESeq2	Love et al.[79]	N/A

(*Continued on next page*)

Continued

REAGENT or RESOURCE	SOURCE	IDENTIFIER
Ingenuity Pathway Analysis	QIAGEN	N/A
ShinyGO	Ge et al.[80]	N/A
g:Profiler	Raudvere et al.[81]	N/A
Deposited data		
Raw single cell mRNAseq data	This paper	GSE232098, GSE262599, GSE262727, GSE263035
Raw single nuclei ATACseq data	This paper	GSE230692
Raw bulk mRNAseq data	This paper	GSE232550
Raw bulk ATACseq data	This paper	GSE264093
CUT&tag seq data	This paper	GSE264418
Others		
Silicone rubber-coated monofilament	Doccol	Cat# 602223PK10Re
Telemetry transmitters (PhysioITel ETA-F10)	Harvard Bioscience Inc.	Cat# ETA-F10
Octapolar catheter	Millar Instruments	Cat# EPR-800
ALZET micro-osmotic pumps	Alzet	Cat#1007D

RESOURCE AVAILABILITY

Lead contact

Further information and requests for resources and reagents should be directed to and will be fulfilled by the lead contact, Arthur Liesz (arthur.liesz@med.uni-muenchen.de).

Materials availability

This study did not generate new unique reagents.

Data and code availability

Single-cell RNA-seq and single-nuclei ATAC-seq data have been deposited at GEO and are publicly available as of the date of publication. Accession numbers are also listed in the key resources table. This paper does not report original code. The used scripts for bioinformatic analyses of sequencing data are available at Mendeley Data (https://doi.org/10.17632/xygfn6kbgb.1) and at https://github.com/Lieszlab. Any additional information required to reanalyze the data reported in this paper is available from the lead contact upon request.

EXPERIMENTAL MODEL AND STUDY PARTICIPANTS DETAILS

Clinical patient population

Clinical data from three stroke patients recruited within the Stroke Induced Cardiac FAILure study (SICFAIL) consortium that were followed-up by cardiac echocardiography at three and 6 months after the incident stroke event was obtained. Methods off the SICFAIL study have been published elsewhere.[60] Patients underwent transthoracic echocardiography as part of the clinical routine by expert sonographers of the Comprehensive Heart Failure Centre Würzburg of the University Hospital Würzburg using standardized protocols. Pulsed-wave tissue Doppler imaging was obtained at the septal and lateral mitral annulus in the apical four-chamber view. The E/e' ratio was calculated averaging the lateral and septal e' velocities.[82] Worsening of diastolic function was defined as an increase in the E/e' ratio of at least 5 points. This study complied with the Declaration of Helsinki and was approved by the Ethics Committee of the Medical Faculty of the University of Würzburg (176/13). Demographical and clinical characteristics of the three patients are shown below.

	Patient 1	Patient 2	Patient 3
Age range, *years*	70-80	70-80	60-70
Sex	Male	Male	Male
Baseline NIHSS	9	0	4
HS-CRP	N/A	0.26	0.17
NT-proBNP	N/A	908	270

Human postmortem material was obtained from the National Center Biobank Network (NCBN) from Japan and the Institute of Legal Medicine, LMU University from Munich. Ethical approval for the use of human postmortem material was granted according to institutional ethics board protocol and national regulations. Detailed demographics and clinical characteristics of the patients are found in Table S3.

	Stroke (n=13)	Control (n=6)
Age, *years*	79 (12)	80 (29.3)
Sex (male), *n (%)*	76% (10)	33% (2)
Baseline NIHSS	23 (12)	N/A
Time from stroke to death, *days*	44 (48.5)	N/A

Shown as Median (Interquartile range, IQR), unless indicated

Animal experiments

All animal procedures were performed in accordance with the guidelines for the use of experimental animals and were approved by the respective governmental committees (Regierungspraesidium Oberbayern, the Rhineland Palatinate Landesuntersuchungsamt Koblenz). Wild-type C57BL6/J mice were purchased from Charles River. eGFP reporter mice (C57BL/6-Tg (CAG-EGFP)131Osb/LeySopJ), KikGR reporter mice (Tg(CAG-KikGR)33Hadj) and Ai14 reporter mice (B6.Cg-Gt(ROSA)26Sortm14(CAG-tdTomato)Hze/J) were purchased from the Jackson Laboratory (US), and bred and housed at the animal core facility of the Center for Stroke and Dementia Research (Munich, Germany). The Mx1-Cre mice (B6.Cg-Tg(Mx1-cre)1Cgn/J) and the $Myb^{fl/fl}$ floxed mutant mice (B6.129P2-Mybtm1Cgn/TbndJ) were purchased from Jackson Laboratory (US). $Ccr2^{CreERT2}$-TdT (Ccr2tm1(cre/ERT2,mKate2)Arte) mice were kindly provided by the Becher lab at University of Zurich (Switzerland), and were housed at the animal core facility of the Walter-Brendel-Center for Experimental Medicine (Munich, Germany) and crossbred to Rosa26tdTomato reporter mice. $Ms4a3^{creERT2}$ mice (B6J-Ms4a3em1(CreERT2)-Gt(ROSA)26Sortm14(CAG-tdTomato)) were generated at the animal core facility of the Center for Stroke and Dementia Research (Munich, Germany), by CRISPR-Cas9-mediated insertion of an IRES-CreERT2 cassette into the 3' un-translated region (3'UTR) of the *Ms4a3* gene in C57BL/6 zygotes. Genotyping was done by PCR using the following primers: Ms4a3 forward primer 5'- GACATTGCAGACGGGATGTAT-3'; Ms4a3 reverse primer 5'- ATCCATGGAGGTGTCATAGACCA-3'; CreERT2 forward primer 5'-AACACCCCGTGAAACTGCTC-3'.

Wild-type male mice and transgenic mice of both sexes (aged 8-12 weeks) were used for the experiments. All mice had free access to food and water at a 12 h dark-light cycle. Data were excluded from all mice that died during surgery. Animals were randomly assigned to treatment groups and all analyses were performed by investigators blinded to group allocation. All animal experiments were performed and reported in accordance with the ARRIVE guidelines.[11]

METHOD DETAILS

Transient proximal cerebral artery occlusion model

Transient intraluminal occlusion of the middle cerebral artery (MCA) was performed as previously described.[12] Briefly, mice were anaesthetized with isoflurane delivered in 100% O_2. A midline neck incision was made and the common carotid artery and left external carotid artery were isolated and ligated; a 2-mm silicon-coated filament was introduced via a small incision in the external carotid artery and advanced towards the internal carotid artery, therefore occluding the MCA. MCA was occluded for 5 min for a transient ischemic attack (TIA) model or for 60 min for tbe transient MCAo stroke model. After occlusion, the animals were re-anesthetized, and the filament was removed. MCA occlusion and reperfusion were confirmed by the corresponding decrease or increase in the blood flow, respectively, measured by a laser Doppler probe affixed to the skull above the MCA territory (decrease in the laser Doppler flow signal >80% of baseline value and increase in the laser Doppler flow signal>80% of baseline value before reperfusion). After recovery, the mice were kept in their home cage with facilitated access to water and food. Body temperature was maintained at 37°C throughout surgery using a feedback-controlled heating pad. The overall mortality rate of stroke mice was approximately 30 %. Exclusion criteria: 1. Insufficient MCA occlusion (a reduction in blood flow to >20% of the baseline value); 2. Insufficient MCA reperfusion (an increase in blood flow of >80% of the baseline value before removing the filament); 3. Death during the surgery.

Permanent distal cerebral artery occlusion model

Permanent occlusion of the distal MCA was performed as previously described.[83] Briefly, mice were anaesthetized with isoflurane delivered in 100% O_2 and placed in lateral position. After a skin incision between eye and ear, the temporal muscle was removed and the MCA identified. Then, a burr hole was drilled over the MCA and the dura mater was removed. The MCA was permanently occluded using bipolar electrocoagulation forceps. Permanent occlusion of the MCA was visually verified before suturing the wound. After recovery, the mice were kept in their home cage with facilitated access to water and food. Body temperature was maintained at 37°C throughout surgery using a feedback-controlled heating pad. Exclusion criteria: Artery broken during surgery and/or major bleeding artery and remaining blood between the brain and skull.

Drug administrations

5-ethynyl-2'-deoxyuridine

Mice received one i.p. injection of EdU dissolved in 0.9% Sodium Chloride 4 h prior to euthanasia, at a dose of 5 mg kg^{-1} body weight, in a final volume of 250 μl. For continuous and controlled EdU delivery, osmotic pumps (ALZET) containing 100 μl of EdU at a concentration of 10 mg/ml were implanted i.p. into mice for 1 week.

Anti-IL-1β

Mice received two i.p. injections of antagonizing anti-IL-1β or vehicle (0.9% NaCl) 1 h prior to and 1 h after surgery, at a dose of 4 mg kg^{-1} body weight, in a final volume of 200 μl.

Recombinant IL-1β

Mice received one i.p. injection of recombinant IL-1β or vehicle (0.9% NaCl), at a dose of 40μg kg^{-1} body weight, in a final volume of 100μl.

Lipopolysaccharides

Mice received one i.p. injection of LPS or vehicle (0.9% NaCl), at a dose of 300μg kg^{-1} body weight, in a final volume of 100μl.

CCR2/CCR5 antagonist Cenicriviroc

Mice received daily i.p. injections of CVC or vehicle (30% Kolliphor and 70% 0.9% NaCl) at a dose of 20 mg kg^{-1} body weight, in a final volume of 250 μl.[13] First dose was given after stroke induction and then daily for 28 days.

Tamoxifen

Tamoxifen was prepared by dissolving in Miglyol 812 for a final concentration of 20 mg/mL and stored at 4 °C. Mice received daily i.p. injections of Tamoxifen solution at a dose of 120 mg kg^{-1} body weight, in a final volume of 150 μl, for 7 consecutive days.

Echocardiography

All mice underwent transthoracic echocardiography using a high-frequency ultrasound system with a 40-MHz linear transducer (Vevo 3100LT, Visual Sonics, Canada). In brief, mice were anaesthetized with isoflurane (in 100% O_2 at 4% induction for 1 min and 1.5% for maintenance) and placed in supine position on a heated platform (37°C). Heart rate was monitored along the recording period. After applying ultrasonic gel, the heart was visualized and a 2D M-mode video (4.5 seconds) was recorded from the parasternal short-axis view. To estimate the mitral valve inflow pattern, the transmitral LV outflow was also recorded from the apical four chamber view using the pulse wave (PW)-doppler imaging mode. All data was analyzed in Vevo 3100 Software, as previously described and according to the American Society of Echocardiography recommendations.[14] The investigators performing and reading the echocardiograms were blinded to the treatment allocation.

ECG telemetry

Continuous electrocardiogram (ECG) acquisition was done over a period of 3 weeks by implanting telemetry transmitters (PhysiolTel ETA-F10, Data Science International, DSI) in male C57Bl/6J wildtype mice (n=4/group) as previously described.[84,85] Briefly, anesthetized mice were placed in a supine position on a heated platform (37°C). A 1.5-2 cm ventral midline abdominal incision was performed, and a subcutaneous pocket in the upper right chest and left abdomen below the heart was prepared for placing the electrode leads. The transmitter body was gently placed in the peritoneum above the intestine. Using a 14-gauge needle, the electrical leads were tunneled through the peritoneum and subcutaneously positioned in the prepared pockets leading to an Einthoven II configuration. The tips of the leads were fixed to the pectoral muscle using a 7-0 suture, and the abdominal fascia and skin were closed.

Data analysis was done using Ponemah's ECG Pro module (Ponemah software 6.42 version).[85,86] 24-hour ECG traces on day 3, 7, 14 and 21 post transmitter implantations were subdivided into 12-hour traces to allow a separate analysis of the ECG during day and night time. P, Q, R, S, T marks were automatically annotated by the software. Undetected marks were manually added. 20 consecutive ECG beats were averaged in each 12-hour day and night window to obtain the heart rate (BPM), P wave duration (ms), PR interval (ms), QRS duration (ms), QT interval (ms). QTc was calculated using Bazett's formula.

Cardiac electrophysiology studies

EP studies were performed 4w post-stroke or naive male C57Bl/6J mice (n=5-7/group) to assess the atrial, av nodal, and ventricular conduction properties, as well as arrhythmia inducibility. An amplifier (AD Instruments), Powerlab (AD Instruments), stimulator (ISO-Stim-01D, npi), and LabChart Pro software (version 8.0, AD Instruments) was used for signal recording and processing as well as intracardiac stimulation. Mice were anesthetized with isoflurane (2.5-4% in 100% oxygen at 1L/min. flow rate) and subsequently maintained at 1.5-2% during EP studies. Mice were positioned in a supine position on a heated platform (37°C) monitored with a rectal temperature probe (Kent Scientific). For surface ECG recording, needle electrodes were placed subcutaneously with the negative lead in the right forelimb, the positive electrode in the left hindlimb, and the ground lead in the right hindlimb allowing an Einthoven I configuration. A midline incision was made along the sternocleidomastoid muscle to visualize and expose the right jugular vein. Two 4-0 sutures were placed at the proximal and distal end of the vein. The suture at the proximal end was tightened and clamped to straighten the vein. The distal suture was used to hold the catheter in place upon insertion into the heart. A small cut was made in the longitudinal direction of the vein using precision scissors before a 1.1 F octapolar catheter (Millar Instruments)

was placed in the vein, followed by gradual advancement into the heart until the tip was located in the RV apex. The correct position of the catheter was confirmed by the local electrograms.

Programmed electrical stimulation was performed following a standard protocol with 120 ms and 100 ms pacing cycle lengths as previously described. In brief, the Wenckebach cycle length was determined by progressively faster atrial pacing rates and the retrograde (VA) conduction cycle length was measured by progressively slower ventricular pacing rates to assess conduction properties of the AV node. Refractory periods in the atrium, the AV node and the ventricle were determined using the standardized S1/S2 protocol. Inducibility of arrhythmias was assessed by applying the standardized S1S2S3 protocol with basic cycle lengths of 120ms and 100 ms and S2/S3 stimulation at cycle lengths of 40-10 ms in 5 ms decrements. Furthermore, burst pacing with application of two 3 second and 6 second bursts at rates of 40–10 ms in 5 ms decrements was performed. An atrial arrhythmia was defined as high frequent atrial signal with regular/irregular AV conduction or a clear change in atrial basic cycle length post stimulation with morphologic change of the atrial signal indicating ectopic origin, either of them lasting for $\geq$1 second.

Non-invasive blood pressure measurements

Mouse blood pressure was evaluated by tail-cuff transmission photoplethysmography using BP-2000 Blood Pressure Analysis System (Visitech Systems, USA). In brief, mice were placed in a holder device with its tail passing through a cuff with an optical sensor. The standard test session was run for 20 times and systolic, diastolic blood pressure and heart rate were acquired.

BM transplantation

Donor animals (actin-eGFP^{+} or KikGR^{+}) were euthanized and femurs were collected in cold PBS. Bone marrows were isolated from femurs and filtered through 40 μm cell strainers to obtain single cell suspensions. Depletion of mature hematopoietic cells, including T cells, B cells, monocytes/macrophages, granulocytes, erythrocytes and their committed precursors was achieved using a negative selection kit for Lineage Cell Depletion (Miltenyi). After washing, cell number and viability was assessed using an automated cell counter (Countess 3, ThermoFisher Scientific) and Trypan Blue solution (Merck, Germany). Cells were injected i.v. into Mx1^{Cre}:c-Myb$^{fl/fl}$ recipient mice (3-8x10^{6} cells per mouse) in a total volume of 100 03BCl saline. At the time of transplantation, recipient mice had previously been treated with poly(I:C) solution (Invivogen) at a dose of 10 μg g^{-1} body weight every other day for five times to induce BM depletion.[15] Mice were maintained for 4 weeks after transplantation to establish efficient BM repopulation.

Organ and tissue collection

Mice were terminally anesthetized with ketamine (120mg/kg) and xylazine (16mg/kg). In a subset of experiments, mice were injected i.v. with 3 μg CD45-eFluor450 or CD45-APC-Cy7, 3 min before transcardiac perfusion, to exclude blood contamination in peripheral organs. Blood was drawn via cardiac puncture and collected in 50mM EDTA tubes (Sigma-Aldrich). Plasma was isolated by centrifugation at 3000g for 10 min and stored at -80°C until further use. Immediately after cardiac puncture, mice were transcardially perfused with 0.9% NaCl and the heart, both lungs, the right liver lobe, the spleen and both femurs and tibias were carefully excised and processed according to the specific endpoint.

Cell isolation

Spleen and bone marrow (from femur) were homogenized and filtered through 40 μm cell strainers to obtain single cell suspensions. Heart, lung and liver tissues were thoroughly minced in a digestive solution containing 60U/ml DNAse, 450U/ml Collagenase I, 125 U/ml Collagenase XI and 60 U/ml Hyaluronidase I-S in PBS and incubated for 30 min at 37°C on a shaker at 250 rpm. Afterwards, samples were filtered through a 40 μm cell strainer to obtain final single cell suspensions.

Cell sorting

Cell suspensions were obtained as described above and further purified by a density gradient centrifugation with Histopaque-107 at 300g, 4°C for 20 min. The mononuclear layer was isolated and cells were washed twice with PBS. Cell suspensions were stained with surface markers diluted in Brilliant Stain Buffer and sorted using a FACS Aria II cell sorter (BD Biosciences, Inc.) or a SH800S Cell Sorter (Sony Biotechnology). Propidium iodide (PI) or 4′,6-diamidino-2-phenylindole (DAPI) were used as a cell viability marker.

Flow cytometry

The primary conjugated anti-mouse antibodies listed above were used for surface marker staining of different leukocytes subpopulations (see key resources table). For high-dimensional flow cytometry of the heart, mice were injected i.v. with 3 μg CD45-e450 (see antibody list) 3 min before transcardiac perfusion, to exclude blood contamination. All samples were stained with Zombie NIR Fixable Viability Kit (1:1000) for 10 min at 4°C and then with the specific surface markers diluted in Brilliant Stain Buffer, according to the manufacturer's protocols, for 30 min at 4°C. For the Click-iT EdU flow cytometry cell proliferation assay, prior to surface antibody staining, cell suspensions were fixed, permeabilized and the intracellular EdU was labelled by means of a click chemical reaction, following manufacturer's instructions. All flow cytometric data was acquired using a Cytek Northern lights™ flow cytometer (Cytek Biosciences, US) and analyzed using FlowJo software.

Single-cell RNA sequencing

Six mouse single-cell RNA experiments were performed in this study: two on myeloid cells isolated from peripheral organs, including the heart, lung, liver, spleen and/or blood; one on cardiac interstitial cells, and the other three on bone marrow myeloid cells, either from stroke and control mice, or from naïve recipients after BM transplantation. For the first experiments, mononuclear cell suspensions from peripheral organs were incubated with anti-CD16/CD32 antibody to block nonspecific binding and stained for $CD45^+CD11b^+$ myeloid cells (see antibodies list). Unique cell hashtags antibodies were also used to label cells from each organ individually. All surface antibodies and hashtag antibodies were incubated for 30 min at 4°C. Immediately prior to cell sorting, PI was added to all samples to label dead cells. Cells were sorted according to their surface markers (SH800S Cell Sorter, Sony Biotechnology or FACS Aria II Fusion cell sorter, BD Biosciences, Inc.). Sorted and organ-specific labeled cells from the same animal were pooled together in the same collecting tube (for peripheral organs, a cell ratio of 1:4:4:4:4 for the heart, lung, liver, spleen and blood was maintained; for heart and blood from BMT mice, the cell ratio was 2:1, respectively). After sorting, all cells were centrifuged and cautiously resuspended to a final concentration of 1000-1200 cells/μl. Cells were then transferred to the Next GEM chip according to manufacturer's instructions. ScRNA-seq and cell hashing libraries were prepared using the 10x Chromium Single Cell 3′ Solution combined with feature barcoding technology for Cell surface protein (cell hashing), as per established protocols.[15]

For analysis of cardiac interstitial cells, cell suspensions from the heart were obtained by means of an enzymatic digestion as previously described. Cell suspensions were then passed through a 40mm cell strainer to remove cardiomyocytes and incubated with pre-warmed red cell lysis buffer for 2 min to remove blood cells. Dead cell debris was removed with the Dead Cell Removal kit (Miltenyi) and single nucleated cells were incubated with DAPI for 5 min prior to sorting CD45(i.v. injected)-negative live cells on a FACS Aria II Fusion cell sorter (BD Biosciences, Inc.). After sorting, all cells were centrifuged and cautiously resuspended to a final concentration of 1000 cells/μl. Cells were then transferred to the Next GEM chip according to manufacturer's instructions. ScRNA-seq libraries were prepared using the 10x Chromium Single Cell 3′ Solution, as per established protocols.[16]

For the experiments on bone marrow samples, bone marrow cells suspensions were stained with a cocktail of antibodies against markers of the lymphoid lineage (CD3, CD4, CD8a, CD19 and Ter119) and mature neutrophils (Ly6G, see antibodies list). Immediately prior to cell sorting, PI or 7-AAD were also added to label dead cells. Cells were sorted according to the surface markers (SH800S Cell Sorter, Sony Biotechnology, or FACS Aria II Fusion cell sorter, BD Biosciences, Inc.) and the negative fraction of BM myeloid cells (depleted of lymphoid lineage cells and neutrophils) was collected. After sorting, cells were centrifuged and cautiously resuspended to a final concentration of 1000-1400 cells/μl. Cells were then further processed according to manufacturer's (10X) instructions. The scRNA-seq libraries were prepared using the 10x Chromium Single Cell 3′ Solution.

In all six experiments, quality control of all cDNA samples was performed with a Bioanalyzer 2100 (Agilent Technologies) and libraries were quantified with the Qubit dsDNA HS kit. Gene expression libraries were sequenced on an Illumina NextSeq 1000 or 2000 using 20,000 reads per cell. Cell-surface protein expression libraries were sequenced on an Illumina NextSeq 1000 or 2000 aiming for 5,000 reads per cell.

Single-cell RNA-seq data analysis

Cell Ranger software was used to demultiplex samples, process raw data, align reads to the mouse mm10 reference genome (or a custom mouse mm10 reference genome with the eGFP, kikGR or tdTomato marker genes incorporated) and summarize unique molecular identifier (UMI) counts. Filtered gene-barcode and hashing-barcode matrices that contained only barcodes with UMI counts that passed the threshold for cell detection were used for further analysis. Filtered UMI count matrices were processed using R and the R package Seurat. As quality control steps, the following cells were filtered out for further analysis: (1) doublets originating from two cells from different samples (one cell positive for two HTO); (2) cells with no HTO detected; (3) cells with a number of detected genes <500 or >6000; (4) cells with >7% of counts that belonged to mitochondrial genes. Hereafter, raw gene counts in high-quality singlets were log normalized and submitted to the identification of high variable genes by MeanVarPlot method. Data was scaled and regressed against the number of UMIs and mitochondrial RNA content per cell. Data was subjected to principal component analysis and unsupervised clustering by the Louvain clustering method. Cell clusters were visualized using Uniform Manifold Approximation and Projection (UMAP) representations. Clusters were manually annotated using the top upregulated genes for each cluster and through the UMAP visual inspection of the expression of key previously described markers. After initial cluster annotation, clusters of T and B cells (between 5-20% of total cells, depending on the experiment) were removed and all remaining myeloid cells were reanalyzed. Differentially expressed genes between conditions were calculated using the FindMarkers function. Volcano plots were generated using EnhancedVolcano in R (Bioconductor EnhancedVolcano v.1.6.0).[16] Pathway enrichment analysis was performed using Ingenuity Pathway Analysis (Qiagen) and ShinyGO.[80] Trajectory and pseudotime analysis were computed on the corresponding UMAP projections using Monocle 3.[18] The CellRank framework (v2.0.2) was used to identify potential genes and GO terms associated with the monocyte-macrophage differentiation trajectory.[71] In brief, for every single cell fate probabilities of reaching tissue-resident macrophages, as a differentiated terminal state, were calculated. These fate probabilities were correlated with gene expression to uncover putative trajectory driver genes. Gene expression was modelled by generalized additive models (n_knots=6). Cell-to-cell communication network analysis was performed using R toolkit CellChat.[72]

Single-nuclei ATAC-seq

Single nuclei suspensions were prepared as previously reported.[19] In brief, BM cell suspensions were obtained as described for the single-cell sequencing experiments. Live, lymphoid lineage (CD3, CD4, CD8a, CD19 and Ter119) and neutrophil (Ly6G) negative BM cells were sorted using a FACS Aria II Fusion cell sorter (BD Biosciences, Inc.). Cells were centrifuged and incubated twice with Nuclei EZ Lysis Buffer on ice for 5 min each time. Lysed cells were washed and nuclei were incubated with 7AAD at 1μg/ml for microscopic inspection of integrity before sorting on a FACS Aria II Fusion (BD Biosciences). Then, nuclei were further processed according to manufacturer's (10X) protocols at a concentration of 1000-5000 nuclei/μl. Single nuclei ATAC libraries were prepared using the 10x Chromium Next GEM Single Cell ATAC kit. Quality control of all cDNA samples was performed with a Bioanalyzer 2100 (Agilent Technologies). Libraries were sequenced on an Illumina NextSeq 1000, aiming for 25,000 reads per nuclei.

Single-nuclei ATAC-seq data analysis

Cell Ranger ATAC software (10x Genomics) was used to process raw single nuclei ATAC-seq data, align reads to the Mus musculus mm10 reference genome, generate the peak matrix with single-cell accessibility counts and the fragments file with unique fragments across all single cells. Filtered peak-barcode matrices that contained only barcodes with UMI counts that passed the threshold for cell detection were used for further analysis. Filtered matrices and fragment files were processed using R and the R packages Signac and Seurat. In brief, a chromatin accessibility matrix was created and as quality control steps, the following nuclei were filtered out for further analysis: (1) nuclei with a total detected fragments > 30,000 or < 5,000; (2) nuclei with the fraction of all fragments that fall within ATAC-seq peaks < 40%; (3) nuclei with a transcriptional start site (TSS) enrichment score lower than 2; and (4) nuclei with a ratio of mononucleosomal to nucleosome-free fragments higher than 4. Peaks were called using MACS2.[20] Hereafter, UMAP based on latent semantic indexing (LSI) was generated to visualize data in the two-dimensional space and a gene activity matrix was created to quantify the activity of each gene in the genome by assessing its chromatin accessibility associated with each gene. Next, to help interpret data, the integration pipeline (canonical correlation analysis) from the Seurat package was used to perform cross-modality integration and label transfer on the single-cell ATAC dataset and single-cell mRNA sequencing dataset also generated from BM myeloid cells. Shared correlation patterns in the gene activity matrix and the single-cell mRNA sequencing were used to identify matched biological states and annotate predicted cluster labels for all nuclei from the ATAC object. Only those nuclei with a predicted score above the 0.5 cutoff were retained and considered for further analyses. Volcano plots showing differential accessible peaks between conditions were generated using EnhancedVolcano in R (Bioconductor EnhancedVolcano v.1.6.0).[17] To identify differentially-active motifs between experimental conditions within specific cell types, we computed a per-cell motif activity score using chromVAR (adj p-value <0.05).[21] Motif position frequency matrices were obtained from the JASPAR database. For each gene, we used the ArchR package to identify set of peaks that regulate the gene by computing the correlation between gene expression and accessibility at nearby peaks. Peak-to-gene links were identified using default parameters, with k=100 and empirical p-value estimation. Positively correlated peak-to-gene links were defined with cutoffs r > 0.45 and FDR < 0.1. The corresponding peak-to-gene matrix was obtained by returning matrices from plotPeak2GeneHeatmap() function with k = 25, grouped by cluster identities. To further characterize these peak-to-gene links, the presence of putative transcription factor motifs was identified using the R package motifmatchr. Peaks were converted to GRanges and position weight matrices were obtained from JASPAR 2022 database.[22]

Bulk ATAC sequencing

Bone marrow (BM) cells were isolated from naïve mice as previously described above. Depletion of mature hematopoietic cells, including T cells, B cells, monocytes/macrophages, granulocytes, erythrocytes and their committed precursors was achieved using a negative selection kit for Lineage Cell Depletion (Miltenyi). Cells were then cultured for 24h at 37°C and 5% CO2 at a density of 2,5·105/mL in StemSpan™ SFEM medium supplemented with Priomicin (1:500), thrombopoietin (TPO) (100 ng/ml), and stem cell factor (SCF) (20 ng/ml) to maintain the stemness of the progenitors and prevent extensive differentiation. Then, cells were exposed to either Isotype or recombinant IL-1b at a concentration of 10 ng/ml overnight at 37°C. The next morning, cells were harvested, and ATAC-Seq kit libraries were prepared using the ATAC-Seq Kit from Active Motif, following the manufacturer's instructions. Libraries were pooled and sequenced on an Illumina NextSeq 1000. Bulk ATAC-seq data was aligned to the mouse genome and read filtering, peak calling and IDR based peak filtering was performed by implementing the ENCODE ATAC-seq pipeline.[87] The bigwig coverage track was generated using Deeptools (v3.1.3).[87] Differentially accessible peaks (3 groups: control, shared, IL-1β-treated) were identified using csaw.[74] Motif enrichment analysis was performed using monaLisa.[73]

CUT&tag sequencing

BM cell suspensions were obtained as described for the single-cell sequencing experiments. BM monocytes (CD11b+Ly6C+Ly6G-) and the lineage- (CD3, CD4, CD8a, CD19, Ter119) and Ly6G) negative myeloid fraction of BM (HSPC-enriched population) were sorted using a FACS Aria II cell sorter (BD Biosciences, Inc.). Cleavage Under Targets Tagmentation (CUT&Tag) assays for H3K27Ac, H3K4me1 and H3K4me3 were performed on these two cell populations as previously reported,[88,89] using the EpiCypher protocol with specific modifications. Briefly, nuclei were extracted from 1·105 cells, washed twice and incubated with 10 μL of activated concanavalin A beads (ThermoFisher) for 10 min at RT. The beads were then resuspended in cold antibody buffer containing primary antibodies (against H3K27ac, H3K4me1 or H3K4me3) and the mixture was incubated overnight at 4°C on a nutator. Then, the beads were washed twice and resuspended in secondary H+L antibody (NovusBio) diluted in 50 μL digitonin buffer,

followed by incubation for 30 min at RT on a rotator. Samples were then incubated with 2.5 μL CUTANA pAG-Tn5 (EpiCypher) for 1 h at RT on a nutator. DNA was tagmented for 1 h at 37°C using tagmentation buffer and tagmented chromatin fragments were released for 1 h at 58°C. 13 ul of tagged DNA was used to prepare the library using NEBNext® High-Fidelity 2X PCR Master Mix (NEB) with CUT&Tag specific PCR cycling parameters. DNA was purified using AMPureXP Beads (Beckman Coulter). The quality of the CUT&Tag libraries was assessed using the Agilent 2100 Bioanalyzer System (Agilent). Libraries were pooled together and sequenced on an Novaseq 6000 SP 300 flowcell using paired-end sequencing (2*150). CUT&Tag-seq data was mapped using CUT&RUNTools 2.0.[90] Differentially accessible peaks (3 groups - control, shared, stroke) were identified using csaw.[74] Motif enrichment analysis was performed using monaLisa.[73] The plotting of the Cut&tag signal at genomic features was performed using SeqPlots.[91]

Second harmonic generation microscopy imaging

Mice were deeply anesthetized and euthanized as described above. Hearts were immediately extracted and immersed in 4% paraformaldehyde overnight. Afterwards, hearts were embedded in 4% agarose, coronally sectioned to 100 μm thick sections and kept at 4°C as free-floating sections in PBS. Sections were then imaged using Zeiss LSM 7 MP microscopy (Zeiss, Germany), acquiring second harmonic generation signals (445 nm) after excitation at a wavelength of 895 nm. SHG images were quantitatively analyzed with ImageJ software as previously described.[23,24] In brief, the images underwent Fast Fourier Transformation (FFT) and then were submitted to an elliptic fit to obtain Aspect Ratio values as a measure of the anisotropy of the collagen fiber distribution.

Mouse heart histological sections

Mice were deeply anaesthetized and euthanized as described above. For conventional and immunofluorescence staining procedures, hearts were immediately extracted, submerged in 4% paraformaldehyde overnight at 4°C, embedded in paraffin and coronally sectioned to 5 μm thick sections. For RNA-fluorescence in situ hybridization (RNA-FISH), hearts were excised, directly flash-frozen on dry ice and coronally cryosectioned to 5μm thick sections.

Human heart histological sections

Cardiac tissue specimens were obtained from adult subjects with ischemic stroke and controls. Specimens were immersed in 10% formalin upon collection to preserve tissue integrity, embedded in paraffin and sectioned at 3 μm thick sections.

Picrosirius red staining

Mouse and human heart paraffin sections were deparaffinized, stepwise in xylene, 100% ethanol, 70% ethanol and 50% ethanol, and then stained with Fast Green solution for 20 min. The sections were washed with 30% acetic acid, rinsed in tap water and submerged to Picrosirius red Solution for 60 min. Hereafter, sections were washed with 30% acetic acid and absolute alcohol, dried at room temperature (RT) and mounted with Eukitt® Quick-hardening mounting medium. Images were acquired at 20x magnification using Axio Imager 2 (Zeiss, Germany).

Hematoxylin and eosin staining

Mouse and human heart paraffin sections were processed and deparaffinized as previously described. Sections were incubated with Mayer's hematoxylin solution at RT for 5 min and washed under running tap water for 10 min. Afterwards, sections were incubated with 1% Eosin Y solution at RT for 3 min and rinsed with distilled water. Finally, sections were dehydrated stepwise with 70% ethanol, 80% ethanol, 90% ethanol and 100% ethanol, dried at RT and mounted with Eukitt® Quick-hardening mounting medium. Images were acquired at 100x magnification using Axio Imager 2 (Zeiss, Germany).

Immunofluorescence staining

Mouse heart paraffin sections were processed and deparaffinized as previously described. After deparaffinization, sections were incubated with blocking solution containing 2% goat serum, 1% BSA and 0.1% cold fish skin gelatin in PBS for 1h at RT. Afterwards, sections were incubated with the primary antibodies against Collagen I (1:50), Collagen III (1:100), Fibronectin (1:50) or Tyrosine Hydroxylase (TH) (1:100) overnight at 4°C. Then, sections were washed in PBS and incubated with Alexa Flour 647 goat anti-rabbit secondary antibody (1:100) in the dark for 1h at RT. After washing, sections were stained with DAPI and mounted with Fluoromount™ Aqueous Mounting medium. Images were acquired in a confocal microscope at 20x or 40x magnification (LSM 880, LSM 980; Carl Zeiss, Germany)).

Immunohistochemical staining

Human heart paraffin sections were deparaffinized and submitted to antigen retrieval in sodium citrate buffer (pH 6) for 20 min at 90°C. Then, sections were washed and immersed in 3% hydrogen peroxide in methanol for 15 min. Sections were then incubated with blocking solution containing 5% goat serum, 1% BSA and 0.1% cold fish skin gelatin in PBS for 1 h at RT, and afterwards with the primary antibodies against CD14 (1:100) or CCR2 (1:100) overnight at 4°C. After washing, sections were incubated with HRP-conjugated goat anti-rabbit secondary antibody (1:1000) in the dark for 1 h at RT. Finally, sections were washed, stained with Mayer's hematoxylin for 5 min, dried and mounted with Fluoromount™ Aqueous Mounting medium. Images were acquired at 20x and 40x magnifications using Axio Imager 2 (Zeiss, Germany).

RNA-fluorescence *in situ* hybridization

The RNAscope Multiplex Fluorescent v2 was used on mouse flash-frozen and human paraffin sections, according to the manufacturer's instructions. Mouse flash-frozen sections were first fixed with 4% PFA at 4°C for 30 min and dehydrated stepwise in 50% ethanol, 70% ethanol and 100% ethanol. Then, sections were incubated with protease IV at RT for 30 min and hybridized with probes specific to *Mmp9, Collagen I, Vimentin* or C*x3cr1* at 40°C for 2 h. Human paraffin sections were deparaffinized by incubating with Xylene for 10 min and then 100% ethanol for 5 min. Then, sections were incubated with Hydrogen peroxide for 10 min at RT and antigen retrieval was done by incubating sections with RNAscope® Retrieval Reagents at 95°C for 15 min. Sections were then incubated with protease III at RT for 30 min and hybridized with probes specific to MMP9 and CD14 at 40°C for 2 h. After hybridization, all sections (mouse and humans) were washed and incubated with a series of pre-amplifier and amplifier reagents, fluorophores and the HRP blocker at 40°C for 15–30 min each, according to manufacturers' protocols. To detect the eGFP+ signal, specific mouse sections were further incubated with 0.5% Triton X-100 for 5 min, blocked with 4% BSA for 10 min at RT and incubated with 1:200 anti-GFP Nanobody conjugated to a fluorescent dye (GFP-booster) at 4°C overnight. Finally, all sections were then stained with DAPI and mounted with Fluoromount™ Aqueous Mounting medium. Images were acquired at 20x and 63x magnifications (Leica, Dmi8, Germany).

MMP9 gelatin zymography

Mice were deeply anaesthetized and euthanized as described above. Hearts were immediately extracted and flash-frozen on powdered dry ice. Frozen hearts were placed in microcentrifuge tubes containing RIPA lysis/extraction buffer already supplemented with protease/phosphatase inhibitor and 5mm steal beads, and placed on a tissue lyser (Qiagen, Germany) at 50HZ for 10 min. The total protein content of each sample was measured using the Pierce BCA protein assay kit. Same amounts of protein were loaded and fractioned on 10% Zymogram Plus (Gelatin) gels, according to the manufacturer's instructions. Gels were then incubated in Zymogram Renaturing Buffer and in Zymogram Developing Buffer for 30 min each, both at RT with gentle agitation. Then, gels were incubated in Zymogram Developing Buffer overnight at 37°C and stained with the colloidal blue staining kit for 3 hours at RT. Gels were washed in water overnight and imaged with a gel scanner (Epson, Germany). Images were analyzed with ImageJ.

Blood urea measurement

Plasma was collected from stroke and control mice one month post-stroke and frozen at -80°C until further use. Frozen plasma was thawed on ice and a commercial urea assay kit (Abcam, USA) was used for evaluating the concentration of the blood urea, according to manufacturer's instructions. All samples were run in duplicates and all duplicates showed a coefficient of variation <15%.

Enzyme linked immunosorbent assay

Total pro-MMP9 concentrations were measured in heart protein lysates using the pro-MMP9 Mouse ELISA kit, according to manufacturer's (ThermoFisher) instructions. Pro-MMP9 concentrations are expressed per microgram of total protein content in the heart, measured using the Pierce BCA protein assay kit and following manufacturer's instructions. Blood IL-1β and IL-6 concentrations were assessed respectively with Mouse IL-1 beta SimpleStep Elisa kit (Abcam) and Mouse IL-6 ELISA Kit (Abcam), according to manufacturer's instructions. Briefly, mouse blood was extracted using EDTA tubes at different timepoints after stroke then centrifuged at 3000 x g for 15 min. The plasma was collected and stored in -80 °C until running the assay. All samples were run in duplicates and all duplicates showed a coefficient of variation <15%.

qPCR

Total RNA from FACS-sorted cells was extracted using Arcturus® PicoPure® RNA Isolation Kit, according to the manufacturer's instructions. Reverse transcription to cDNA was performed using High-Capacity Reverse Transcription Kit. qRT-PCR was performed with a standard SYBR-Green PCR kit protocol as previously described.[25] Relative changes on *Mmp9* gene expression levels were normalized to *Ppia* gene expression levels by using the $2^{-03940394^{Ct}}$ method.[26]

Splenocytes isolation and incubation with CVC

Mice were deeply anaesthetized and euthanized as described above. Spleens were immediately removed and cell suspensions were prepared as previously described. Splenocytes were incubated for 2h at 37°C with CVC at different concentrations (0 μM, 5μM, 10 μM and 100 μM). Afterwards, cells were washed and stained with surface markers for flow cytometry as described above.

BMDM and primary monocyte isolation

Bone marrow derived macrophage (BMDM) cells are generated from mouse tibia and femur. After flushed out from both femurs and tibias, bone marrow cells were filtered through 40μm cell strainers to obtain single cell suspensions. Subsequently, cells were resuspended in DMEM (Gibco), supplemented with 10% fetal bovine serum (FBS) (Gibco), 1% Gentamycin (ThermoFisher Scientific) and 20 % L929 cell-conditioned medium (LCM) to promote differentiation into macrophages. A total of $5x10^5$ cells were seeded per well and cultured for 7 days at 37 °C with 5% CO2.

Primary monocytes were obtained from isolated cell suspensions using the negative selection kit EasySep monocyte isolation kit (StemCell). Sorted monocytes were then plated in 12-well plates at $5x10^5$ cells per well in DMEM (Gibco), supplemented with 10% FBS (Gibco) and 1% gentamycin (Thermo Scientific) and cultured for 24h at 37 °C with 5% CO2.

BMDM and primary monocyte phagocytosis assay

Fully differentiated BMDMs or cultured primary monocytes were primed with 100 ng/ml LPS for 4h. Then, cells were treated with 1μg/ml (BMDMs) or 5μg/ml (monocytes) pHrodo Zymosan (Thermo Fisher, US) for 30 min. Zymosan uptake by cells was analyzed via flow cytometry, as previously described.

BMDM stimulation with IL-1β

Fully differentiated BMDM were treated with 5ng/ml or 50ng/ml of recombinant IL-1β or vehicle for 6h at 37°C with 5% CO2. Cells were then washed and harvested and analyzed by western blot.

Western blotting analysis

BMDM were lysed with RIPA lysis/extraction buffer with added protease/phosphatase inhibitor (Thermo Fisher Scientific). Total protein was quantified using the Pierce BCA protein assay kit (Thermo Fisher Scientific). Whole cell lysates were fractionated by SDS-PAGE and transferred onto a polyvinylidene difluoride membrane (BioRad). After blocking for 1 hour in TBS-T (TBS with 0.1 % Tween 20, pH 8.0) containing 4 % skin mile powder (Sigma), the membrane was incubated with the primary antibodies against following antibodies: rabbit anti-cJun/phospho-cJun (1:1000; Cell signalling), rabbit anti-actin (1:2000; Sigma), rabbit APOE (1: 5000, Invitrogen), mouse anti-β-Tubulin (1:2000, Sigma Aldrich) and rabbit anti-LPL (1:1000, Invitrogen, US). Membranes were washed three times with TBS-T and incubated for 1 hour with HRP-conjugated anti-rabbit or anti-mouse secondary antibodies (1:5000, Dako) at RT. Membranes were developed using ECL substrate (Millipore, US) and acquired via the Vilber Fusion Fx7 imaging system.

Bulk mRNA sequencing of human heart samples

Human heart paraffin sections were used to retrieve the PFA-cross-linked mRNA as previously described.[27] In brief, PFA-fixed paraffin-embedded hearth tissue sections were scratched from each slide using a stereomicroscope (Olympus SZ51, Model# 1111260100), collected in cold PKD buffer supplemented with proteinase K solution and snap-frozen in liquid nitrogen until further use. To prepare the Smartseq2 libraries, samples were thawed at RT for 3 min and incubated at 56°C in a thermal cycler (lid temperature 66°C), for 4 h or until tissue was completely dissolved. Samples were then placed on ice and incubated at 56°C for 1 min with dT25 magnetic beads to reverse crosslinked samples. Samples were incubated at RT to allow mRNA hybridization and washed with 1x hybridization buffer (HB), containing 2x SSPE, 0.05% Tween-20 and 0.05% RNase Inhibitor. Samples were then washed with PBS with 0.1% RNase Inhibitor and incubated with RNase-free water for 2 min at 80°C to elute mRNA. Smartseq2 libraries were prepared from 1 ng mRNA, as previously described. Libraries were sequenced 2x60 reads base pairs paired-end on an Illumina NextSeq 1000 to a depth of 300,000–600,000 reads/sample.

Bulk mRNA sequencing data analysis

FastQC was used to check the quality of fastq files. Low-quality reads and adapters were trimmed using Cutadapt using the following parameters: (1) reads <20 bp, and (2) quality cutoff of 20. The trimmed FASTQ files were mapped to the mm10 reference genome using STAR. The mapped reads (of lesion tissue sections) belonging to the same slide were merged using the merge BAM files tool in Galaxy version 4. To quantify the number of reads mapping to the exons of each gene, featureCounts program was used. Data was further analyzed in R. As quality control steps, the following samples were filtered out for further analysis: (1) Samples with a high percentage of mitochondrial genes (>20%); samples with a high percentage of ribosomal genes (>8%); (3) very highly-expressed genes with more than 20.000 counts; and (4) genes that are expressed in less than 5 samples with more than 1 count. Hereafter, raw gene counts were normalized to stabilize variance (regularized logarithm method) and differentially expressed genes were identified using the DESeq2 package in R.

QUANTIFICATION AND STATISTICAL ANALYSIS

Data were analyzed using GraphPad Prism version 9.0. All summary data are expressed as the mean ± standard deviation (s.d.), unless indicated otherwise. Normality was assessed in all datasets using the Shapiro-Wilk normality test. Normally-distributed data were analyzed using a two-way Student's t test (for 2 groups) or ANOVA (for > 2 groups). Data with a no normal distribution were analyzed using the Mann-Whitney U test (for 2 groups) or Kruskal-Wallis test (H test, for > 2 groups). Multiple comparison adjusted p values were computed using Bonferroni correction or Dunn's multiple comparison tests. A p value < 0.05 was considered statistically significant.

CellPress
OPEN ACCESS

Supplemental figures

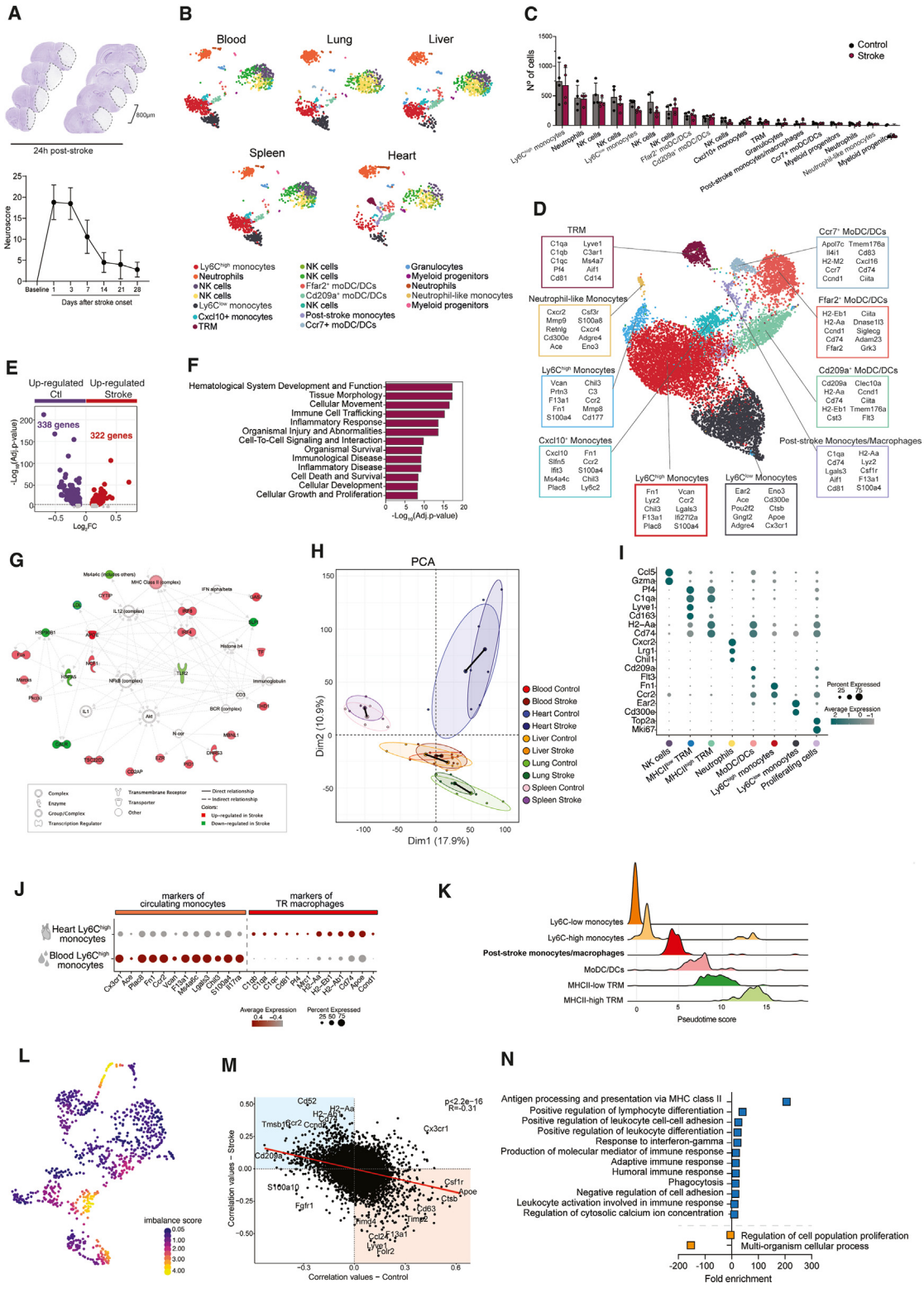

(legend on next page)

Figure S1. Stroke induces long-term inflammatory changes in monocytes/macrophages from peripheral organs, related to Figure 1

(A) Representative images of ischemic stroke lesions from the transient middle cerebral artery occlusion (tMCAo) stroke mouse model (upper). Graph showing the neurological deficits of mice over time after stroke, assessed by the Neuroscore test.

(B) Uniform manifold approximation and projection (UMAP) plots of a representative set of 1,000 $CD45^+$ $CD11b^+$ cells per peripheral organ, colored by identified populations.

(C) Number of cells per identified population, split by condition.

(D) UMAP plot of the monocytes and macrophages clusters identified in peripheral organs, annotated with key expressed genes per population.

(E) Volcano plot showing the upregulated (322 genes, red) and downregulated genes (338 genes, purple) of $Ly6C^{high}$ monocytes from stroke and control mice. Colored genes are $p < 0.05$ and |fold-change| > 1.25.

(F) Pathway analysis was performed using ingenuity pathway analysis (IPA, Qiagen) using the DEG from $Ly6C^{high}$ monocytes, with an adjusted $p < 0.05$ and |fold-change| > 1.58. Top diseases and functions categories sorted by p value are displayed.

(G) Functional gene interaction network analysis using IPA. Genes are colored based on fold-change values determined by the single-cell mRNA sequencing analysis, where red indicates an increase in stroke and green in control animals.

(H) PCA plot displaying all analyzed samples from all peripheral organs. The PCA was calculated from a total of 18,834 genes identified in peripheral $CD45^+CD11b^+$ myeloid cells. The Euclidian distances between stroke and control clusters per organ are indicated in black lines.

(I) Dot plot showing the expression profile of selected genes key for the identification of the cell populations in the heart. The dot size corresponds to the fraction of cells within each condition expressing the indicated transcript, and the color indicates average expression.

(J) Dot plot showing the expression levels of selected gene features in $Ly6C^{high}$ monocytes from the heart and blood. Genes were selected from the list of DEG between both cell populations. The dot size corresponds to the fraction of cells within each condition expressing the indicated transcript, and the color indicates average expression.

(K) Ridge plots showing the pseudotime score distribution in each cell population identified in the heart.

(L) UMAP plot showing the imbalance score.

(M) Correlation values of the trajectory-driver genes between stroke and control conditions.

(N) Pathway analysis using ShinyGO for differential trajectory-driver genes between stroke and control conditions.

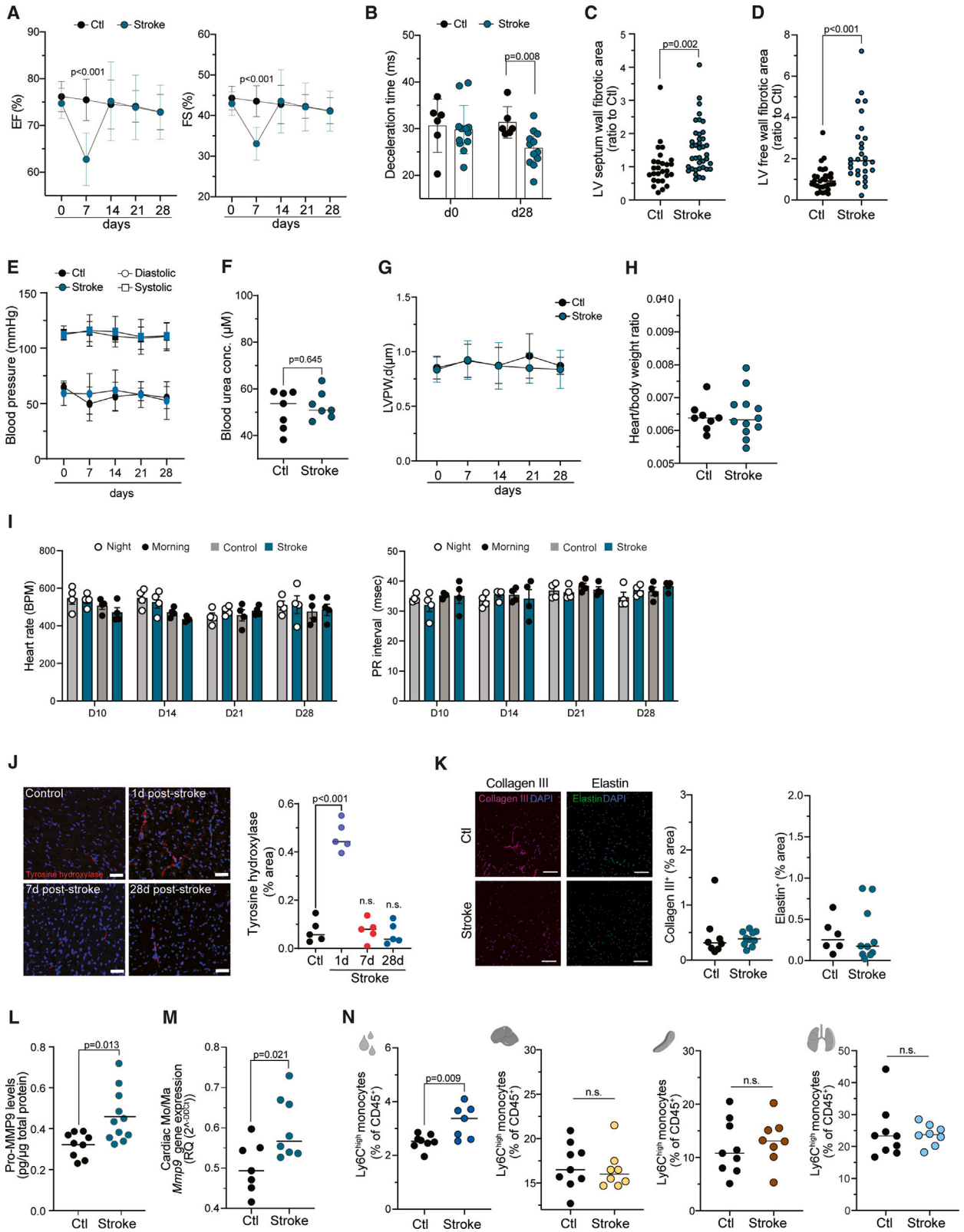

(legend on next page)

Figure S2. Stroke results in chronic cardiac diastolic dysfunction, related to Figure 2

(A) Quantification of the ejection fraction (EF, left) and fractional shortening (FS, right) at indicated time points (days) before (day 0) and after stroke, and control (U tests, *n* = 6/12 per group).

(B) Quantification of the transmitral deceleration time at days 0 and 28 in control and stroke mice (U tests, *n* = 6/12 per group).

(C) Quantification of cardiac fibrosis in the LV septum wall at 1 month after stroke and control (t test, *n* = 7/10 per group, 4 heart sections per mouse).

(D) Quantification of cardiac fibrosis in the LV free wall at 3 months after stroke and control (t test, *n* = 7/10 per group, 4 heart sections per mouse).

(E) Quantification of the blood pressure at the indicated time points (days) before (day 0) and after stroke, and control conditions (*n* = 3/8 per group).

(F) Blood urea concentration was measured in mice 1 month after stroke or in control mice (t test, *n* = 7 per group).

(G) Quantification of the LV posterior wall thickness at the end of diastole (LVPW, d) at indicated time points (days) before (day 0) and after stroke, and control mice (U tests, *n* = 6/12 per group).

(H) Heart-body ratio was measured in mice 1 month after stroke and control mice (t tests, *n* = 8/12 per group).

(I) Quantification of heart rate (right) and PR interval (left) at indicated time points (days) after stroke and control, using continuous ECG telemetry (U tests, *n* = 4 per group). Each time point include the measurement in the morning and at night.

(J) Representative immunofluorescence images of the tyrosine hydroxylase (TH) in the heart at indicated time points (days) after stroke and control. DAPI was used as nuclear dye (left, scale bars, 50 μm). Quantification of the TH content, expressed in percentage of total area of the LV free wall (right; t test, *n* = 5/group).

(K) Representative images of immunofluorescence staining for the detection of collagen III and elastin in heart coronal sections (left; scale bars, 50 μm). Corresponding quantification of collagen III and elastin content, expressed in percentage of total area of the LV free wall (right; t test, *n* = 8/10 per group).

(L) Total pro-MMP9 protein levels were measured in heart samples from stroke and control mice. Pro-MMP9 protein levels are normalized to total protein content (U test, *n* = 9/11 per group).

(M) RT-qPCR was performed on sorted monocyte/macrophages (Mo/Ma, $CD45^+Ly6G^-CD11b^+$) to measure the expression levels of *Mmp9* mRNA, quantified relative to the expression of the housekeeping gene encoding for *Ppia*, and normalized to control levels (U test, *n* = 7 per group).

(N) Quantification of the $Ly6C^{high}$ monocytes ($CD45^+CD11b^+Ly6g^-Ly6C^{high}$) in blood, liver, spleen, and lung from mice 1 month after stroke and control mice, measured by flow cytometry and expressed as percentage of total $CD45^+$ cells (t test, *n* = 8/7 per group).

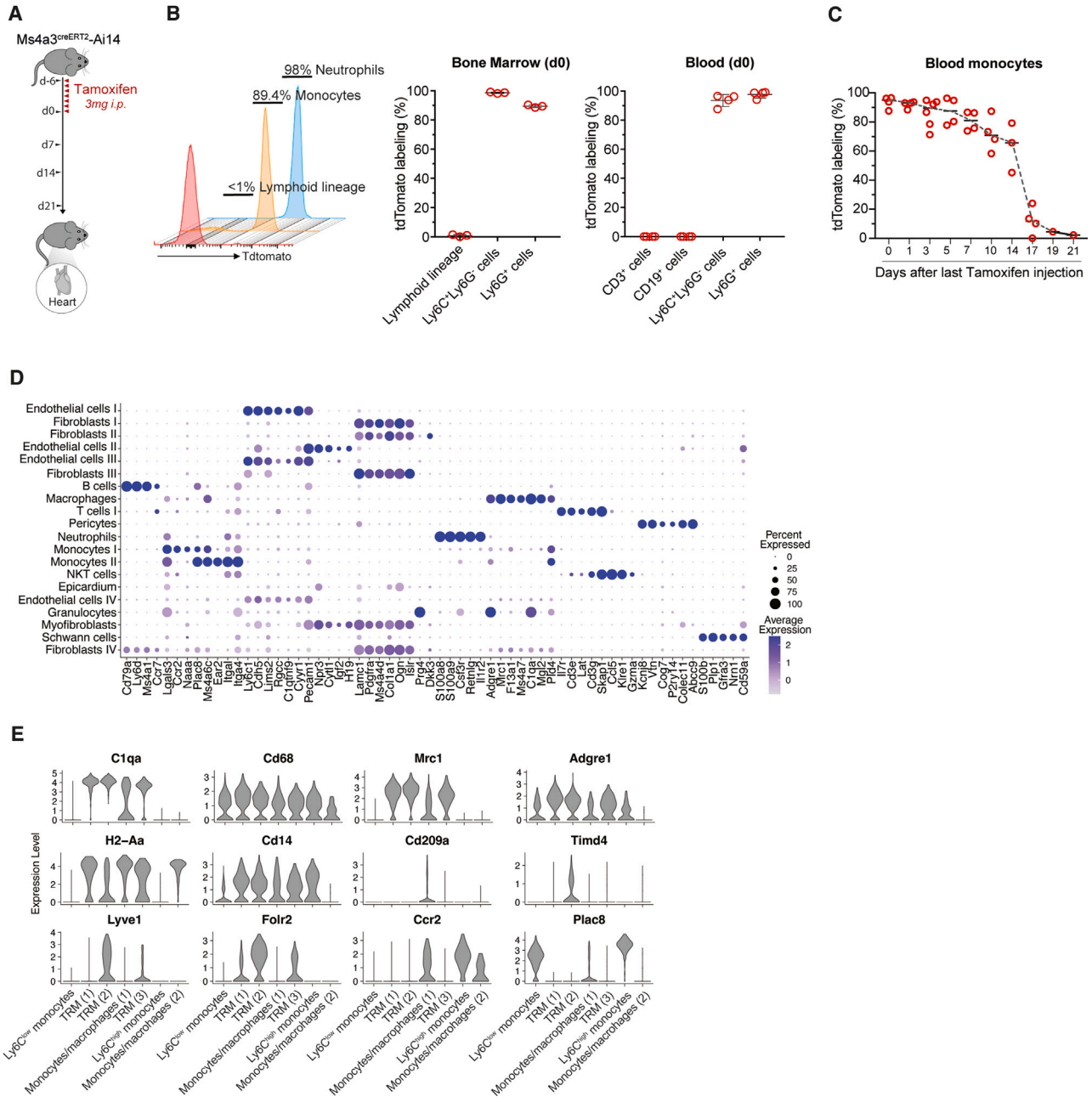

Figure S3. Stroke promotes chronic monocyte recruitment into the heart, related to Figure 4

(A) Schematic experimental design: Ms4a3^{creERT2}xAi14 mouse were treated with tamoxifen for 7 consecutive days. Mice were sacrificed at different time points within the 3 weeks after tamoxifen treatment, and the heart myeloid cells were analyzed by flow cytometry (left).

(B) tdTomato labeling of lymphocytes (CD3+, CD4+, CD8a+, CD19+, and Ter119+), monocytes (Ly6C+Ly6G−), and neutrophils (Ly6C+Ly6G+) in bone marrow (middle) and blood (right) after 7 daily doses of tamoxifen (n = 3/4).

(C) tdTomato labeling of monocytes (Ly6C+Ly6G−) in blood over time after 7 daily doses of tamoxifen (n = 4).

(D) Dot plot showing the expression profile of selected key genes for the identification of cell subsets of cardiac interstitial cells sorted from hearts 1 month after stroke or control surgery in Ccr2^{creERT2}xAi14 reporter mice (n = 2 mice/group). The dot size corresponds to the fraction of cells within each condition expressing the indicated transcript, and the color indicates average expression.

(E) Violin plots showing the expression levels of selected key genes for the identification of the populations of cardiac monocytes and macrophages.

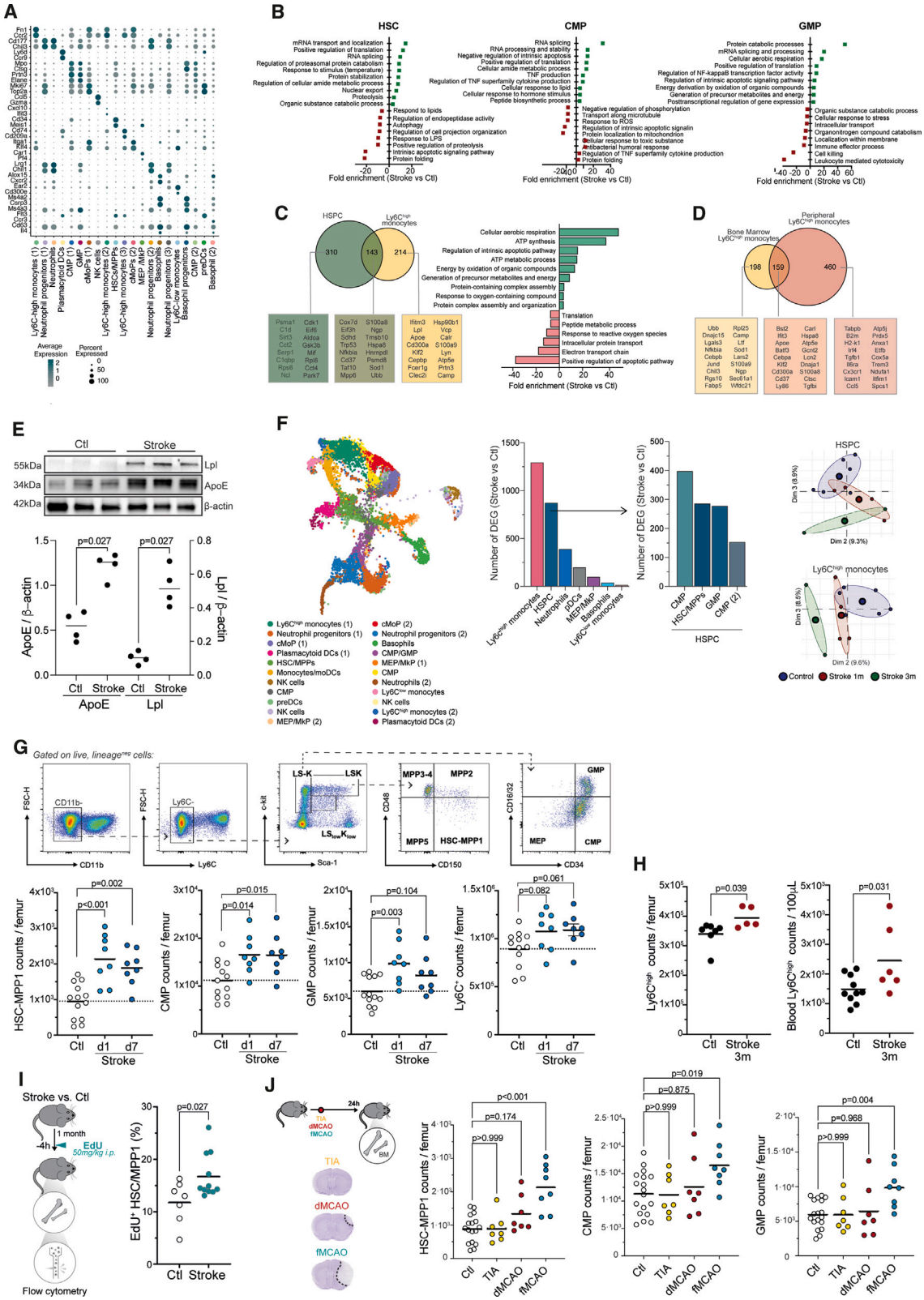

(legend on next page)

Figure S4. Bone marrow cellularity and function are chronically altered after stroke, related to Figure 5

(A) Dot plot showing the expression profile of selected key genes for the identification of the populations of lymphoid (CD3, CD4, CD8a, CD19, and Ter119)-lineage and neutrophil (Ly6G) negative myeloid cells sorted from the BM of control and stroke mice 1 month after stroke (n = 4/group). The dot size corresponds to the fraction of cells within each condition expressing the indicated transcript, and the color indicates average expression.

(B) Pathway analysis was performed using differentially expressed genes between stroke and control conditions in hematopoietic stem cells (HSCs), common myeloid progenitors (CMPs), and granulocyte-monocyte progenitors (GMPs). Biological processes were grouped and sorted by p value.

(C) Venn analysis illustrating shared DEGs between stroke and control conditions in both HSCs and Ly6C^{high} monocytes (right). Pathway analysis of the shared DEGs in HSCs and Ly6C^{high} monocytes. Biological processes were grouped and sorted by p value (left).

(D) Venn diagram illustrating shared DEGs between stroke and control conditions in bone marrow (BM) and circulating (blood) Ly6C^{high} monocytes.

(E) Representative immunoblot graph of the lipoprotein ligase (Lpl) and apolipoprotein E (APOE) in cultured BM-derived macrophages (BMDMs) isolated from mice 1 month after stroke and control mice (upper). Corresponding quantification of the APOE and Lpl intensity normalized to β-actin (U test, n = 4 per group).

(F) UMAP plot of the 23,516 lymphoid lineage- (CD3, CD4, CD8a, CD19, and Ter119) and neutrophil- (Ly6G) negative myeloid cells sorted from the BM 3 months after stroke or control (left). Quantification of DEGs between stroke and control conditions per identified subset (adj. $p < 0.05$) (middle). Euclidian distances in the PCA space of HSPC and Ly6C^{high} monocytes from control mice and mice 1 and 3 months after stroke.

(G) Representative gating strategy for BM progenitor cells and cell count quantifications of hematopoietic stem cells-multipotent progenitors 1 (HSC-MPP1), common myeloid progenitors (CMPs), granulocyte-monocyte progenitors (GMPs), and Ly6C^{+} monocytes in stroke and control mice at 1 and 7 days after stroke (U test; n = 9/13 per group). LSK, Lin-Sca1+c-Kit+; LS-K, Lin-Sca1-c-Kit+; LS^{low}K^{low}, Lin-Sca1^{low}c-Kit^{low}; MMP, multipotent progenitor.

(H) Cell count quantification of BM (left, t test, n = 7/5 per group) and blood Ly6C^{high} monocytes (right, t test, n = 10/6 per group) at 3 months after stroke and control.

(I) Schematic experimental design: stroke and control mice were administered with EdU 4 h before sacrifice. Subsequently, BM cells were isolated and analyzed by flow cytometry (left). Corresponding quantification of the percentage of EdU+ cells from HSC/MPP1 in stroke and control mice (U test; n = 7/11 per group).

(J) Schematic experimental design: mice underwent either transient ischemic attack (TIA), distal middle cerebral artery occlusion (dMCAo), or filament-induced occlusion of the proximal middle cerebral artery (fMCAO). BM was collected 24 h post-surgery and analyzed by flow cytometry (upper left). Representative images of the corresponding brain lesions 24 h after each surgery (bottom left, no structural lesion after TIA). Cell count quantification of HSC-MPP1, CMP, and GMP for each condition (U test; n = 7–17 per group).

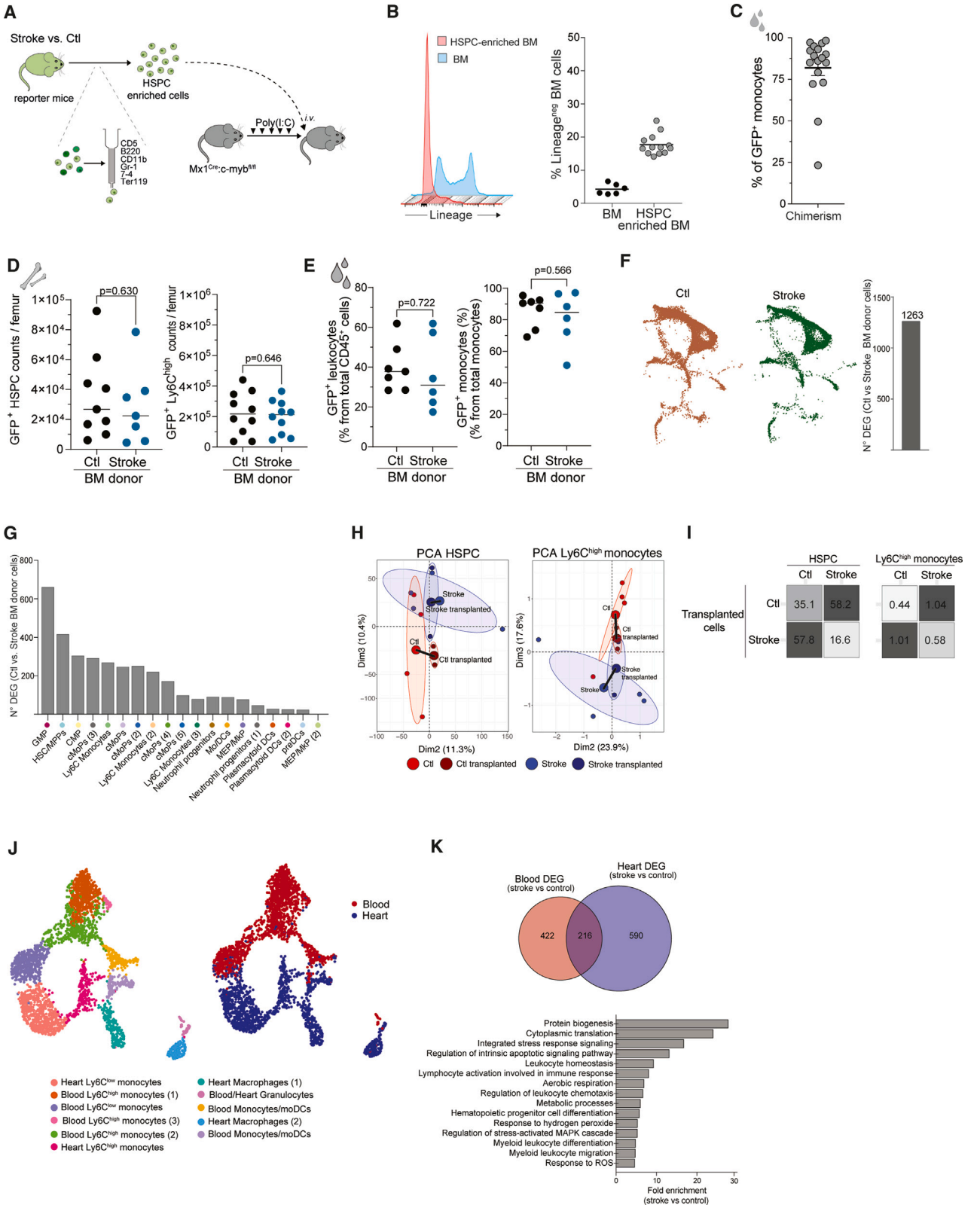

(legend on next page)

Figure S5. Stroke induces persistent innate immune memory, related to Figure 5

(A) Schematic experimental design: bone marrow (BM) cells were isolated from actin-eGFP or kikGR control and stroke mice 1 month after stroke and enriched for hematopoietic stem and progenitor cells (HSPCs). HSPC-enriched GFP+ cells were transplanted into BM-depleted $Mx1^{Cre}$:c-$myb^{fl/fl}$ mice.

(B) Histogram of cells before and after HSPC enrichment showing the proportion of $lineage^{neg}$ and $lineage^{pos}$ BM cells (right). Corresponding flow cytometry quantification of the percentage of $lineage^{neg}$ cells before and after HSPC enrichment (n = 6/12 per group, right).

(C) Blood chimerism 1 month after BM transplantation, depicted as the percentage of GFP^+ monocytes in blood from recipient mice.

(D) Percentage of GFP^+ donor-derived HSPC ($Lineage^-$ $c\text{-}kit^+$) cells and $Ly6C^{high}$ monocytes from recipient mice (n = 7/10 per group). Results indicate no difference in repopulation efficacy between control and stroke donors.

(E) Percentage of circulating $eGFP^+$ leukocytes ($CD45^+$) monocytes ($Ly6C^{high}$) from recipient mice (n = 7/6 per group).

(F) UMAP plot of myeloid cells from the BM of transplanted mice, split by condition (left) and number of differentially expressed genes (DEGs) between stroke and control (adjusted $p < 0.05$).

(G) Number of DEGs between stroke and control conditions per cell type.

(H) PCA plot displaying individual samples from the BM of stroke (light blue) and control mice (light red) and the BM of recipient mice transplanted with stroke (dark blue) and control (dark red) GFP^+ HSPC-enriched BM cells (left). The PCA was calculated from a total of 18,834 genes identified in BM myeloid cells. Euclidian distances between stroke samples and control samples are indicated in black lines and were calculated from the mean of each cluster.

(I) Euclidian distances in the PCA space between the stroke and control samples and samples from recipient mice transplanted with stroke and control GFP^+ HSPC-enriched BM cells.

(J) UMAP plot of a total of 3,098 GFP^+ blood monocytes and cardiac monocytes/macrophages from recipient mice transplanted with stroke or control GFP^+ HSPC-enriched BM cells, colored by identified cluster (left) or by organ (right).

(K) Venn diagram illustrating shared DEGs between blood and heart GFP^+ cells isolated from recipient mice transplanted with stroke or control GFP^+ HSPC-enriched BM cells (upper). Pathway analysis was performed using ShinyGO for shared DEGs between blood and heart, with an FDR-adj. $p < 0.05$ (bottom).

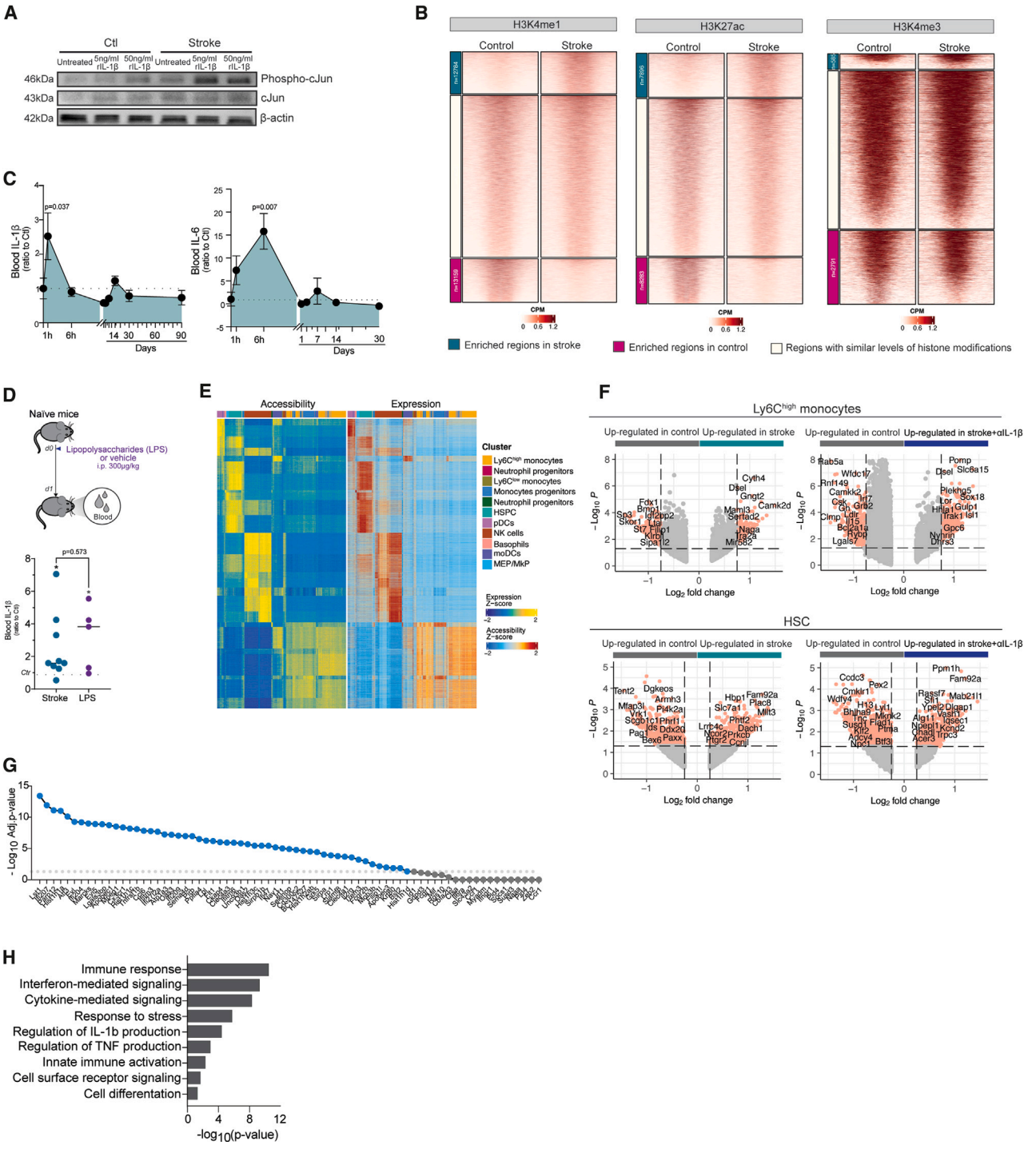

Figure S6. Innate immune memory is mediated by early post-stroke IL-1β secretion, related to Figure 6

(A) Representative immunoblot graph of the protein levels of c-Jun and phospho-c-Jun in cultured bone marrow-derived macrophages (BMDMs) isolated from mice 1 month after stroke and control mice, and following stimulation with 5 or 50 ng/mL of recombinant IL-1β.

(B) Density heatmaps H3K4m1, H3K27ac, or H3K4me3 peaks in Ly6C^{high} monocytes from mice 1 month post-stroke (up, green) or control mice (down, pink), split by condition. Regions with similar levels of histone modifications are also shown (middle, white) (left).

(C) Plasma IL-1β and IL-6 levels at indicated time points after stroke, expressed as ratio to control levels (baseline) before stroke.

(D) Schematic experimental design: mice received a single injection intraperitoneal (i.p.) injection of lipopolysaccharides (LPSs). 24 h later, mice were sacrificed, and blood was collected (upper). Plasma IL-1β levels 24 h after stroke or LPS treatment, expressed as ratio to IL-1β levels from naive mice (control).

(legend continued on next page)

(E) Side-by-side heatmaps showing the correspondence links of peaks (left) and gene (right) from the single-nuclei ATAC sequencing and single-cell mRNA sequencing, respectively.
(F) Volcano plots showing the differentially accessible peaks between vehicle-treated stroke and control and between αIL-1β-treated stroke and control mice for Ly6C^{high} monocytes (upper) and HSCs (lower). Colored peaks are $p < 0.05$ and $\log_2FC > 0.75$, and top peaks were associated to the closest genes (Table S4).
(G) Dot plot showing the statistical significance of the differential expression of genes that showed a significant correlation with the top 10 transcription factors with highest differential activity between stroke and control conditions in Ly6C^{high} monocytes.
(H) Pathway analysis performed by g:Profiler using the differential expressed genes between stroke and control conditions that showed significant correlation with the top 10 transcription factors with highest differential activity between these two conditions in Ly6Chigh monocytes. Biological processes were grouped and sorted by *p* value.

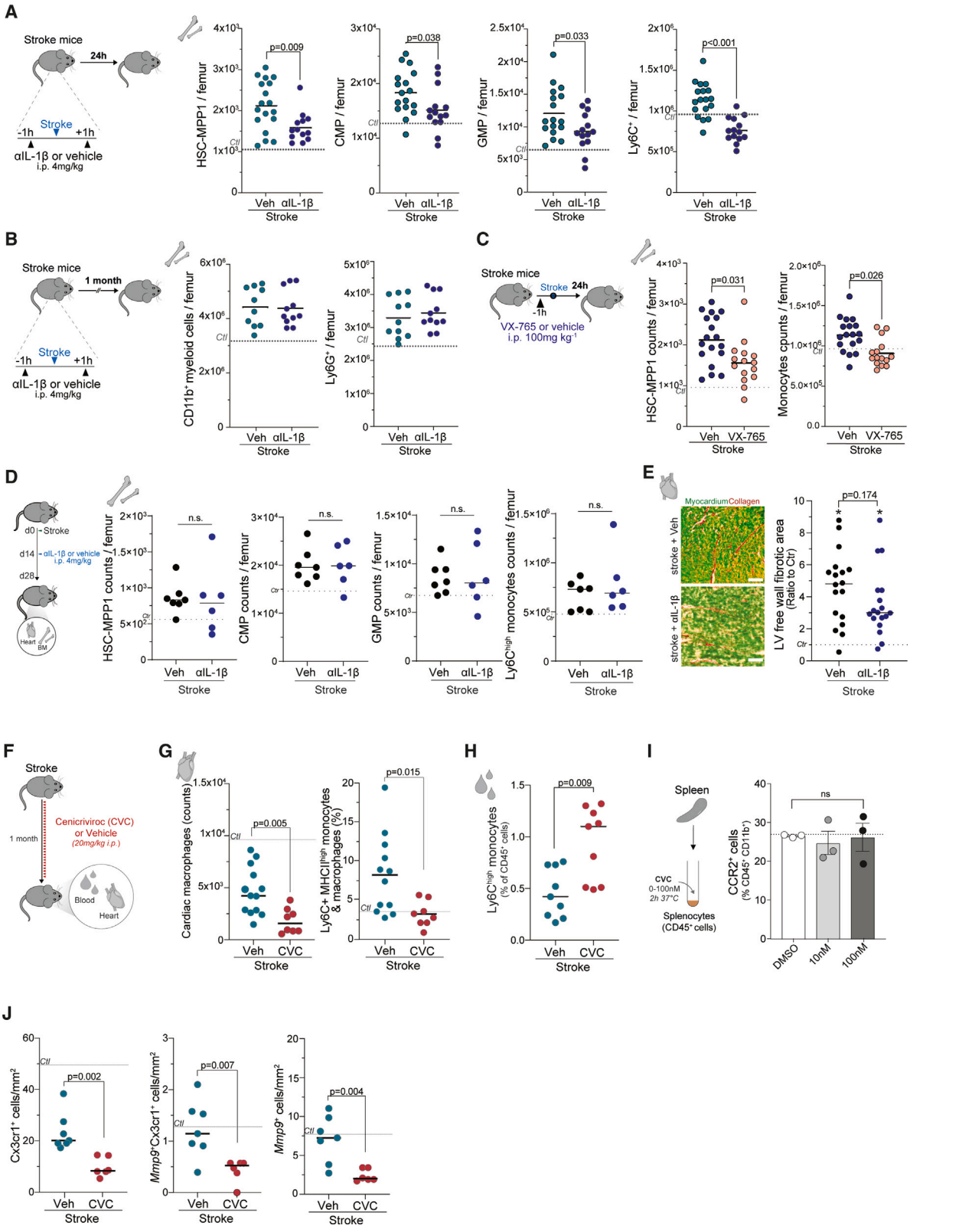

(legend on next page)

Figure S7. IL-1β-driven innate immune memory mediates remote organ dysfunction after stroke, related to Figure 7

(A) Schematic experimental design: mice received IL-1β-specific neutralizing antibodies or vehicle 1 h before and 1 h after stroke induction. 24 h later, BM cells were isolated for flow cytometry (left). Cell count quantifications of hematopoietic stem cells-multipotent progenitors 1 (HSC-MPP1), common myeloid progenitors (CMPs), granulocyte-monocyte progenitors (GMPs), and total Ly6C$^+$ monocytes in BM from anti-IL-1β or vehicle-treated stroke mice (U test; n = 13/18 per group).

(B) Same experimental design as in (A), but BM was collected 1 month after stroke for flow cytometric cell count quantifications of total CD11b$^+$ myeloid cells and Ly6G$^+$ neutrophils (U test; n = 10/11 per group).

(C) Schematic experimental design: mice received the caspase-1 inhibitor VX-765 or vehicle 1 h before stroke induction. 24 h later, BM was collected for flow cytometry analysis (left). Cell count quantifications of HSC-MPP1 and total Ly6C$^+$ monocytes in BM from VX-765 or vehicle-treated stroke mice (U test; n = 18/15 per group).

(D) Schematic experimental design: mice received IL-1β neutralizing antibodies or vehicle 14 days after stroke. 2 weeks later, 1 month after stroke, BM and hearts were collected for flow cytometry and histology staining, respectively (left). Cell count quantifications of HSC-MPP1, CMP, GMP, and Ly6C^{high} monocytes in BM from anti-IL-1β or vehicle-treated stroke mice (t test; n = 7/6 per group).

(E) Representative images of the Sirius red/fast green collagen staining performed on cardiac coronal sections from delayed anti-IL-1β and vehicle-treated stroke mice (left). Quantification of cardiac fibrosis in the LV free wall in anti-IL-1β and vehicle-treated stroke mice. Dashed line indicates mean percentage of fibrotic area in control mice, * indicates significant difference between respective stroke to control mice per treatment condition (t test, n = 5 per group, 3–4 heart sections per mouse).

(F) Schematic experimental design: stroke mice were administered daily with the dual C-C chemokine receptors type 2 and 5 antagonist cenicriviroc (stroke + CVC) or vehicle (stroke) for 28 days. Mice were sacrificed at day 28, and the heart and blood were collected for flow cytometry and histological analysis.

(G) Flow cytometry of total CCR2$^+$ and Ly6C$^+$MHC-II^{high} monocytes/macrophages in the heart of stroke mice treated with CVC or vehicle (t test; n = 8/12 per group).

(H) Flow cytometry for circulating Ly6C^{high} monocytes in CVC- or vehicle-treated stroke mice, expressed as percentage of total circulating CD45$^+$ cells. Dashed lines indicate mean values in control mice (t test; n = 9 per group).

(I) Schematic experimental design: splenocytes were freshly isolated from naive mice and treated with CVC at a dose of 0 (DMSO), 10, and 100 nM. 2 h after treatment, the percentage of live CCR2$^+$ cells was evaluated by flow cytometry.

(J) smFISH quantification for the detection of total *Cx3cr1*$^+$ cells (left), *Mmp9*$^+$ *Cx3cr1*$^+$ cells (mid), and *Mmp9*$^+$ cells (right) in the hearts of CVC- or vehicle-treated stroke mice. DAPI was used as nuclear dye. Dashed lines indicate mean values in control mice (t test, n = 6/7 per group).